Investigation of geometric frustration in magnetic oxides

Stuart Calder

UCL

Supervisor: Prof. S. T. Bramwell

Thesis submitted for the degree of
Doctor of Philosophy (PhD)

I, Stuart Calder, confirm that the work presented in this thesis is my own. Where information has been derived from other sources, I confirm that this has been indicated in the thesis.

Abstract

This thesis describes the experimental investigations of geometric frustration in magnetic oxides. The rare earth double perovskites Ba_2HoSbO_6 and Ba_2ErSbO_6 crystallise into the $Fm\bar{3}m$ cubic space group with the rare earth ions forming a face centred cubic arrangement of edge sharing tetrahedra. This arrangement is expected to result in geometric magnetic frustration. Previous studies have revealed no long range order or spin glass behaviour down to 1.5 K. In this work, low temperature neutron scattering measurements were carried out to investigate the magnetic behaviour below 1.5 K. The crystalline electric field was found to dominate the magnetic behaviour. Using experimental results from inelastic neutron scattering the crystal field level scheme was solved for Ba_2HoSbO_6 and Ba_2ErSbO_6. These results were used to successfully predict the observed behaviour of both systems, showing that they can be considered to behave as single ion systems down to the lowest temperature investigated of 0.06 K. As such exchange interactions and any effects of frustration are not evident at the temperatures investigated.

As a further step to investigate frustration in magnetic oxides $LuCuGaO_4$ was considered. This has triangular bilayers of magnetic Cu^{2+} and non-magnetic Ga^{3+} that are expected to lead to two dimensional geometric magnetic frustration of the Cu^{2+} ions. The presence of Ga^{3+} on the same lattice site as the Cu^{2+} lead to charge frustration. Polarised neutron analysis, inelastic neutron scattering and μSR build up a coherent picture of the low temperature behaviour of the system which questions the previous belief in the literature of a spin glass transition. Instead what is found is a spin liquid state.

Finally, the problem of interpreting the subtle features and signatures of frustration is considered with an alternative μSR technique. μSR allows local interactions to be investigated, however the problem of interpreting the results can lead to ambiguity. It is shown that it is possible to successfully implant muons outside the sample of interest and accurately measure the sample's magnetic dipolar field. In this way μSR can be used as a bulk magnetometer with the same frequency response as standard μSR and it is shown that this can be useful in the investigation of frustrated materials with reference to results on $Tb_2Sn_2O_7$.

Acknowledgements

In the course of carrying out this work I received a great deal of help and support, in differing forms, all of which I am grateful for. First of all I would like to thank Steve Bramwell for all his hard work and enthusiasm throughout. Andrew Wills has always been at hand to help and his input and enthusiasm has been much appreciated, as has the help offered by Des McMorrow. Tom Fennell deserves special praise, especially in the early stages of my PhD, for helping me with the experimental and computational aspects large and small.

A great deal of respect and thanks goes to the instrument scientists and collaborators who helped during this thesis, namely Sean Giblin, Pascale Deen, Winfried Kocklemann, Andrew Wildes, Ross Stewart, Aziz Daoud-Aladine, Jon Taylor, Xianglin Ke and Carlo Carboni. This work relied on the skill and hard work of the cryogenic teams at ISIS and the ILL and I am grateful for their efforts.

A special mention for my fellow PhD group members Bob Aldus and Tom Forrest for many breaks and discussions which helped me get through the PhD years.

I would like to thank friends and family for all the support during my PhD. My family for their visits and allowing me to escape up to Edinburgh. Friends for offering me many necessary distractions throughout my time in London.

Finally, I thank Hannah for her constant patience and support.

Contents

List of Figures

List of Tables

Chapter 1

Introduction

1.1 Magnetism

1.1.1 Magnetism of a single ion

There are two magnetic moment operators associated with the electron. The first is the orbital magnetic moment operator ($\hat{\boldsymbol{\mu}}_{\boldsymbol{\ell}}$) and is given by:

$$\hat{\boldsymbol{\mu}}_{\boldsymbol{\ell}} = -\mu_{\mathrm{B}}\hat{\boldsymbol{\ell}}, \tag{1.1}$$

where $\hat{\boldsymbol{\ell}}$ is the orbital magnetic moment operator and μ_{B} is the Bohr magneton, defined as $\mu_{\mathrm{B}} = \frac{e\hbar}{2m_e}$. The second is the spin magnetic moment operator ($\hat{\boldsymbol{\mu}}_{\boldsymbol{s}}$) and is given by:

$$\hat{\boldsymbol{\mu}}_{\boldsymbol{s}} = -2\mu_{\mathrm{B}}\hat{\boldsymbol{s}}, \tag{1.2}$$

where $\hat{\boldsymbol{s}}$ is the spin operator and has eigenvalues $s_z = \pm\frac{1}{2}$ for a spin along the z-axis.

For an atom with i electrons: $\hat{\mathbf{L}} = \sum_i \hat{\boldsymbol{\ell}}_i$ and $\hat{\mathbf{S}} = \sum_i \hat{\boldsymbol{s}}_i$. The magnetic moment of an atom or ion in free space is:

$$\hat{\boldsymbol{\mu}} = -g_J\mu_{\mathrm{B}}\hat{\mathbf{J}} \tag{1.3}$$

where the total angular momentum operator is: $\hat{\mathbf{J}}$ = $\hat{\mathbf{L}}$ + $\hat{\mathbf{S}}$. The operator $\hat{\mathbf{J}}^2$ has eigenvalues $J(J+1)$. The Landé g-factor, g_J, is given by:

$$g_J = \frac{3}{2} + \frac{S(S+1) - L(L+1)}{2J(J+1)} \tag{1.4}$$

In a magnetic field the energy levels of the system are given by:

$$U = -\hat{\boldsymbol{\mu}}.\boldsymbol{B} = m_J g \mu_{\mathrm{B}} B \tag{1.5}$$

where m_J is the azimuthal quantum number with values between $J, J-1, ..., -J$.

When magnetic ions are placed in a crystal structure they are surrounded by a crystalline electric field (CEF) created by oppositely charged ions. For orbitals (except the spherically symmetric s-orbital) there is angular dependence. The CEF lifts the $(2J+1)$ degeneracy of m_J states.

1.1.2 Magnetisation and susceptibility

The magnetisation $\mathbf{M}$ is defined as the magnetic moment per unit volume and for a linear material in a magnetic field $\mathbf{H}$ it is given by:

$$\mathbf{M} = \chi \mathbf{H} \tag{1.6}$$

where χ is the magnetic susceptibility.

Curie's Law

For a paramagnet the molar susceptibility is given by Curie's law:

$$\chi = \frac{N_A g_J^2 \mu_{\mathrm{B}}^2}{3 k_B T} J(J+1) \tag{1.7}$$

where $N_A = 6.022 \times 10^{23}$ is Avagadro's number and k_B is Boltzmann's constant.

The effective magnetic moment is expressed by the identity (in cgs units):

$$\mu_{eff} \equiv 2.827 \sqrt{\chi_m T} \tag{1.8}$$

Curie-Weiss Law

The Curie-Weiss law describes a ferromagnetic material in the paramagnetic regime in a mean field. The Curie-Weiss law is:

$$\chi = \frac{C}{T - \theta_W} \tag{1.9}$$

where $C = N_A\mu^2/3k_B$ is the Curie constant with $\mu = g_J\sqrt{J(J+1)}\mu_\mathrm{B}$. θ_W is the Weiss constant, with units of temperature.

- If $\theta_W > 0$ magnetic interactions in the material are ferromagnetic.
- If $\theta_W < 0$ magnetic interactions in the material are antiferromagnetic and $\theta_W = -T_N$, where T_N is the Néel temperature.

This law only holds for high temperatures.

Van Vleck Susceptibility

Van Vleck introduced an expression for susceptibility [1]:

$$\begin{aligned}\chi &= \frac{N_A g_J^2 \mu_B^2}{Z}\left[\frac{1}{k_B T}\sum_i \left|\langle\Gamma_i|\, J_z\, |\Gamma_i\rangle\right|^2 \exp\left(\frac{-E_i}{k_B T}\right)\right] \\ &\quad + \frac{2N_A g_J^2 \mu_B^2}{Z}\left[\sum_{i,j}\frac{\left|\langle\Gamma_i|\, J_z\, |\Gamma_j\rangle\right|^2}{E_j - E_i}\exp\left(\frac{-E_i}{k_B T}\right)\right]\end{aligned} \tag{1.10}$$

$$Z = \sum_i g_i \exp\left(\frac{-E_i}{k_B T}\right) \tag{1.11}$$

where Z is the partition function and J_z the z-component of the total angular momentum J. $|\Gamma_i\rangle$ are the eigenstates of the Hamiltonian which has energy given by E_i where the number of identical E_i terms are taken into account by introducing a degeneracy factor g_i.

1.1.3 Interactions of magnetic ions

Direct exchange

The direct exchange interaction occurs due to the orbital overlap of two atoms resulting in a correlation of their electrons. Coulombic repulsion is minimized and the Pauli exclusion principle satisfied by keeping the electrons well separated and anti-parallel.

Superexchange

The superexchange interaction is mediated by an intermediate ligand or anion (often oxygen). Superexchange interactions are usually antiferromagnetic, but ferromagnetic exchange may occur depending on the specific geometry of the orbitals and angles involved. Superexchange pathways are short, usually connected to nearest neighbours, though it can extend to second or third nearest neighbors.

Dipolar interactions

The dipolar interaction is present in all magnetic materials. It is, however, a weak effect and only becomes significant at low temperature for large moments. It is anisotropic and falls off as $1/r^3$.

1.2 Geometric magnetic frustration

1.2.1 Introduction to frustration

Consider the spins on the corners of a triangle as shown in figure 1.1 with the exchange interaction given by:

$$H_{ex} = -J \sum_{\langle i,j \rangle} \hat{\mathbf{S}}_i \cdot \hat{\mathbf{S}}_j \tag{1.12}$$

For an antiferromagnetic material the geometry does not allow all local interactions to be simultaneously minimised. In this case the ground state does not correspond to the

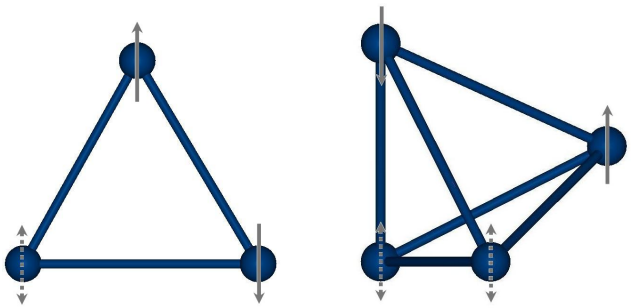

Figure 1.1: Frustrated triangle and tetrahedra: The orientation of two spins in the triangle or tetrahedron frustrates the choice of spin orientation for the remaining spins in antiferromagnets. The double arrow on the ion depicts two degenerate spin orientations. An ensemble of triangles in an ordered lattice leads to a large number of degenerate ground states.

minimum of the interaction of every spin pair leading to frustration.

Initial examples of geometric frustration (GF) were discovered over fifty years ago in the studies of Ising antiferromagnets on a triangular lattice [2] and hexagonal lattice [3] and with the work by Anderson [4]. The current concepts of frustration were not formally considered until the work of Toulouse [5] and the work by Villain on spin glasses [6, 7]. There are a number of recent reviews on geometrical frustration due to the increased interest in this field [8–12].

A signature of frustration is magnetic ordering occurring well below θ_W. Ramirez [8] and Moessner [9] proposed to use this behaviour to define an empirical measure of frustration through the following relationship:

$$f = -\frac{\theta_W}{T_c} \tag{1.13}$$

where T_c represents any cooperative ordering transition temperature. $f > 1$ corresponds to frustration with the higher the f value the more pronounced the frustration effects.

Theoretically 2d and 3d cases of geometric frustration can be realised in an almost limitless number of possible structures, however in practice this is limited by the avail-

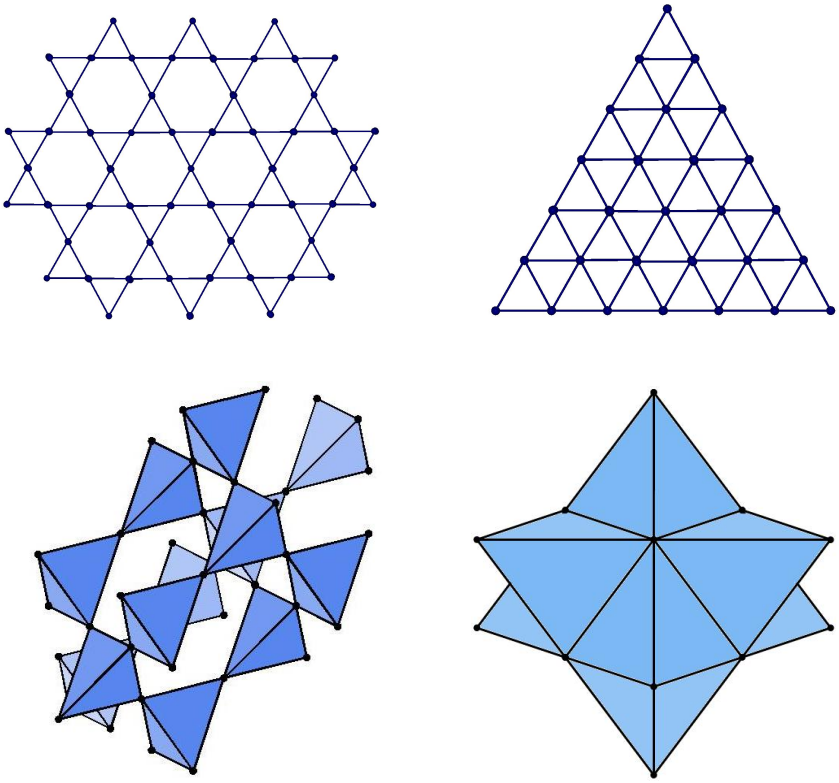

Figure 1.2: Top: 2d corner sharing kagomé lattice and edge sharing triangular lattices. Bottom: 3d corner sharing tetrahedra found in the pyrochlores and spinels, and edge sharing tetrahedra forming an fcc lattice found in the double perovskites.

ability of suitable substances [13]. Four of the most simple structures are shown in figure 1.2.

2d case: Kagomé lattice

Compounds containing the kagomé lattice are found among the Jarosite materials [14, 15], which were the subject of much of the early study of geometric frustration. More recently the experimental realisation of the Herbertsmithites, $ZnCu_3(OH)_6Cl_2$, has renewed interest in finding a true realisation of the spin-$\frac{1}{2}$ kagomé lattice model [16].

3d case: Pyrochlores

Greedan and Reimers [17–19] were responsible for many of the early studies of pyrochlores. Some of the initial pyrochlore compounds studied belonged to the series $R_2Mo_2O_7$ (R = Nd, Tb, Y). They were found to have a spin glass transition at low temperature despite having a well ordered structure.

Further research on the pyrochlores has revealed various exotic low temperature ground states. $Tb_2Ti_2O_7$ has been shown to be a spin liquid [20]. "Spin ice" materials $Ho_2Ti_2O_7$ and $Dy_2Ti_2O_7$ have been observed [21,22]. Their spins behave analogously to water ice obeying the "two-in two-out" rule. Spin ice research has led to the discovery of magnetic monopoles [23] and due to their movement within the material "magnetricity" has been measured [24].

Rosenkranz et al. showed in ref. [25] that the crystal field played a dominant role in determining the orientation of the spins in $Ho_2Ti_2O_7$ and hence they could explain why the ground state spin structure was adopted. The results were used to predict that $Dy_2Ti_2O_7$ should also be a spin ice and helped explain why $Tb_2Ti_2O_7$ behaves as a spin liquid.

1.3 Rare earth double perovskites: a model system

Karunadasa et al. [26] proposed that rare earth double perovskites form a new model three dimensional geometrically frustrated system. The investigation of two members of this series, Ba_2HoSbO_6 and Ba_2ErSbO_6, will be carried out in this thesis.

The compounds investigated here belong to the $A_2BB'O_6$ class of double perovskites where A is generally an alkaline earth with only the B site carrying a magnetic moment from a rare earth ion, and for which there is perfect ordering between the B and B' sites,

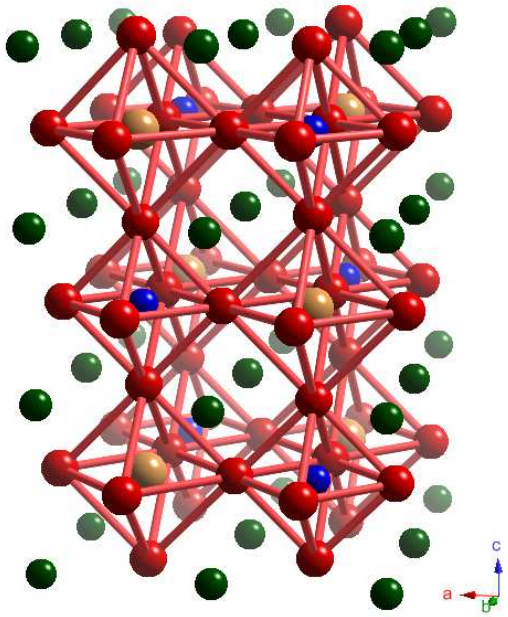

Figure 1.3: The double perovskite structure $A_2BB'O_6$ composed of two interpenetrating *fcc* lattices of magnetic rare earth ions (orange) and non-magnetic ions (blue) surrounded by six oxygen ions (red) in an octahedral arrangement. The green ion denotes the alkaline rare earth, e.g. barium.

see figure 1.3. The magnetic lattice in this case is composed of edge sharing tetrahedra forming a face centred cubic (*fcc*) lattice, as shown in figure 1.4(a).

There are many books dedicated to the perovskite structure due to its versatility in hosting a large array of ions [27,28], along with much current work [29–35]. Karunadasa et al. makes reference to a selection of these similar studies but their work appears to be the first to point out the importance of double perovskites with respect to frustration.

There are conflicting ideas from the literature as to the expected ordering of spins on the *fcc* lattice. An early theoretical study on the antiferromagnetic *fcc* lattice using the Ising model predicted a high degeneracy for the ground state with clusters forming [36]. For this Ising model in the limit of a large number of sites the entropy per spin tends to zero as the temperature tends to 0 K and the susceptibility is zero at 0 K.

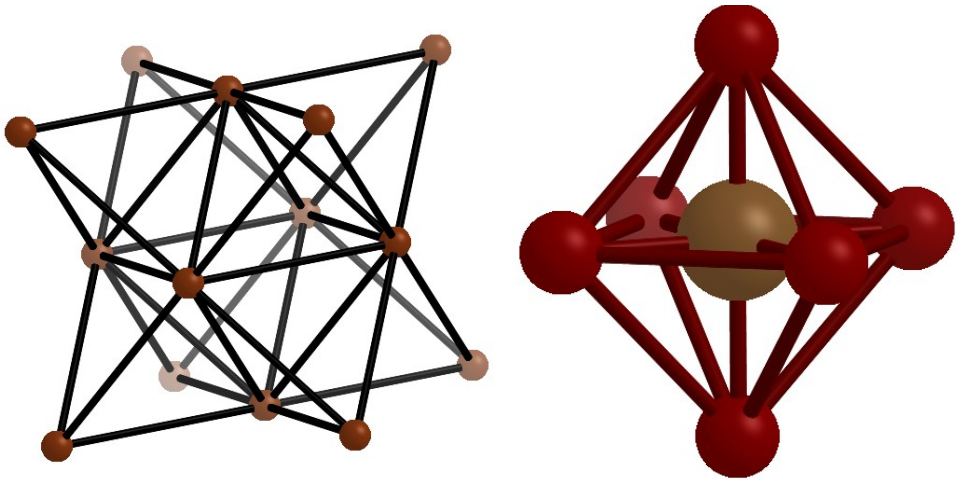

(a) (b)

Figure 1.4: (a) The rare earth ions sit on the corners of edge sharing tetrahedra in an *fcc* lattice. Each rare earth ion is connected to twelve nearest neighbours resulting in a highly connected lattice. (b) The rare earth ion surrounded by six oxygen ions in an octahedra structure.

Similar investigations have also proposed the possibility of continuous degeneracy [37]. Subsequent theoretical studies have been performed using a Monte Carlo simulation [38, 39]. The most likely ordering for the *fcc* lattice appears to be through "order by disorder" [40]. This concept was originally proposed by Villain in his seminal work on frustration [41] and later confirmed to be present in the pyrochlore $Er_2Ti_2O_7$ [42].

1.3.1 Previous work on Ba_2RSbO_6 (R = Ho, Er)

Reference	θ_W (K)	Space group	a (Å)
[43]	No data	Er and Ho $Fm\bar{3}m$	Ho/Er: $8.417(1)$/$8.397(1)$
[44]	No data	Er: $Fm\bar{3}m$	Er : $a = 8.3960(1)$
[45] and [46]	Ho: -5.46854	Ho: $Fm\bar{3}m$	Ho: 8.3712
[47]	Ho: -5.6	Ho: $Fm\bar{3}m$	Ho: $8.4170(2)$
[26]	Ho: $-4.7(2)$	$Fm\bar{3}m$	Ho: $8.4119(1)$

Table 1.1: Characterisation results from the literature for Ba_2RSbO_6, (R = Ho, Er).

Ba_2HoSbO_6 and Ba_2ErSbO_6, along with other rare earth variants (Ba_2RNbO_6, R =

Nd, Sm, Eu, Gd, Tb, Yb), were characterised by Casado et al. through x-ray powder diffraction [43]. The Ho and Er variants were reported to adopt the cubic space group $Fm\overline{3}m$, with $a = 8.417(1)$ Å for Ho and $a = 8.397(1)$ Å for Er.

Neutron powder diffraction was recently carried out on Ba_2ErSbO_6, which confirmed the space group $Fm\overline{3}m$, with $a = 8.3960(1)$ Å [44]. There do not appear to be any diffraction measurements below room temperature in the literature for Ba_2ErSbO_6, and no susceptibility or specific heat measurements have been reported.

Ba_2HoSbO_6 has been more widely investigated experimentally. Ambient temperature neutron powder diffraction on Ba_2HoSbO_6 again found the cubic space group $Fm\overline{3}m$, with $a = 8.4240(3)$ Å [47]. Susceptibility measurements in the range 2-350 K were reported showing Curie-Weiss behaviour above 10 K and $\theta_W = -5.6$ K.

Measurements on a single phase ceramic substrate of Ba_2HoSbO_6 reported the space group $Fm\overline{3}m$ with lattice constant of $a = 8.3712$ Å [45]. Susceptibility measurements were performed and gave $\theta_W = -5.47$ K [46].

Karunadasa et al. [26] characterised Ba_2HoSbO_6 by room temperature neutron powder diffraction to have the space group $Fm\overline{3}m$, with $a = 8.4119(1)$ Å. Susceptibility measurements down to 2 K showed no ordering, with $\theta_W = -4.7(2)$ K.

1.3.2 Compounds with a similar structure to Ba_2HoSbO_6 and Ba_2ErSbO_6

The rare earth perovskite series Ba_2RSbO_6 (*R* = Rare earth ion) were initially investigated by Blasse [48]. It was shown that Ba_2GdSbO_6 is cubic with space group $Fm\overline{3}m$.

The related series Ba_2RTaO_6 was investigated and found to remain paramagnetic down to 5 K [49]. For Dy-Lu, including Ho and Er, the crystal structure reported from x-ray diffraction was $Fm\overline{3}m$.

Characterisations of the group Ba_2RBO_6 (B = Nb, Ta, Ir, Ru, Bi and Sb) by Kennedy et al. [50] have shown that four space groups are favoured for the double perovskite structure: cubic $Fm\overline{3}m$, tetragonal $I4/m$, rhombohedral $R\overline{3}$ and monoclinic $I2/m$. The symmetry adopted is determined by the different sizes of the rare earth ions causing the octahedra to tilt to differing degrees. The crystal symmetry can also alter with temperature. For example x-ray powder diffraction for Ba_2HoTaO_6 has shown that a transition from space group $Fm\overline{3}m$ to $I4/m$ occurs around 260 K [50]. This highlights the importance of measuring if Ba_2HoSbO_6 and Ba_2ErSbO_6 remain in their ideal cubic structure down to low temperatures.

One of the few mentions of frustration in the double perovskites is in ref. [51] in which the compounds Ba_2RMoO_6 (R = Nd, Sm, Eu, Gd, Dy, Y, Er and Yb) are investigated. All the compounds magnetically order except Ba_2YMoO_6 and Ba_2YbMoO_6 which remain in the paramagnetic regime down to 2 K which is explained as being due to the geometrical frustration inherent in the crystal structure.

1.3.3 Tolerance factor

The structures of Ba_2HoSbO_6 and Ba_2ErSbO_6 have been shown to be cubic at room temperature, however there are no measurements at low temperature. Since the temperature of interest is below $\sim$5 K, it would be advantageous to have evidence as to whether the structure remains cubic. One such way to gain insight is to calculate tolerance factors and a program has been developed by Lufaso et al. called SPuDs [52] which does this for the perovskite structure.

The Goldschmidt tolerance factor, t, is given by:

$$t = \frac{(R_A + R_O)}{\sqrt{2}(R_B + R_O)} \tag{1.14}$$

where R_A is the ionic radius of A, R_B is the ionic radius of B, and R_O is the ionic radius

of oxygen. SPuDs calculates these values as a function of temperature. The values calculated using this program are shown in table 1.2.

	300 K	5 K
Ba_2HoSbO_6	$t = 0.972$	$t = 0.963$
Ba_2ErSbO_6	$t = 0.981$	$t = 0.974$

Table 1.2: Tolerance factors, t, calculated using SPuDs [52].

The tolerance factor can be used to predict the possibility of any lattice distortions.

- For $t = 1$ the A cation is an ideal size and no distortions of the cubic structure are expected.
- For $t > 1$ the A cation is too large and this can lead to distortions.
- For $t < 1$ the A cation is too small and octahedral tilting distortions can occur.

The results in table 1.2 suggest that the structure may alter between 300 K and 5 K, with Ba_2HoSbO_6 being slightly more likely to change. Glazer stated that octahedral tilting is the most important factor determining the space group of a perovskite [53]. It is therefore necessary to confirm the structure down to low temperatures.

Ba_2SmSbO_6 was found to be cubic from x-ray and neutron powder diffraction [54], however the tolerance factor was found to be $t = 0.977$, which deviates from unity to a similar degree as the calculated tolerance factor for Ba_2HoSbO_6 and Ba_2ErSbO_6. An explanation is that the double perovskite structure $A_2BB'X_6$, as opposed to the perovskite ABX_3, has a further degree of freedom to relieve tension. For ABX_3 the only variable parameters is the volume of the cell. For the double perovskite there is the additional parameter of the position of the X-anion between the B and BO cations, which is able to be adjusted to relieve tension.

1.4 Frustrated systems with non-magnetic crystal field ground states

A crucial factor in the study of the magnetic properties of rare earth systems is the crystalline electric field at the rare earth site, which determines the electronic states of the ion. A pertinent example is the related elpasolite series A_2BRX_6 [32, 55–60] (A, B = Li, Na, K, Rb, and Cs; R is a rare earth; X = F, Cl), which contains an *fcc* lattice of rare earth ions. It has been shown that CEF effects generally dominate those arising from magnetic coupling. For non-Kramers ions the materials behave as Van Vleck paramagnets with a non-magnetic ground state. While for Kramers ions the systems order at low temperature. Calculations based on crystal field theory gave reasonable fits to the measured magnetic susceptibility data [32, 55, 56] and optical spectra [58, 59], indicating that the magnetic behaviour is well explained by a model of uncoupled ions.

Bleaney is responsible for much of the early work on non-magnetic ground states on unfrustrated materials [61]. He focuses on non-magnetic doublets, particularly those labelled Γ_3.

A study of $TbBe_{13}$ around the same time [62] showed how the small separation of the Γ_3 doublet to a non-magnetic singlet ($\sim$0.7 K) resulted in an induced moment system responsible for the magnetic screw-type structure observed below 16 K. This was reported as a unique case.

Another early example of relating frustration and CEF effects was in the frustrated RMn_2 compounds [63]. In this system there is instability in the antiferromagnetism. It is proposed that along with frustration the CEF leads to instability in which magnetic and non-magnetic sites coexist, as revealed by differing distances between the Mn-Mn distances.

$Tb_2Ti_2O_7$ has been studied widely in terms of frustration due to its lack of ordering down to low temperature with the ground state described as a spin liquid. Molavian *et al.*, however, argue that it can also be described as a quantum spin ice with virtual crystal field excitations in a non-ineracting tetrahedral model leading to non-trivial interactions in this frustrated system [64].

Recent work on $PrAu_2Si_2$ found that dynamical fluctuations of CEF levels destabilized the induced moments created from the non-magnetic GS and magnetic first excited level and frustrate the development of long range order [65]. As a result the system goes through a spin glass transition despite the crystal structure being completely ordered. A large distribution of exchange interactions and the small energy gap between the GS and first excited CEF level is postulated to result in this novel behaviour. It is known frustration can result from lattice or structural disorder but this is the first evidence of frustration being caused by dynamical fluctuations at a phase boundary.

Neutron scattering, susceptibility and specific heat investigations on Pr_3In suggested that the antiferromagnetic order which occurs at 12 K arises from an induced moment in the non-magnetic singlet ground state [66]. A non-magnetic Γ_3 ground state is known to play a role in non-magnetic heavy Fermion behaviour [67] and the phenomenon of enhanced nuclear magnetism [68].

Thus, a careful study of model frustrated systems with Γ_3 ground states would seem to be an interesting avenue by which to explore frustration.

1.5 Spin-charge frustrated systems

1.5.1 Introduction to spin-charge frustration

The investigation of frustrated systems arising purely from the geometry of local spin interactions on a regular lattice has been considered above. The effect of charge frustra-

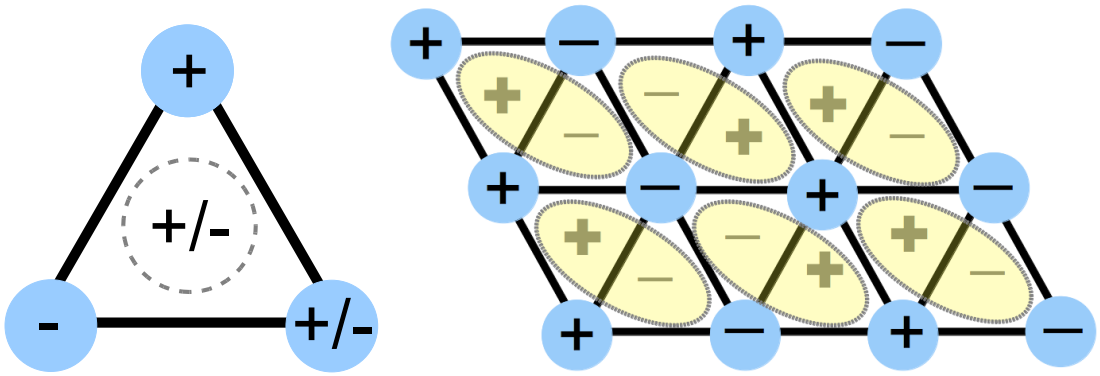

Figure 1.5: Charge frustration: (Left) If there are two differently charged ions then there is competition as to where to place the charges to minimise electrostatic interactions. This example shows a positive and negative charge competition, but it is equally prevalent for charges of the same sign, for example one ion with charge 2+ and one with charge 3+. Either of these cases leaves a charge imbalance associated with the triangle. (Right) Possible charge ordering on a triangular lattice.

tion allows a further avenue in which to explore this phenomenon. Charge frustration describes the situation in which, due to the symmetry of the crystal structure, it is not possible to minimize all local electrostatic interactions between neighboring ions.

As with geometrical magnetic frustration, charge frustration is prevalent on triangular lattices, as is shown in figure 1.5. Although the overall charge will sum to zero charge frustration effects become important if a lattice is formed of a triangular layer. This leads to local competition if there is an equal number of differently charged ions as to where they will be placed on the lattice. It is possible to arrange the ions in such a way as to minimize the electrostatic interactions, such as having alternative stripes of the same charged ions, as in figure 1.5(right). However, in real systems there will be other competing effects. If one of these effects is geometric magnetic frustration then the system will be "spin-charge" frustrated, i.e. there is competition between spin and charge ordering leading to degeneracies of both [69]. The importance of charge order has been highlighted in recent work on the pyrochlores [70, 71].

1.5.2 An example of a spin-charge frustrated system: $LuCuGaO_4$

Structure of $LuCuGaO_4$

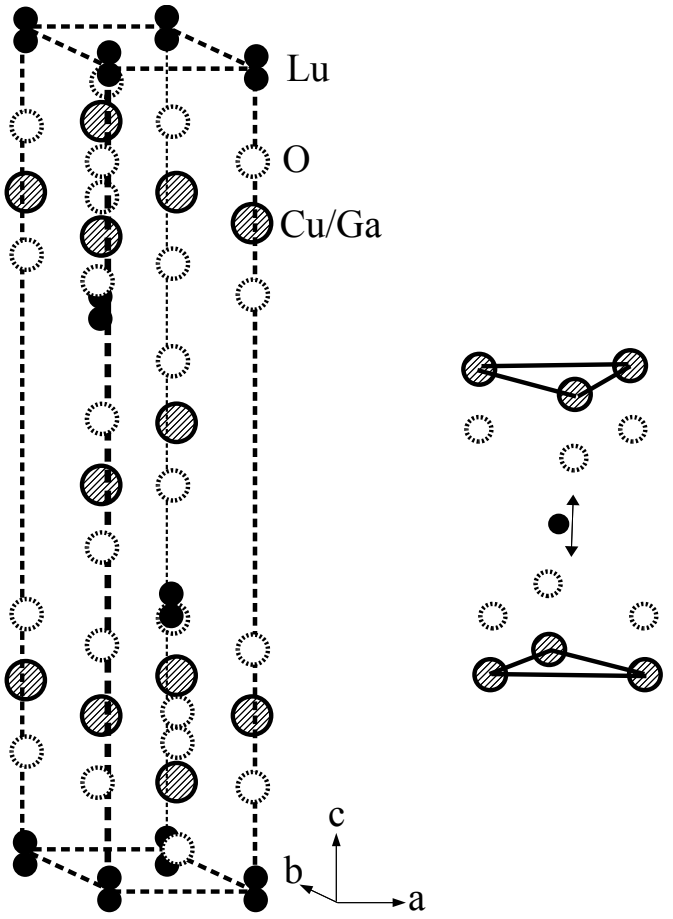

Figure 1.6: (Left) Overall structure of $LuCuGaO_4$ with the double layers of Cu^{2+} and Ga^{3+} separated along the c-axis by Lu^{3+} ions. (Right) The Lu ions are situated between the bilayers directly above (or below) the triangles formed by the Cu/Ga ions, suggesting the c-position of the Lu ion is directly controlled by the ordering on the bilayers.

The structure of $LuCuGaO_4$ is shown in figure 1.6. $LuCuGaO_4$ is a member of the series $R^{3+}M^{2+}M'^{3+}O_4$ where R is a small rare earth such as Yb^{3+} or Lu^{3+}, and M and M' are late $3d$ transition metals such as Fe^{2+} and Fe^{3+} or Cu^{2+} and Ga^{3+}. M and M' can either both be magnetic ions (non-dilute case) or a mixture of magnetic and non-magnetic ions (dilute case). The crystal structure has the space group $R\bar{3}m$. The

transition metal ions form double layers of $M^{(\prime)}O_5$ triangular bipyramids connected by triangular layers of RO_6 octahedra. The R^{3+} ions lie at the centre of distorted octahedra of O^{2-} ions, directly above and below the centre of triangles of transition metal ions. Observed down the c-axis the cation bilayers show a kagomé geometry, see Fig. 1.7. This geometry is expected to result in $LuCuGaO_4$ being a spin-charge frustrated system.

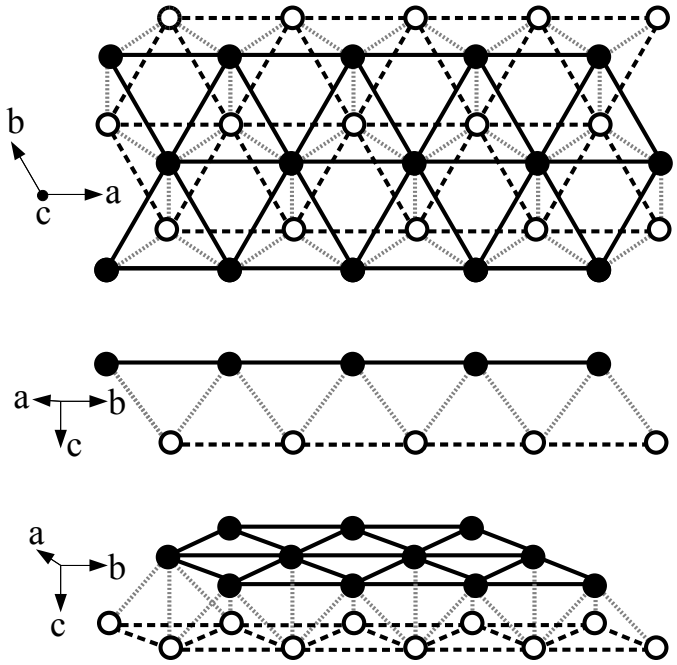

Figure 1.7: The bilayers of Cu^{2+} and Ga^{3+} triangular nets viewed along various directions showing nearest neighbour interactions in and between the layers.

Previous investigations of $LuCuGaO_4$ and related compounds

Cava et al. carried out ac and dc-susceptibility measurements on $LuCuGaO_4$ [72]. $\theta_W = -69$ K was reported with no ordering down to 2 K, strongly suggesting a highly frustrated system. The ac-susceptibility and specific heat results showed a broad peak around 0.4 K which was attributed to a spin glass transition in ref. [72], however this thesis questions this conclusion. There is no other information in the literature regarding

the magnetic properties of $LuCuGaO_4$.

Several combinations of related materials with M and M' have already been studied. An extensive literature exists concerning $LuFe_2O_4$ where charge order between Fe^{2+} and Fe^{3+} is possible and is thought to underlie the multiferroicity [73, 74]. Numerous examples are known where the two cations are different and their ordering is therefore frustrated. As well as $LuCuGaO_4$, YbMFeO$_4$ (M = Mg, Fe, Co, Cu), $YbCuGaO_4$, LuMFeO$_4$ (M = Zn, Fe, Co, Cu) and $LuCoGaO_4$ have all been studied [72, 75–85]. Structurally all are characterised as having M and M' randomly distributed on the bi-layers. With the exception of RCuGaO$_4$ (R = Yb, Lu) all these materials exhibit a splitting of field cooled and zero field cooled magnetic susceptibilities at temperatures of the order 20 K (and in some cases considerably more) indicative of freezing or spin glass transitions.

There was no indication of long range magnetic order in previous neutron diffraction studies on this series, however extra scattering was observed for $LuCuFeO_4$, $LuZnFeO_4$ and $LuCoGaO_4$ in a broad peak around 1.28 Å^{-1} in Q at 11 K [72]. There is no mention of similar scattering in $LuCuGaO_4$, however this could be due to the small magnetic moment of Cu^{2+}.

Polarised neutron powder diffraction, along with standard neutron diffraction, was carried out on YFe_2O_4 [86]. Low angle magnetic scattering, which could not be indexed to a long range structure, was again observed. This, interestingly, suggests that the main magnetic features for dilute and non-dilute triangular layers are the same [85].

The dilute case of triangular layers in this series has been most extensively investigated for $LuFeMgO_4$ [77–81]. A peak around 1.25 Å^{-1} in Q from neutron scattering has been modelled to short range two dimensional magnetic correlations by Wiedenmann et

al. using the following neutron cross section [77]:

$$\frac{\mathrm{d}\sigma}{\mathrm{d}\Omega} = 0.27^2 F^2(Q) \sum_i C_i \left[a_i \left(\frac{\sin(Qr_i)}{Qr_i} \right) + b_i \left(\frac{\sin(Qr_i)}{(Qr_i)^3} - \frac{\cos(Qr_i)}{(Qr_i)^2} \right) \right] \quad (1.15)$$

where $F^2(Q)$ is the form factor, C_i is the number of spins connected to a given spin at a distance r_i and the coefficients a_i and b_i describe the correlations between the spins.

It is suggested that the random dilution of cations leads to the formation of clusters resulting in two types of site for the magnetic cation: (i) those lying in the body of clusters and having close to the full complement of magnetic neighbours, and (ii) those lying on extended branches of clusters and having just one or two neighbours [77, 78, 80, 81].

The spins in category (i) are highly frustrated while the spins in category (ii) have their frustration minimized due to having the number of nearest neighbours limited. From Monte Carlo studies this distribution of spins matched most accurately the experimental susceptibility, specific heat and neutron scattering results available. The idea of clusters has been introduced for $LuFe_2O_4$ from early neutron scattering studies [74, 87]. 2D spin-glass like ferrimagnetic order is observed and explained due to clusters of different sizes within the triangular layers, this will be investigated further in chapter 5.

1.6 Aims of the present work

This thesis will investigate frustration in magnetic oxides. This chapter has served as an introduction to the general concepts used in this investigation. The main experimental techniques and instruments used are introduced in chapter 2. The present work was motivated by various aspects of geometrical frustration, already discussed. The rare earth double perovskites have the signature of frustration and their similarity to the highly frustrated rare earth pyrochlore series points towards interesting and novel behaviour.

Various aims need to be met to investigate this further:

- Confirm crystal structure down to low temperature for Ba_2HoSbO_6 and Ba_2ErSbO_6.
- Measure magnetic correlations through neutron scattering.
- Solve the crystal field level scheme and use this to predict experimental properties.

These will be carried out in chapter 3.

Charge frustration and geometric magnetic frustration are investigated in chapter 4 through an experimental study of $LuCuGaO_4$. It has been previously predicted to undergo a spin glass transition around 0.4 K, this will be tested through:

- Structural characterisation and susceptibility to confirm previously reported results.
- Low temperature polarised and inelastic neutron scattering to investigate magnetic correlations.
- μSR to investigate the local spin correlations and compare to the neutron results.

Finally, a novel μSR technique is introduced. The effectiveness of the technique is tested through a calibration experiment and numerical simulation of the results. Results from an experiment on a frustrated magnetic oxide using this technique will be presented in chapter 5.

Chapter 2

Experimental Techniques

2.1 Neutron scattering

2.1.1 The neutron as a probe

Chadwick discovered the neutron in 1932 [88]. The de Broglie wavelength for thermal neutrons is $\lambda = \frac{h}{m_n v} = 1.8$ Å, where the velocity, v, is taken as 2.2 km/s and the neutron mass is $m_n = 1.675 \times 10^{-27}$ kg [89]. The temperature is given by $T = (m_n v^2)/2k_B = 293$ K. The wavelength corresponds to typical interatomic distances. The neutron is uncharged which allows it to penetrate deep into matter without being affected by Coulomb forces, instead scattering from the nucleus through the strong nuclear force. The neutron also carries an intrinsic magnetic moment of $\mu_n = 1.913\mu_N$ which means it can be used to obtain magnetic information by interacting with unpaired electrons through magnetic dipole forces. The neutron is therefore ideal for studying magnetic condensed matter systems and numerous texts describe neutron scattering thoroughly [89–92].

2.1.2 Production of neutrons and delivery to instruments

Neutron scattering experiments are carried out at large scale facilities of two general kinds: reactor and spallation sources.

The Institut Laue-Langevin (ILL) is located in Grenoble, France. It is a reactor

source and works through nuclear fission to produce neutrons (n) in the chain reaction:

$$^{235}\mathrm{U} + \mathrm{n} \rightarrow \mathrm{Kr} + \mathrm{Ba} + 2.5\mathrm{n}$$

The neutrons produced have a spectrum of energies and wavelengths which can be controlled by varying their temperatures to select the desired wavelength range, which follows a Maxwell-Boltzmann distribution.

ISIS is the leading pulsed neutron source and is located at the Rutherford Appleton Laboratory near Oxford, UK. Pulses of protons from a synchrotron are collided with a heavy metal target of tantalum with the production of around 30 neutrons per incident proton.

2.1.3 Use of cross-sections to describe scattering

Consider an incoming beam of neutrons scattering from a sample due to interactions between the neutron and the nucleus as shown in figure 2.1. A neutron detector can measure the number of neutrons scattered into the known area of the detector and record their energy. The distance of the counter from the target is large compared to the dimensions of the counter and the target so the area, $\mathrm{d}\Omega$, is well defined. This angular dependence of the scattering process can be defined by:

$$\frac{\mathrm{d}\sigma}{\mathrm{d}\Omega} = \frac{\text{number of scattered particles into } \mathrm{d}\Omega}{\text{flux} \times \text{time} \times \mathrm{d}\Omega} \tag{2.1}$$

The measured energy can be taken into account through the partial differential cross-section:

$$\frac{\mathrm{d}^2\sigma}{\mathrm{d}\Omega \mathrm{d}E} = \frac{\text{number of scattered particles into } \mathrm{d}\Omega \text{ with energy transfer } \mathrm{d}E}{\text{flux} \times \text{time} \times \mathrm{d}\Omega \times \mathrm{d}E} \tag{2.2}$$

Considering the state of the system before and after the neutron scattering using $\lambda_i \rightarrow \lambda_f$ to represent the scattering system and $k_i \rightarrow k_f$ for the neutron, and applying Fermi's

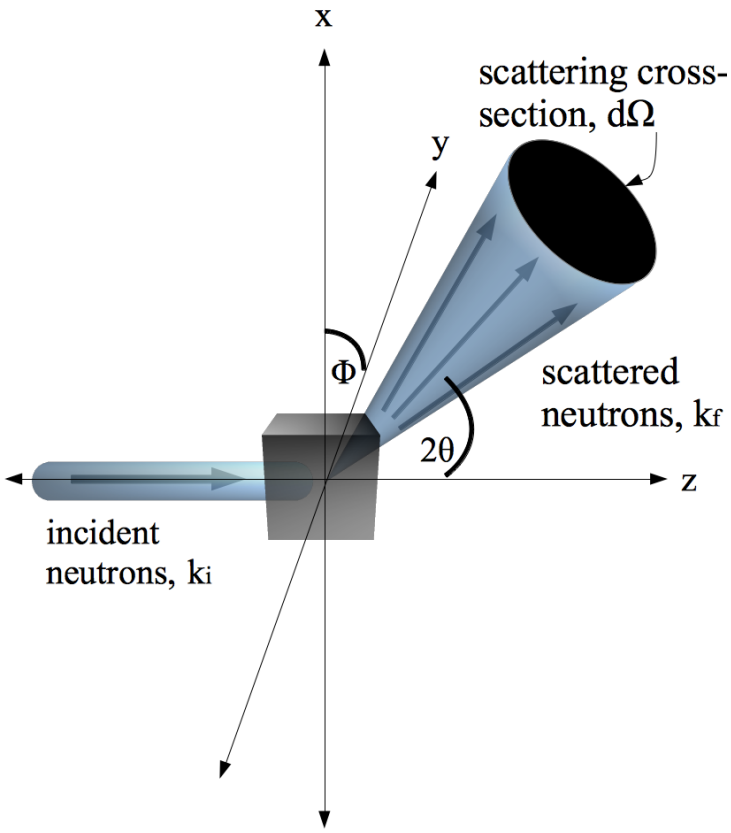

Figure 2.1: Schematic of a neutron scattering experiment. The neutron beam is scattered from a sample and the resultant scattering cross-section in the direction (θ, ϕ) detected at a detector which can be used to gain information about the sample.

golden rule to equation 2.1 for the transition between the states gives:

$$\left(\frac{\mathrm{d}\sigma}{\mathrm{d}\Omega}\right)_{\lambda_i \to \lambda_f} = \frac{k_f}{k_i}\left(\frac{m}{2\pi\hbar^2}\right)^2 |\langle k_f \lambda_f | V | k_i \lambda_i \rangle| \tag{2.3}$$

where m is the mass of the neutron and V is the potential for the neutron-nucleus system.

The next step is to consider a particular k_f. This is done by considering for fixed k_i, λ_i and λ_f for the very narrow range of $|k_f|$ values for which transitions are probable. This k_f is inserted into equation 2.3 and as a result all the scattered neutrons detected in the cross section have the same energy. The new expression for the partial differential

cross-section is:

$$\left(\frac{\mathrm{d}\sigma}{\mathrm{d}\Omega \mathrm{d}E_f}\right)_{\lambda_i \to \lambda_f} = \frac{k_f}{k_i}\left(\frac{m}{2\pi\hbar^2}\right)^2 |\langle k_f \lambda_f | V | k_i \lambda_i \rangle| \delta(E_{\lambda_i} - E_{\lambda_f} + E_{k_i} - E_{k_f}) \quad (2.4)$$

where the subscript on the energy E denotes the initial and final energies of the system (λ) and the neutron (k) with the initial and final energies of the combined system-neutron being equal. The interaction potential, V, is the sum of the nuclear part arising from the interaction of the neutron with the nucleus and magnetic potential arising from the interaction of the neutron with the magnetic field of unpaired electrons through dipolar forces. These are given by:

$$V_{\text{nucl.}} = \frac{2\pi\hbar^2}{m_n}\sum_j b_j \delta(\mathbf{r}_j) \quad (2.5)$$

$$V_{\text{mag.}} = -\lambda\hbar\hat{\boldsymbol{s}}.\mathbf{B} \quad (2.6)$$

where b is known as the scattering length and varies between nuclei, so is different for different isotopes of the same element, and also depends on the spin state of the nucleus-neutron system. $\hat{\boldsymbol{s}}$ is the operator of the neutron spin and $\mathbf{B}$ is the magnetic field in the sample.

2.1.4 Scattering from a single nucleus

The use of cross-sections applies generally to any kind of scattering. The case of scattering from a single fixed nucleus can be described by considering the incoming neutron, defined along the z-axis, as a plane wave described by the wavefunction:

$$\psi_i = \exp(ik_i z) \quad (2.7)$$

After interacting with the nucleus the scattered neutrons, whose wavelength of $\sim 10^{-10}$

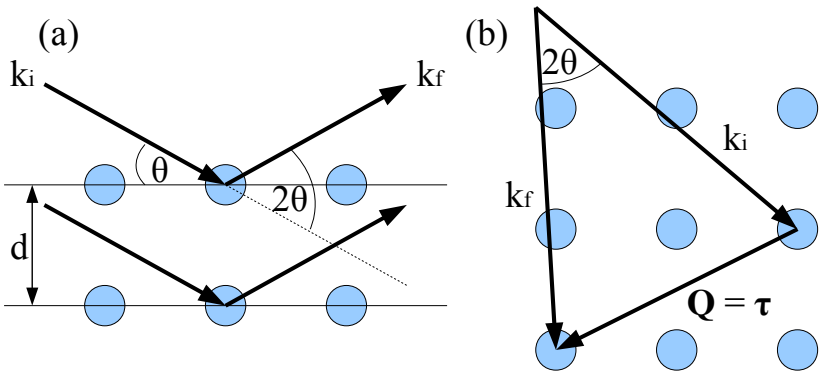

Figure 2.2: (a) Bragg diffraction showing the incoming neutrons scattering from the nuclei within the crystal. (b) Reciprocal space representation of neutron scattering. For diffraction to occur the scattering vector **Q** must equal a reciprocal lattice vector τ.

m is much larger than the nucleus size of $\sim 10^{-14}$ m, are spread out spherically symmetrically around the nucleus and can be described by:

$$\psi_i = -\frac{b}{r}\exp(ik_f r) \tag{2.8}$$

In this case $k_i = k_f$ since the energy of the neutron is too small to change the internal energy of the nucleus and the scattering is therefore elastic. r is the position of the scattered neutron.

2.1.5 Nuclear Bragg scattering

Figure 2.2(a) shows the case of Bragg diffraction from planes in a crystal separated by a distance d. The scattering system can be defined as having dimension (in direct space):

$$\mathbf{r} = n_1\mathbf{a} + n_2\mathbf{b} + n_3\mathbf{c} \tag{2.9}$$

The incoming neutrons are considered as plane waves and have a wavelength of $\lambda = 2\pi/|k|$, where $k_i = k_f = |k|$. Braggs law for diffraction is given by:

$$n\lambda = 2d\sin\theta \tag{2.10}$$

where θ is shown in figure 2.2(a) and n is an integer resulting in wavelengths separated by an integer number combining constructively.

Figure 2.2(b) shows the reciprocal lattice. The reciprocal lattice is defined with respect to the direct space lattice as:

$$\mathbf{a}^* = \frac{2\pi}{v_0}\mathbf{b} \times \mathbf{c}, \quad \mathbf{b}^* = \frac{2\pi}{v_0}\mathbf{c} \times \mathbf{a}, \quad \mathbf{c}^* = \frac{2\pi}{v_0}\mathbf{a} \times \mathbf{b} \tag{2.11}$$

where $\mathbf{a}, \mathbf{b}$ and $\mathbf{c}$ are unit vectors of the nuclear cell and v_0 is the volume of the unit cell given by $v_0 = \mathbf{a}.(\mathbf{b} \times \mathbf{c})$. The reciprocal lattice vectors of the unit cell are denoted by $\mathbf{a}^*$, $\mathbf{b}^*$ and $\mathbf{c}^*$. The direct lattice and the reciprocal lattice are related as a fourier transform pair.

For scattering to be observed the scattering vector $\mathbf{Q}$ must be equal to a reciprocal lattice vector $\boldsymbol{\tau}$, i.e. $\mathbf{Q} = k_i - k_f = \boldsymbol{\tau}$. If $\mathbf{Q} \neq \boldsymbol{\tau}$ then no coherent scattering is observed and therefore there is no scattering intensity.

The intensity of the elastically scattered neutrons is given by:

$$\left(\frac{\mathrm{d}\sigma}{\mathrm{d}\Omega}\right)_{\text{nuc. el.}} = \mathrm{N}\frac{(2\pi)^3}{v_0}\sum_{\boldsymbol{\tau}} \delta(\boldsymbol{Q} - \boldsymbol{\tau})|F_N(\mathbf{Q})|^2 \tag{2.12}$$

where N is the number of unit cells and F_N is known as the structure factor. So for a particular material $I_N \propto |F_N(\mathbf{Q})|^{\mathbf{2}}$. The structure factor is given by:

$$F_N(\mathbf{Q}) = \sum_j b_j \exp(2\pi i \mathbf{Q}.\mathbf{r}_j) \exp(-W_j) \tag{2.13}$$

where the sum is over all j atoms and $\exp(-W_j)$ is the Debye-Waller factor which takes into account the thermal motion of the atom.

In real scattering systems there is generally a variable scattering length at different sites due to nuclear spins or isotopes. This results in the cross section being separated into coherent and incoherent terms.

Coherent scattering depends on the correlation between the positions of the same nucleus at different times, and on correlations of different nuclei at different times. The result is interference effects. The coherent scattering depends on the average scattering length, assuming no correlation between position and scattering length. The coherent scattering is observed as intensity or Bragg peaks. They are either given as a function of 2θ, Q or d. These are related by:

$$Q = \frac{4\pi \sin\theta}{\lambda} = \frac{2\pi}{d} \tag{2.14}$$

Incoherent scattering only depends on the correlation of the positions of the same nucleus at different times. It does not give rise to interference effects. The incoherent scattering is due to the random distribution of deviations of the scattering lengths from the mean value.

2.1.6 Magnetic scattering

For the purposes of this work magnetic scattering can be considered in much the same way as the nuclear scattering described above with only the need to alter a few parameters. The total scattering from a sample, as a function of $\mathbf{Q}$, is given as the sum of nuclear and magnetic components:

$$\frac{\mathrm{d}\sigma}{\mathrm{d}\Omega}_{\mathrm{total}} = \frac{\mathrm{d}\sigma}{\mathrm{d}\Omega}_{\mathrm{nuc.}} + \frac{\mathrm{d}\sigma}{\mathrm{d}\Omega}_{\mathrm{mag.}} \tag{2.15}$$

$\frac{\mathrm{d}\sigma}{\mathrm{d}\Omega}_{\mathrm{mag.}}$ has the same form as equation 2.12 but now $\mathbf{k}$ is introduced to describe the magnetic order:

$$\left(\frac{\mathrm{d}\sigma}{\mathrm{d}\Omega}\right)_{\mathrm{mag.}} = \mathrm{N}\frac{(2\pi)^3}{v_0}\sum_{\tau}\sum_{\mathbf{k}}\delta(\mathbf{Q}-\boldsymbol{\tau}-\mathbf{k})|F_M(\mathbf{Q})|^2 \tag{2.16}$$

$\mathbf{k}$ is known as the propagation vector of the magnetic structure or k-vector. If $\mathbf{k} = (0,0,0)$ then the magnetic and nuclear Bragg peaks will lie on top of each other. If

$\mathbf{k} \neq (0,0,0)$ then there can be magnetic peaks at different positions to the nuclear peaks.

For magnetic scattering from a particular system $I_M \propto |F_M(\mathbf{Q})|^2$, where $F_M(\mathbf{Q})$ is given by:

$$F_M(\mathbf{Q}) = F(\mathbf{Q}) \sum_j \mathbf{m}_{\perp j} \exp(2\pi i \mathbf{Q}.\mathbf{r}_j) \tag{2.17}$$

$\mathbf{m}_{\perp j}$ is the magnetic component of the ordered moment perpendicular to $\mathbf{Q}$ on the jth atom in the unit cell and $F(\mathbf{Q})$ is known as the magnetic form factor. The magnetic form factor arises due to the magnetic moment being spread out over an atom. The form factor is present for all magnetic systems regardless of the presence of magnetic ordering or otherwise.

2.2 Neutron scattering instruments

2.2.1 The MARI spectrometer at ISIS

MARI is an inelastic neutron scattering instrument situated at ISIS [93]. It can handle incident neutron energies of 8 to 1000 meV. The neutron beam from the moderator passes through three choppers. These are the nimonic chopper which rotates at 25-100 Hz. This suppresses the prompt neutron pulse from the protons that hit the target. These high energy neutrons would thermalise in the spectrometer resulting in a sloping background on the data. The 5-50 Hz disc chopper suppresses the flux of fast delayed neutrons that form the majority of the background when running with a depleted uranium target. Finally the required neutron energies are selected by the Fermi chopper which rotates with frequencies between 50 and 600 Hz.

The instrument has a high resolution of 1-2 $\%$ of the incoming energy. The ^{3}He detector banks cover a range of 3° to 153° allowing a large range of $(\mathbf{Q}, E)$ space.

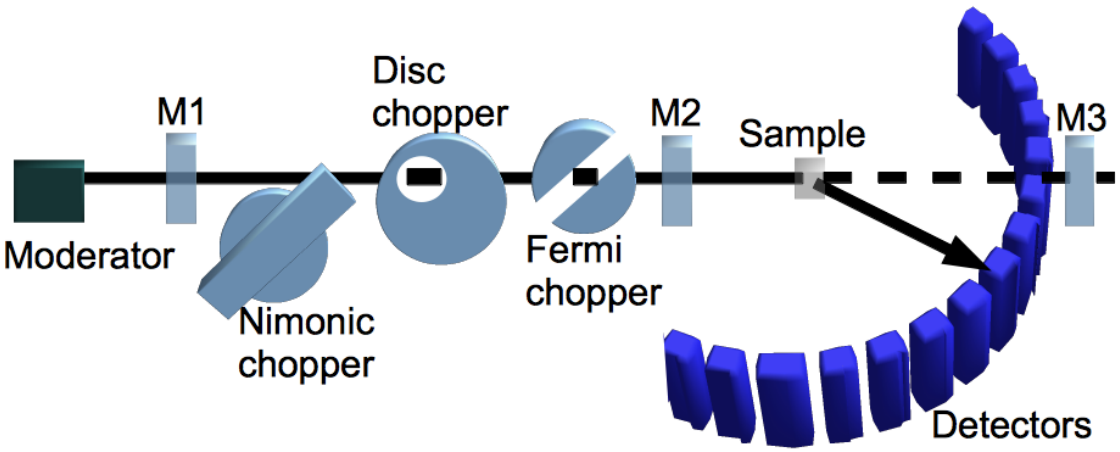

Figure 2.3: Schematic of the MARI spectrometer located at ISIS. M1, M2 and M3 corresponds to the monitors, with the distances between each monitor and the moderator accurately known.

The energies of the scattered neutrons are determined by the time taken to reach the detectors. There are currently a large amount of detectors (922) allowing the large coverage and these are split into 8 different “arms” or banks with an additional assembly of low angle banks. The data from these separate banks can be analysed along with a combination of all detectors.

2.2.2 The GEM diffractometer at ISIS

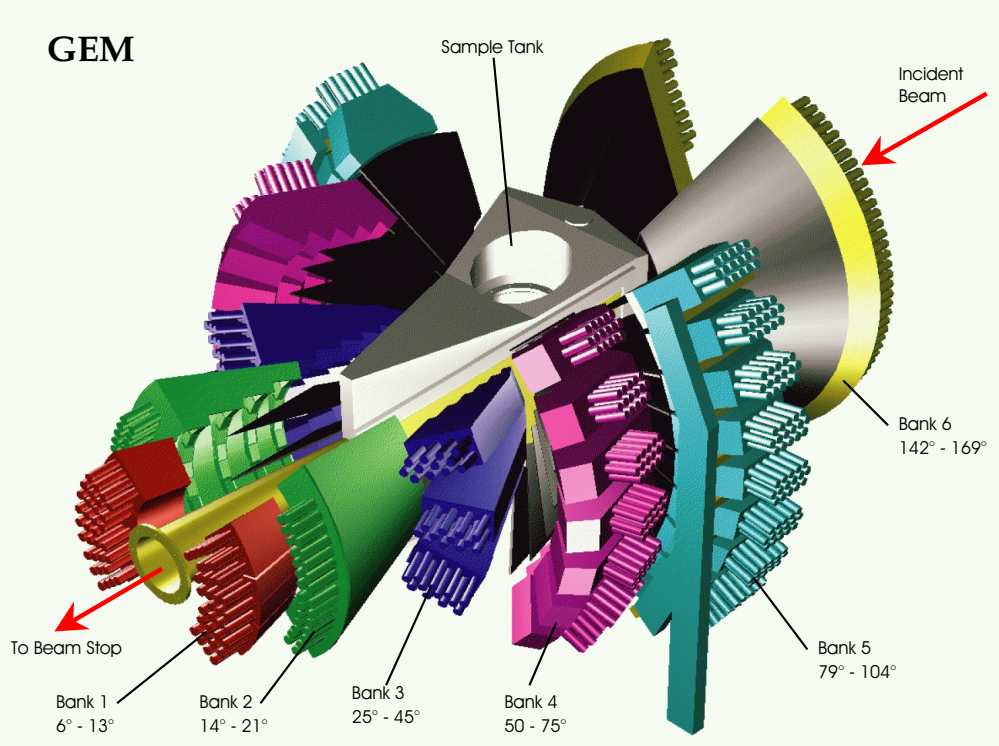

Figure 2.4: Schematic representation of the GEM diffractometer banks surrounding the sample. GEM contains 6 separate banks allowing a large range of scattering angles to be followed. Figure reproduced from ref. [94].

The General Materials diffractometer (GEM) is a high intensity and high resolution instrument at the pulsed neutron source of ISIS. The instrument and examples of its use are described in ref. [95] and on the GEM website [94]. GEM has six detector banks of zinc sulphide scintillators covering a large angle of $6°$ to $169°$. This means it lends itself well to magnetic scattering studies in the low angle banks and structural characterisation through the large amount of nuclear Bragg peaks in the high angle banks.

GEM has a similar nimonic chopper to MARI to remove the prompt pulse of neutrons which comes from the neutron source and disc choppers for restricting and setting the wavelength range and therefore preventing overlap.

2.2.3 IN4 at the ILL

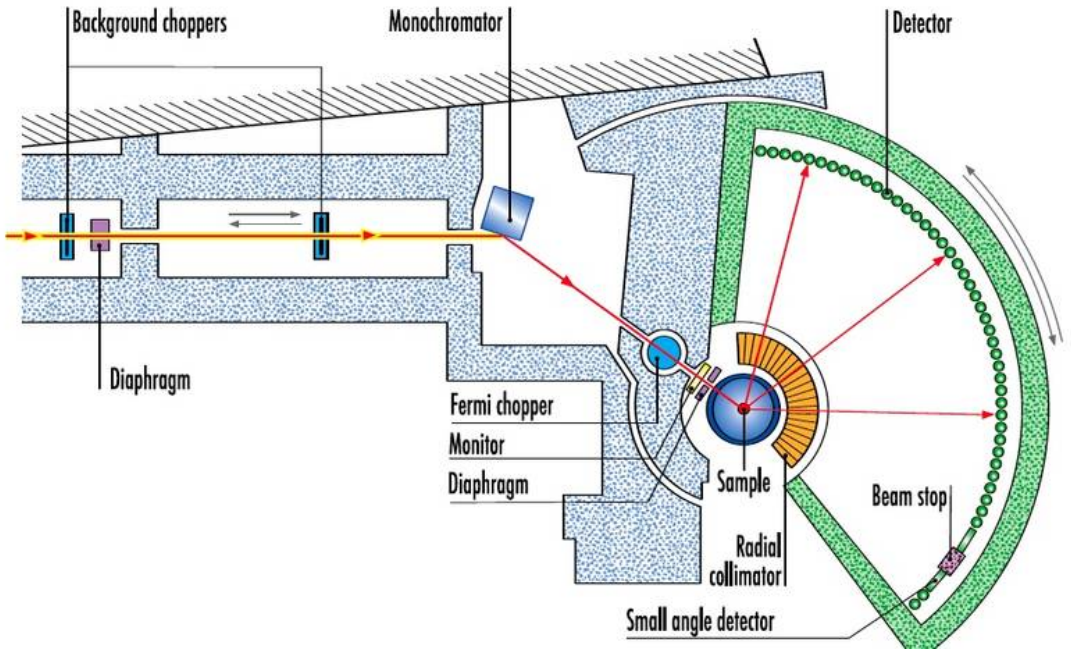

Figure 2.5: Schematic of the IN4 spectrometer located at the ILL. Figure reproduced from ref. [96].

IN4 is located at the ILL [96]. It is a time of flight spectrometer with a neutron energy range of 10-100 meV. A schematic of the instrument is shown in figure 2.5. The background choppers eliminate fast neutrons and gamma rays that cause background noise. The monochromator is an assembly of 55 copper crystals and selects the neutron energy. A Fermi chopper rotating at 40000 rpm transmits short pulses of the monochromated neutrons to the sample. The TOF for the neutrons between the chopper and the sample is accurately measured by the instruments electronics. ^{3}He detector banks cover angles up to 120° and record the scattering in $S(\mathbf{Q}, \omega)$.

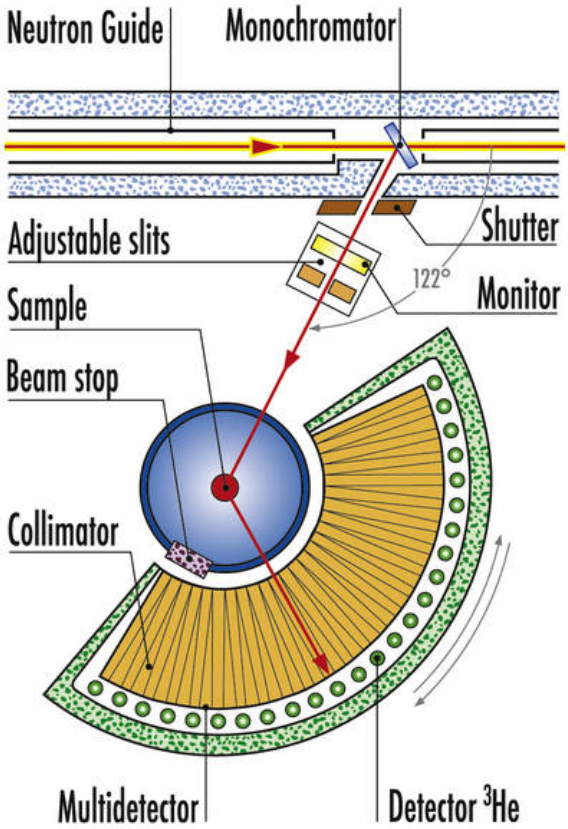

Figure 2.6: Schematic of the D1A diffractometer located at the ILL. Figure reproduced from ref. [97].

2.2.4 D1A at the ILL

The high resolution two-axis diffractometer D1A is located at the ILL [97]. It is ideally suited to structural characterisation work due to its near perfect Gaussian peak shape in the range $30°$ to $150°$ giving reliable information in as little as 2 hours. The wavelength range is 1.39 to 2.99 Å. This is selected by a monochromator consisting of 30 Ge crystals, 30 mm in height. The optimum wavelength for this instrument is 1.911 Å. The instrument has a bank of 25 high efficiency collimators and ^{3}He detectors.

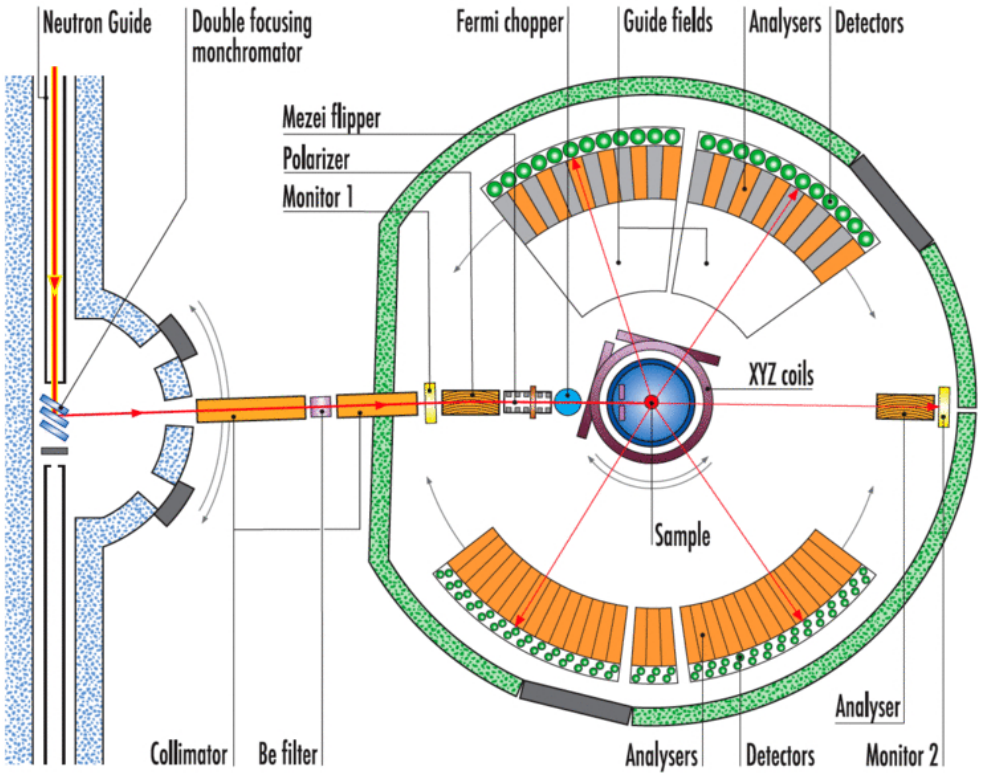

Figure 2.7: Schematic of the D7 polarised neutron analyser located at the ILL. Figure reproduced from ref. [98].

2.2.5 The D7 polarised neutron analyser at the ILL

The D7 instrument, located at the ILL, performs so called "xyz" polarisation analysis. This unambiguously separates the total scattering into a magnetic component, nuclear component and spin incoherent component. The advantage of this is that any diffuse scattering, which is generally not very intense compared to Bragg scattering and often obscured by Bragg peaks, can be observed. Its operation and theory are described on the ILL instrument website [98] and in ref. [99] and a schematic is shown in figure 2.7. The instrument can operate at three different wavelengths of 3.1, 4.8 and 5.8 Å with the wavelengths being selected by the monochromator. The operating wavelength used in this work was 4.8 Å which gave a usable Q range of 0.5 to 2.5 Å^{-1}. Once the wavelength

is selected and higher orders of the wavelength are removed by the Be-filter the incident neutron beam is polarized using supermirror benders, the polarization is assumed to be in the z-direction throughout this discussion. The neutrons are then flipped by the flipper for spin flip analysis (SF) or left unchanged for non-spin flip (NSF). The polarisation is maintained by a guide field. The polarized neutrons then pass through the sample which will cause some of the spins to flip. The scattered neutrons are then analysed by the supermirrors and the 32 multi detectors in the x-y plane. A total of six measurments are made due to measuring the SF and NSF in the x, y, z directions. These are denoted as $\frac{\mathrm{d}\sigma_{\mathrm{SF}}^{(x,y,z)}}{\mathrm{d}\Omega}$ and $\frac{\mathrm{d}\sigma_{\mathrm{NSF}}^{(x,y,z)}}{\mathrm{d}\Omega}$ and given by:

$$\frac{\mathrm{d}\sigma_{\mathrm{mag.}}}{\mathrm{d}\Omega} = \frac{\mathrm{d}\sigma_{\mathrm{SF}}^{X}}{d\Omega} + \frac{\mathrm{d}\sigma_{\mathrm{SF}}^{Y}}{\mathrm{d}\Omega} - 2\frac{\mathrm{d}\sigma_{\mathrm{SF}}^{Z}}{\mathrm{d}\Omega}$$

or,

$$\frac{d\sigma_{\mathrm{mag.}}}{\mathrm{d}\Omega} = 2\frac{\mathrm{d}\sigma_{\mathrm{SF}}^{Z}}{\mathrm{d}\Omega} - \frac{\mathrm{d}\sigma_{\mathrm{SF}}^{X}}{\mathrm{d}\Omega}.\frac{\mathrm{d}\sigma_{\mathrm{SF}}^{Y}}{\mathrm{d}\Omega}$$

As the two combinations correspond to independent measurements, the magnetic differential cross section is taken as their average.

By using a vanadium sample to normalise the measurements units of barn sr^{-1} formula unit^{-1} can be obtained for the intensity of scattering.

2.3 The μSR technique and instrumentation

2.3.1 Properties of the muon

Muons are elementary particles in the lepton family, with properties shown in table 2.1, which can be used as a unique experimental tool by implantation inside the sample. There are various books and articles describing the use of muons in condensed matter [100–104].

Charge	$+1$
Mass	$207m_e$, $\frac{1}{9}m_p$
Spin	$\frac{1}{2}$
Lifetime	2.197 μs
Magnetic moment	3.18 μ_p
Gyromagnetic ratio	$\approx 2\pi$ kHz/mT

Table 2.1: The basic properties of μ^+.

Both μ^+ and μ^- are used experimentally. For the study of magnetic condensed matter systems μ^+ is most widely used and only μ^+ is considered in this thesis.

2.3.2 Production of muons

Muons are produced by cosmic rays but their intensity is too small for effective investigations and their velocity too high to stop within standard sample sizes for condensed matter studies. The large scale production of muons began in the 1950s. Muons are produced in the following reaction chain:

$$\begin{aligned} p + p &\longrightarrow p + n + \pi^+ \\ \pi^+ &\longrightarrow \mu^+ + \nu_\mu \end{aligned}$$

The production works by firing a high energy proton beam at a target of a light element, usually graphite. This leads to various reactions with the one of importance here producing a proton (p), neutron (n) and pion (π^+).

Due to conservation of momentum the muon and neutrino produced from the pion decay have equal and opposite momentum. Since the pion has zero spin the muon spin must be equal and opposite to the neutrino spin (ν indicates a neutrino with the subscript defining which lepton the neutrino is associated with). A fundamental property of the neutrino is that its spin is aligned anti-parallel to its momentum, causing the muon spin to be similarly oriented. Therefore stationary pions are selected resulting in a 100% spin

polarized beam of spin-$\frac{1}{2}$ muons.

The muon then undergoes the following decay:

$$\mu^+ \longrightarrow e^+ + \overline{\nu}_\mu + \nu_e$$

Due to parity violation, which is a consequence of the decay involving the weak interaction, the decay positrons (e^+) are distributed asymmetrically with respect to the muon polarization, being emitted preferentially in the direction of the muon spin.

2.3.3 Using muons as a probe: μSR

Muons are used in the investigation of matter through μSR, the general label used to cover muon spin rotation, resonance and relaxation. In all instances μSR relies on the basic properties of the muon which allow (i) the high degree of spin polarization of the muons which remains unaffected by the implantation process and (ii) the asymmetry of the muon decay preferentially in the spin direction allowing the polarization to be analysed.

A schematic μSR experimental arrangement is shown in figure 2.8. A spin-$\frac{1}{2}$ polarized beam of μ^+ particles is implanted into the sample. The implanted μ^+ will reside at an area of high negative charge. In metals the μ^+ will reside at an interstitial site due to the negative conduction electrons. Alternatively the muon can pair with an electron to form a muonium (Mu) "atom".

The μ^+ undergo a precession governed by their response to either a local magnetic field within the sample or to an externally applied field in the transverse or longitudinal direction ($H_{\rm local}$). The angular frequency of this Larmor precession is given by:

$$\omega_\mu = \gamma_\mu B, \tag{2.18}$$

The gyromagnetic ratio for the muon is given by: $\gamma_\mu = ge/2m_\mu$.

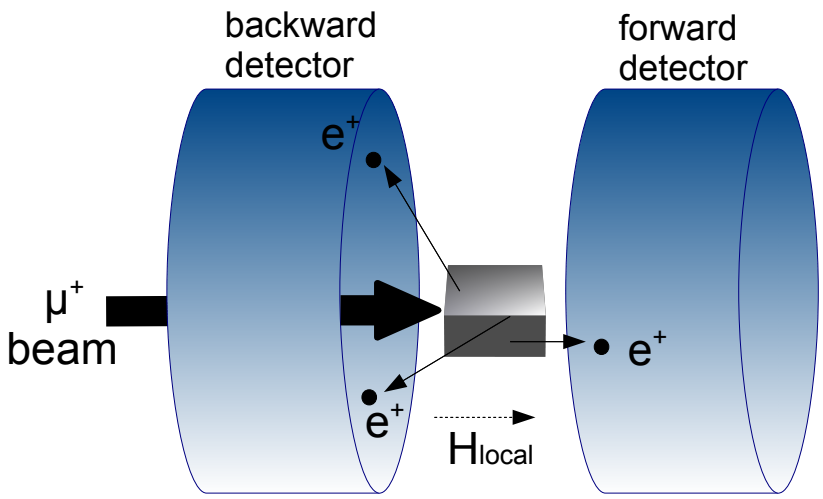

Figure 2.8: Schematic of a standard μSR experiment. The muon polarization is antiparallel to the beams momentum. Each μ^+ decays into an e^+ and is detected in one of the two detectors.

While the muon is precessing in the material it will decay into a positron. The positron is emitted in the direction of the μ^+ spin and is detected in one of the forward or backward detectors, see figure 2.8. The number of detected e^+ particles for the forward, $N_f(t)$, or backward, $N_b(t)$, detectors can be used to gain information about the local magnetic fields. Summed together $N_f(t)$ and $N_b(t)$ recover the expected exponential form for radioactive decay of the form $N_b(t) + N_f(t) = N_{total}(t) = N(0)_{total} \exp(-t/\tau_\mu)$. An asymmetry function given by the expression:

$$A(t) = \frac{N_b(t) - \alpha N_f(t)}{N_b(t) + \alpha N_f(t)}, \tag{2.19}$$

where α is an instrumental parameter, is used to find information about the time evolution of the implanted μ^+ beam. Any field surrounding the muons alters the Larmor precession frequency of the muon and the resultant relaxation envelope, manifested in the asymmetry function from the emitted positron, is used to measure magnetic properties on the time scales of nano to microsecond dynamics.

2.3.4 Implantation of muons

In a standard μSR experiment muons are implanted in high intensity beams directly into the sample under investigation with an energy of $\sim$10 MeV. The muon has a lifetime of $\tau_\mu = 2.2$ μs and decays after a time t with a probability proportional to $\exp(-t/\tau_\mu)$, defining the timescales μSR is applicable. Through ionising atoms, scattering with electrons and then finally electron capture and loss in the sample the muons reduce their energy down to a few hundred eV. These processes involve electrostatic interactions and hence leave the muons spin largely unaffected by the implantation process. The timescale for this is the order of 10^{-9} s.

The Bethe formula describes the energy loss by ionization, which is the main process involved in the stopping of muons in the sample.

$$-\frac{\mathrm{d}E}{\mathrm{d}x} = 4\pi N_A r_e^2 m_e c^2 \rho \frac{Z}{A}\frac{1}{\beta^2}\left[\ln\left(\frac{2m_e\gamma^2 v^2}{I}\right) - \beta^2\right] \tag{2.20}$$

where $r_e = 2.817 \times 10^{-13}$ m, $\beta = \frac{v}{c}$, $I =$ mean ionisation energy, $A =$ atomic weight of sample, $\rho =$ density of sample and $\gamma = \frac{1}{\sqrt{1-\beta^2}}$.

The muons range is thus dictated by the material which it is implanted in to, but as a rough guide a value for the muon range is given as 100 mg.cm^{-2} of material, which is equivalent to about 1 mm of water or 500 μm of silicon [104]. Each review on μSR points out that there inevitably is damage to the sample due to the implantation of the muons. The general consensus is that the muons cause initial damage to the sample when entering, but eventually reside in an area that is well away from any damage. Since the muon is a local magnetic probe then it is argued that it does not feel the effects from any damage that it has caused in the sample. The number of muons injected in a given measurement is also much less than the number of atoms in the sample and hence this is also believed to limit any effects of damage caused. There does not appear,

however, to be any detailed studies to prove or disprove these beliefs.

2.3.5 μSR instrument used in the present work: MuSR

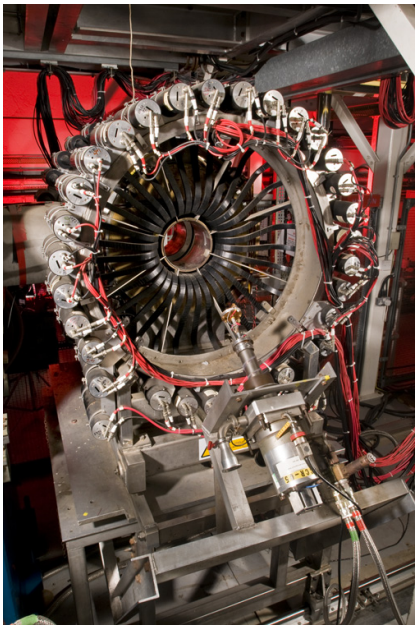

Figure 2.9: Photograph of the MuSR instrument showing the 32 forward detector banks. Figure reproduced from ref. [105].

The MuSR instrument is located at the pulsed muon source at ISIS [105]. A schematic of the instrument is shown in figure 2.8 and a photograph in figure 2.9. ISIS is currently the world's most intense source of pulsed muons. They are produced by the collision of 800 MeV protons on a thin graphite target. The muons produced are 100% spin-polarised and this polarisation is maintained through to implantation into the sample. The MuSR instrument uses positive muons with an incident energy of 26.5 MeV/c and an intensity of $4 \times 10^5 \mu^+/s$. The beam size has an adjustable 7-15 mm FWHM. It has 64 scintillator detector segments in two circular arrays of 32 detectors for forward and backward scattering. MuSR can be used for zero field, longitudinal field and transverse field investigations in fields of 0 - 0.2 T.

Chapter 3

Neutron scattering investigations of Ba_2RSbO_6 (R = Ho, Er)

As discussed in section 1.3 the rare earth double perovskites are candidates for a new three dimensional model geometric frustrated system. Neutron scattering investigations of Ba_2HoSbO_6 and Ba_2ErSbO_6 under various temperatures have been performed to investigate their magnetic properties.

3.1 Powder sample synthesis of Ba_2HoSbO_6 and Ba_2ErSbO_6

The powder samples of Ba_2HoSbO_6 and Ba_2ErSbO_6 were prepared by G. C. Lau and R. J. Cava et al. at Princeton University [26]. The starting materials were $BaCO_3$, Sb_2O_5 and Ho_2O_3 or Er_2O_3 for each variant. Stoichiometric mixtures of these powders were mixed in an agate mortar and heated in air in dense, high-purity Al_2O_3 crucibles. The samples were heated at 1400 °C for a total of 48 hours with several intermediate grindings. Approximately 11 grams of Ba_2HoSbO_6 and 15 grams of Ba_2ErSbO_6 were produced.

3.2 Neutron powder diffraction on GEM down to 1.5 K

Neutron diffraction measurements were performed at the ISIS pulsed neutron source using the high intensity and high resolution diffractometer GEM. This instrument is detailed in section 2.2.2. The zero field results were used to confirm the low temperature structures of Ba_2HoSbO_6 and Ba_2ErSbO_6.

The temperatures chosen to carry out the neutron diffraction were 20 K, which lies well within the paramagnetic regime, and 1.5 K, the lowest temperature accessible with the experimental arrangement. If the nuclear structure remains unchanged then any change in scattering between 20 K and 1.5 K can be attributed to the development of magnetic correlations.

3.2.1 Diffraction results at 20 K for Ba_2HoSbO_6 and Ba_2ErSbO_6

To verify the crystal structure of the powder samples the diffraction profile obtained at 20 K was refined using the GSAS rietveld refinement programme and the separately developed graphical user interface EXPGUI [106, 107]. This method produces an expected diffraction pattern from various instrumental and structural parameters entered by the user and compares it with the experimentally obtained results. The parameters can be allowed to be refined by the programme and in this way the predicted diffraction pattern and the experimentally obtained diffraction pattern can be compared by both a χ^2 statistic, with generally the lower the value the better the model, and by visually observing the difference of the calculated and experimental diffraction patterns.

Initial parameters for the crystal structure and position of the atoms were chosen from the literature for Ba_2HoSbO_6 [26] and Ba_2ErSbO_6 [44].

Results for Ba_2ErSbO_6 at 20 K

The results of the GSAS refinement of the diffraction data obtained at 20 K for Ba_2ErSbO_6 are shown in figure 3.1 and table 3.1. The good agreement of results used show that the structure for Ba_2ErSbO_6 is cubic with the space group $Fm\overline{3}m$. There are, however, some Bragg peaks which are unindexed by the structural model used in GSAS and the χ^2 value is relatively high. This will be considered further when discussing the 1.5 K data.

	Fractional coordinates	Thermal parameter (U_{iso} [Å^2])
Ba	0.25 0.25 0.25	0.002(1)
Er	0 0 0	0.0009(6)
Sb	0.5 0.5 0.5	0.001(1)
O	0.263(2) 0 0	0.003(7)
	$a(= b = c)$	8.39042(6) Å
	space group	$Fm\overline{3}m$
	χ^2	7.95(2)

Table 3.1: Parameters from GSAS refinement at 20 K for Ba_2ErSbO_6.

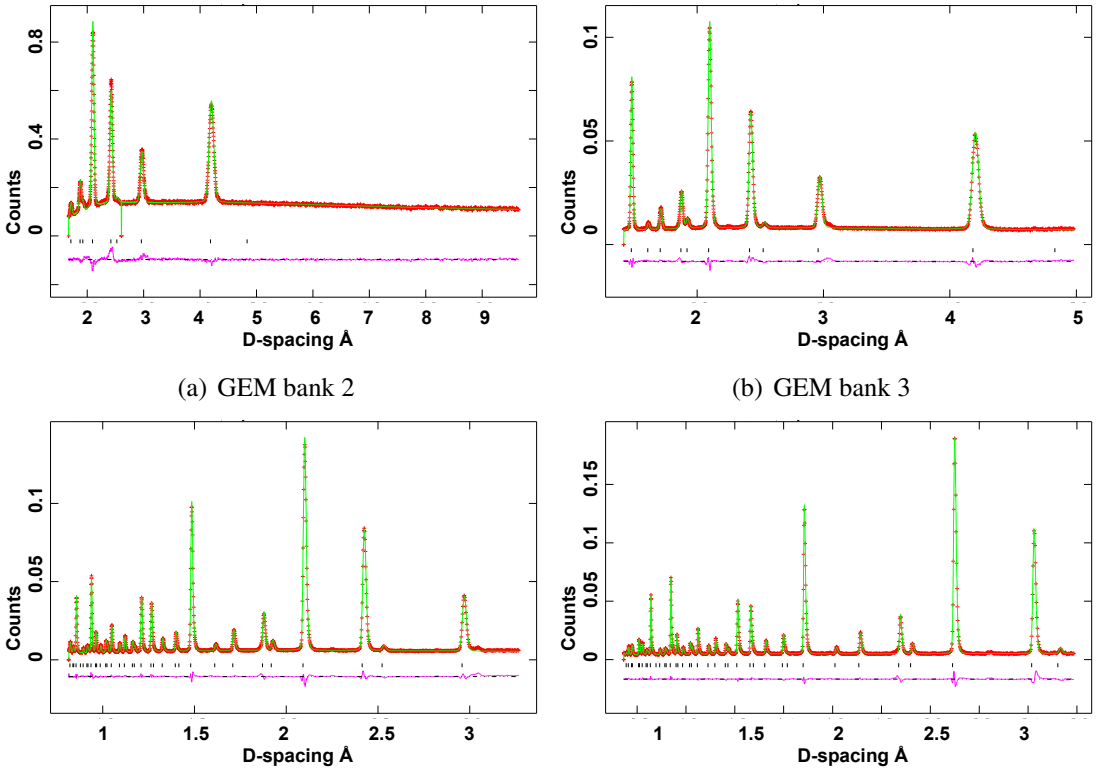

(a) GEM bank 2

(b) GEM bank 3

(c) GEM bank 4

(d) GEM bank 5

Figure 3.1: [Ba_2ErSbO_6] GSAS refinement of GEM powder diffraction of Ba_2ErSbO_6 at 20 K. The red crosses are the experimental data and the solid green line is the calculated diffraction using the parameters in table 3.1. The black vertical ticks are the calculated reflection points. The solid purple line is the difference between the calculated and experimental results. The banks refer to the various detector banks on the GEM instrument which cover different scattering angles.

Results for Ba_2HoSbO_6 at 20 K

The powder diffraction results for Ba_2HoSbO_6 and the corresponding fits are shown in figure 3.2. The fits were obtained using the parameters in table 3.2. Good agreement is obtained in the fits showing that Ba_2HoSbO_6 remains in the cubic space group $Fm\bar{3}m$ at 20 K. Notice the much improved χ^2 compared with the Ba_2ErSbO_6 results.

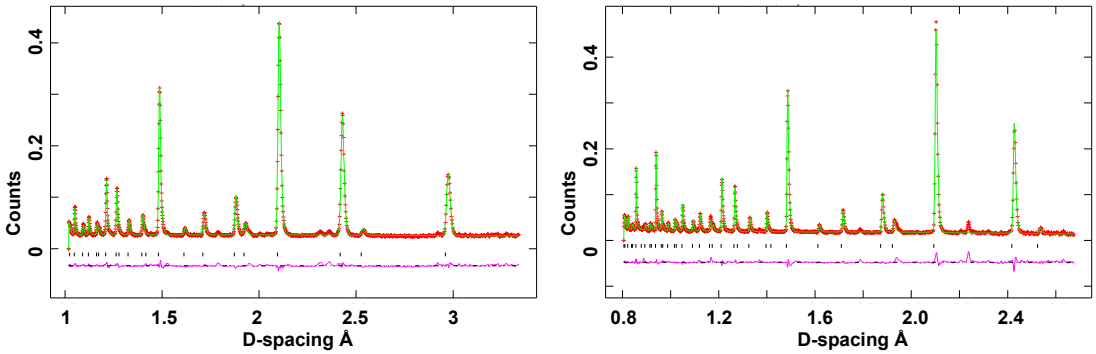

(a) GEM bank 4 (b) GEM bank 5

Figure 3.2: [Ba_2HoSbO_6] GSAS refinement of GEM powder diffraction of Ba_2HoSbO_6 at 20 K. The red crosses are the experimental data and the solid green line is the calculated diffraction using the parameters in table 3.2. The black vertical ticks are the calculated reflection points. The solid purple line is the difference between the calculated and experimental results. The banks refer to the various detector banks on the GEM instrument which cover different scattering angles.

	Fractional coordinates	Thermal parameter (U_{iso} [Å^2])
Ba	0.25 0.25 0.25	0.001(2)
Ho	0 0 0	0.001(4)
Sb	0.5 0.5 0.5	0.001(2)
O	0.264(3) 0 0	0.004(1)
	$a(=b=c)$	8.4017(7) Å
	space group	$Fm\bar{3}m$
	χ^2	4.778

Table 3.2: Parameters from GSAS refinement at 20 K for Ba_2HoSbO_6.

3.2.2 Comparison of results at 20 K and 1.5 K for Ba_2HoSbO_6

The diffraction results for Ba_2HoSbO_6 at 20 K and 1.5 K are compared in figure 3.3[1]. There is no observable difference suggesting that Ba_2HoSbO_6 does not undergo magnetic ordering between room temperature and 1.5 K, which agrees with the susceptibility results from the literature [26].

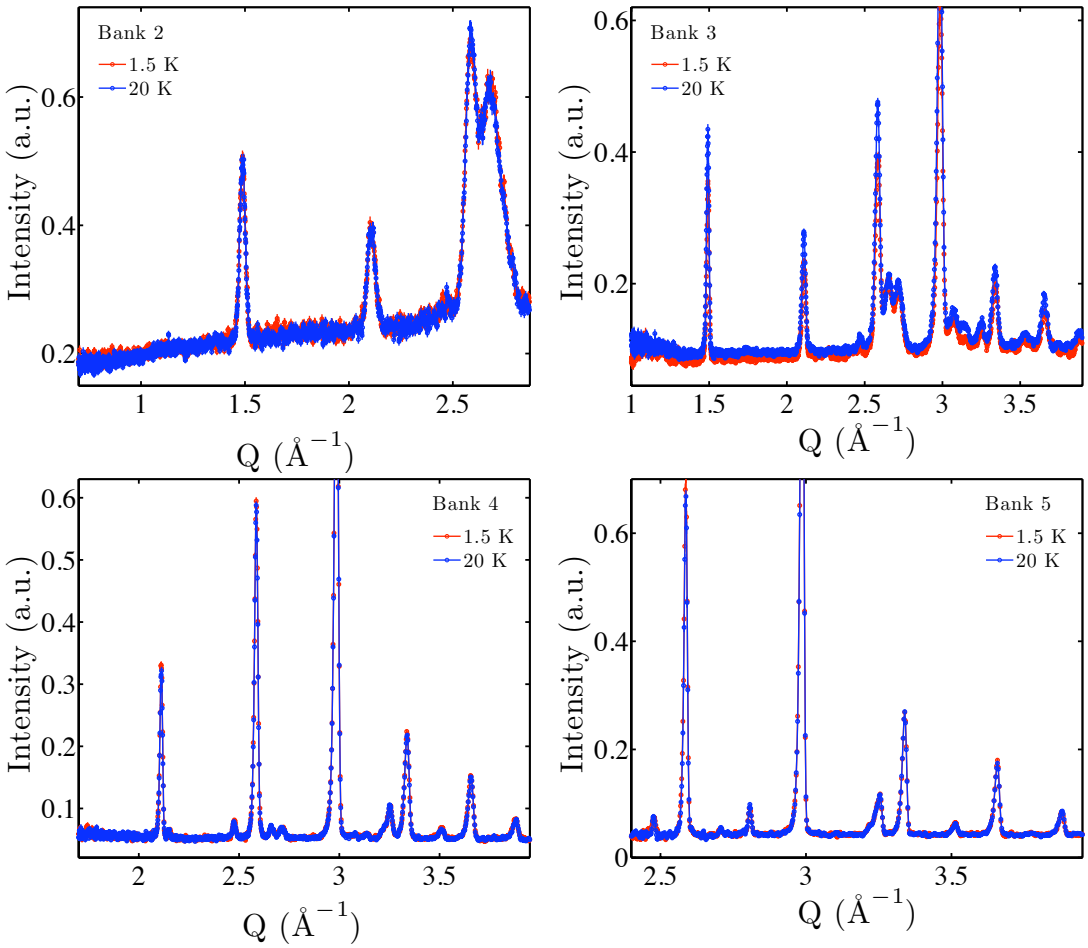

Figure 3.3: [Ba_2HoSbO_6] Comparison of neutron diffraction of Ba_2HoSbO_6 in the different detector banks of GEM at 20 and 1.5 K. There is no difference in scattering at the two temperatures indicating no change in structure or development of magnetic correlations.

[1] a.u. and arb. units denote arbitrary units throughout this thesis

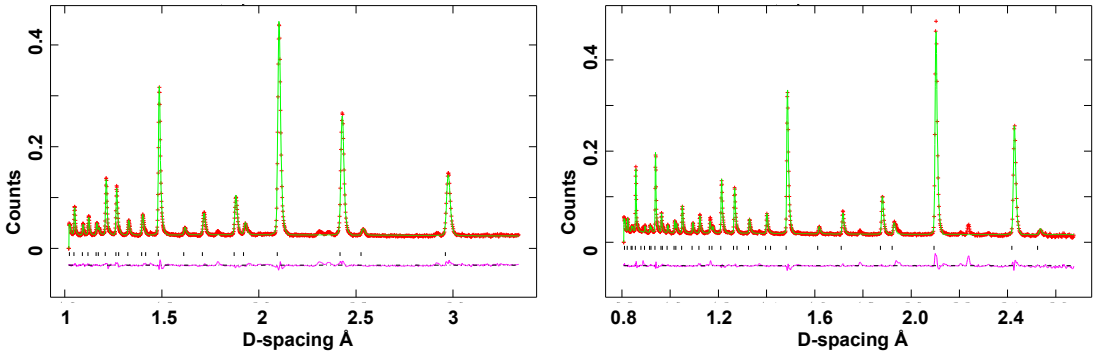

(a) GEM bank 4 (b) GEM bank 5

Figure 3.4: [Ba_2HoSbO_6] GSAS refinement results for Ba_2HoSbO_6 at 1.5 K. The red crosses are the experimental data and the solid green line is the calculated diffraction using the parameters in table 3.3. The black vertical ticks are the calculated reflection points. The solid purple line is the difference between the calculated and experimental results.

	Fractional coordinates	Thermal parameter (U_{iso} [Å^2])
Ba	0.25 0.25 0.25	0.001(5)
Ho	0 0 0	0.001(3)
Sb	0.5 0.5 0.5	0.001(1)
O	0.264(2) 0 0	0.004(4)
	$a(=b=c)$	8.4017(4) Å
	space group	$Fm\bar{3}m$
	χ^2	4.997

Table 3.3: Parameters from GSAS refinement for 1.5 K for Ba_2HoSbO_6.

The results of the GSAS refinement for Ba_2HoSbO_6 are shown in figure 3.4 for 1.5 K using the parameters in table 3.3. Due to the similarity in scattering at 20 and 1.5 K these results closely match those of the refinement carried out at 20 K and also are in good agreement with the refinement carried out at ambient temperature reported in the literature [26]. It is therefore shown that the crystal structure of Ba_2HoSbO_6 does not change between room temperature and 1.5 K. There are, however, some unindexed peaks that occur at 1.5 and 20 K. Various impurity phases were considered within GSAS and as a result, the following can be ruled out: Aluminium, Sb_2O_5, $BaCO_3$, Ho_2O_3 and

$Ba(Sb_2O_6)$. The unindexed peaks are believed to be an artefact of the GEM instrument itself since experiments carried out at the same time on a different structure have similar peaks.

3.2.3 Comparison of results at 20 K and 1.5 K for Ba_2ErSbO_6

The comparison of the diffraction results for Ba_2ErSbO_6 shows new peaks developing between 20 K and 1.5 K, as can be seen in figure 3.5. This suggests that there is magnetic order occurring in the powder sample, although the small size of the peaks suggest the ordering is weak.

To verify the magnetic ordering temperature measurements were taken at 1.5, 2.0, 2.5, 3.0, 3.5 and 4.0 K to follow the development of the magnetic order, as shown in figure 3.6 for the peak around 0.84 Å^{-1}. The ordering is seen to occur around 3.5 K.

The first deduction from these results is that Ba_2ErSbO_6 undergoes a transition to magnetic order around 3.5 K. To confirm if this is the case the new peaks have to be matched to magnetic correlations of the Er^{3+} ion in Ba_2ErSbO_6. There is one Er^{3+} ion per unit cell and the Er^{3+} ions form a fcc lattice and as such obey the reflection rules for fcc symmetry, namely that peaks can occur for crystal planes with miller indices (h, k, l) which are either all odd or all even. Applying these selection rules does not give an expected peak at 0.84 Å^{-1} or any multiples of 0.84 Å^{-1}. Attempting to find a model for the peaks using GSAS and SARAh [108], which allows all possible magnetic structures to be searched for using a Monte Carlo simulation and applied to GSAS, also did not produce any reasonable results.

This could be due to the magnetic structure being incommensurate with the nuclear structure. As such the results were analysed using SARAh and Fullprof, which is a similar refinement programme to GSAS, but with the extra option of handling incom-

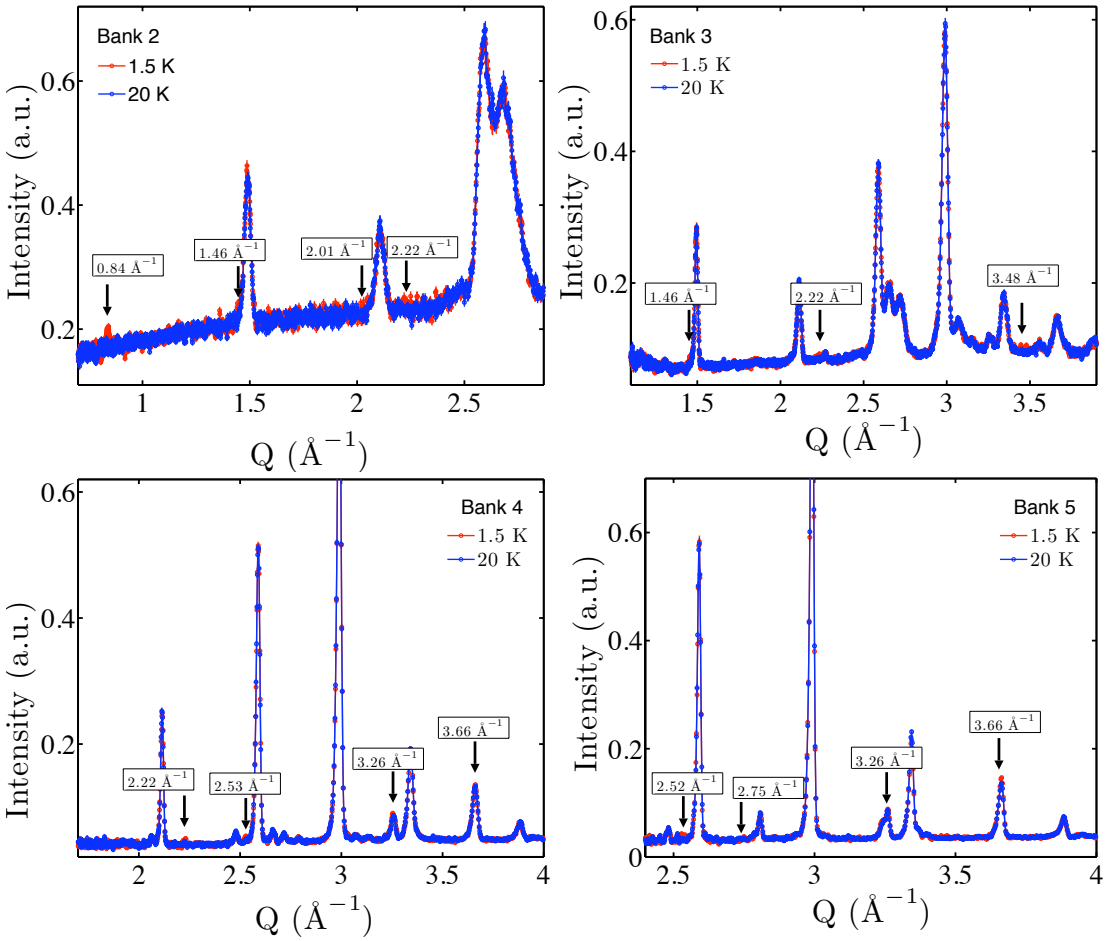

Figure 3.5: [Ba_2ErSbO_6] Comparison of diffraction results obtained on GEM at 20 and 1.5 K for Ba_2ErSbO_6. Additional peaks which appear at 1.5 K are highlighted and these are attributed the development of magnetic order.

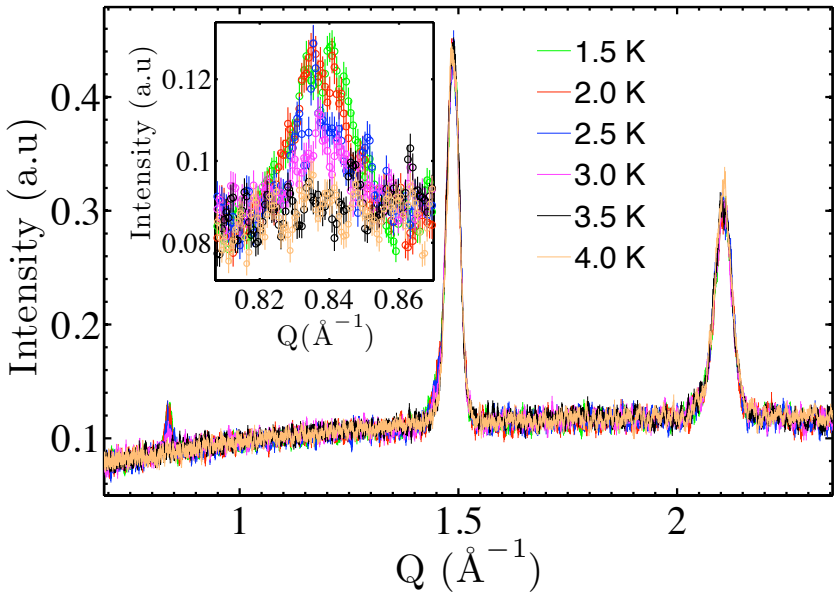

Figure 3.6: [Ba_2ErSbO_6] Development of magnetic order in the Ba_2ErSbO_6 powder sample. The inset shows the order develops between 3.0 and 3.5 K. This corresponds to the magnetic ordering temperature of Er_2O_3 of 3.4 K.

mensurate structures. Again no magnetic structures were found to match the extra peaks at 1.5 K using a single phase model of Ba_2ErSbO_6.

The next possibility considered was that there was an impurity in the sample and that this was responsible for the extra peaks observed at 1.5 K. The peak size being so much smaller than the nuclear peaks ($< 10\%$) also supports the idea that they are due to an impurity since the large magnetic moment of Er^{3+} would be expected to give peaks comparable, or larger, than nuclear peaks. The sample was prepared with starting materials $BaCO_3$, Er_2O_3 and Sb_2O_5. If these were not fully reacted then an impurity phase could remain. Since Er_2O_3 is the only starting compound which could undergo a magnetic transition it was investigated.

Results from the literature show that Er_2O_3 undergoes a magnetic transition at 3.4 K [109, 110], corresponding to the temperature at which the additional peaks appear in

the neutron diffraction results. The magnetic structure has been solved previously [109] and these results were used in GSAS in an attempt to index the magnetic peaks. The structural parameters used for Er_2O_3 are shown in table 3.4. These correspond closely to the starting structural parameters for Er_2O_3 used from the literature [109]. All the additional peaks can be indexed to the Er_2O_3 magnetic structure, as is shown in figure 3.7. This is best seen with the two highlighted peaks at d = 7.48 Å (Q = 0.84 $Å^{-1}$) and d = 4.28 Å (Q = 1.46 $Å^{-1}$) in the figure. Both these peaks appear around 3.5 K and can only both be indexed by magnetic reflections of Er_2O_3.

	Fractional coordinates	Thermal parameter (U_{iso} [$Å^2$])
Ba	0.25 0.25 0.25	0.002(1)
Er	0 0 0	0.0009(6)
Sb	0.5 0.5 0.5	0.001(1)
O	0.263(2) 0 0	0.003(7)
	$a(= b = c)$	8.3904(3) Å
	space group	$Fm\bar{3}m$
Er1	0.25 0.25 0.25	0.12(6)
Er2	0.979(2) 0 0.25	0.04(1)
O1	0.415(1) 0.131(1) 0.360(9)	0.02(2)
	$a(= b = c)$	10.52(1) Å
	space group	$Ia3$
	χ^2	8.669

Table 3.4: Parameters from GSAS refinement for 1.5 K for Ba_2ErSbO_6 and Er_2O_3. Note the high χ^2 is due to the magnetic component of Er_2O_3 not being fitted to the experimental results.

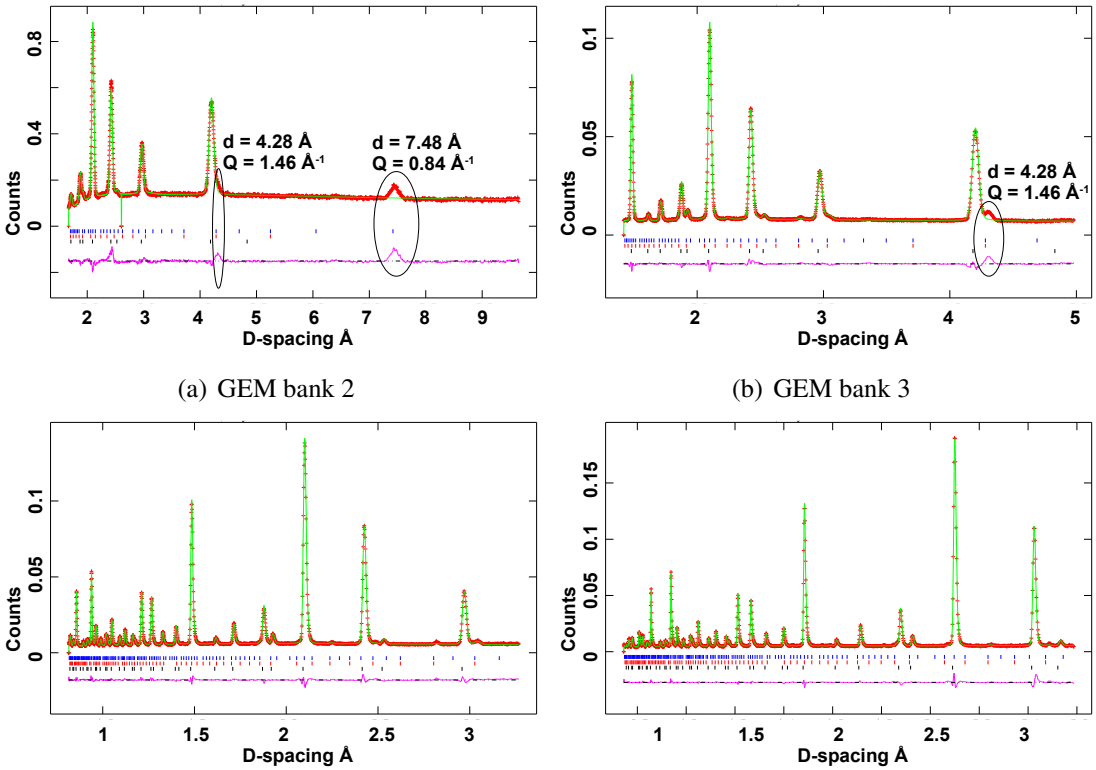

(a) GEM bank 2

(b) GEM bank 3

(c) GEM bank 4

(d) GEM bank 5

Figure 3.7: [Ba_2ErSbO_6] GSAS refinement of results for Ba_2ErSbO_6 at 1.5 K using an additional impurity phase of Er_2O_3. The three reflection ticks from top to bottom represent magnetic Er_2O_3, nuclear Er_2O_3 and nuclear Ba_2ErSbO_6 phases. The most obvious magnetic peaks are circled and shown to be only all indexed by a magnetic Er_2O_3 phase. The red crosses are the experimental data and the solid green line is the calculated diffraction using the parameters in table 3.4. The solid purple line is the difference between the calculated and experimental results.

Additionally adding this impurity phase to the refinement carried out at 20 K, where no magnetic order occurred, allowed the unindexed peaks to be fitted to the nuclear structure of Er_2O_3: see figure 3.8 and table 3.5. The χ^2 is also improved for the two phase 20 K refinement (decreasing from 7.952 to 5.834) showing the fits obtained are closer to the experimental data. As such the powder sample for Ba_2ErSbO_6 is found to contain one impurity phase of Er_2O_3 with no suggestion of any other impurities. These results confirm that along with Ba_2HoSbO_6, Ba_2ErSbO_6 does not order between ambient temperature and 1.5 K and the crystal lattice remains cubic with the point group of the magnetic ion remaining cubic.

	Fractional coordinates	Thermal parameter (U_{iso} [Å^2])
Ba	0.25 0.25 0.25	0.002(1)
Er	0 0 0	0.0009(6)
Sb	0.5 0.5 0.5	0.001(1)
O	0.263(2) 0 0	0.003(7)
	$a(=b=c)$	8.3904(3) Å
	space group	$Fm\bar{3}m$
Er1	0.25 0.25 0.25	0.01(1)
Er2	0.97(9) 0 0.25	0.04(1)
O1	0.41(5) 0.13(1) 0.36(1)	0.02(3)
	$a(=b=c)$	10.52(1) Å
	space group	$Ia3$
	χ^2	5.834

Table 3.5: Parameters from GSAS refinement for 20 K for Ba_2ErSbO_6 and Er_2O_3. The χ^2 is improved compared to the single phase case indicating an improved fit with the model used.

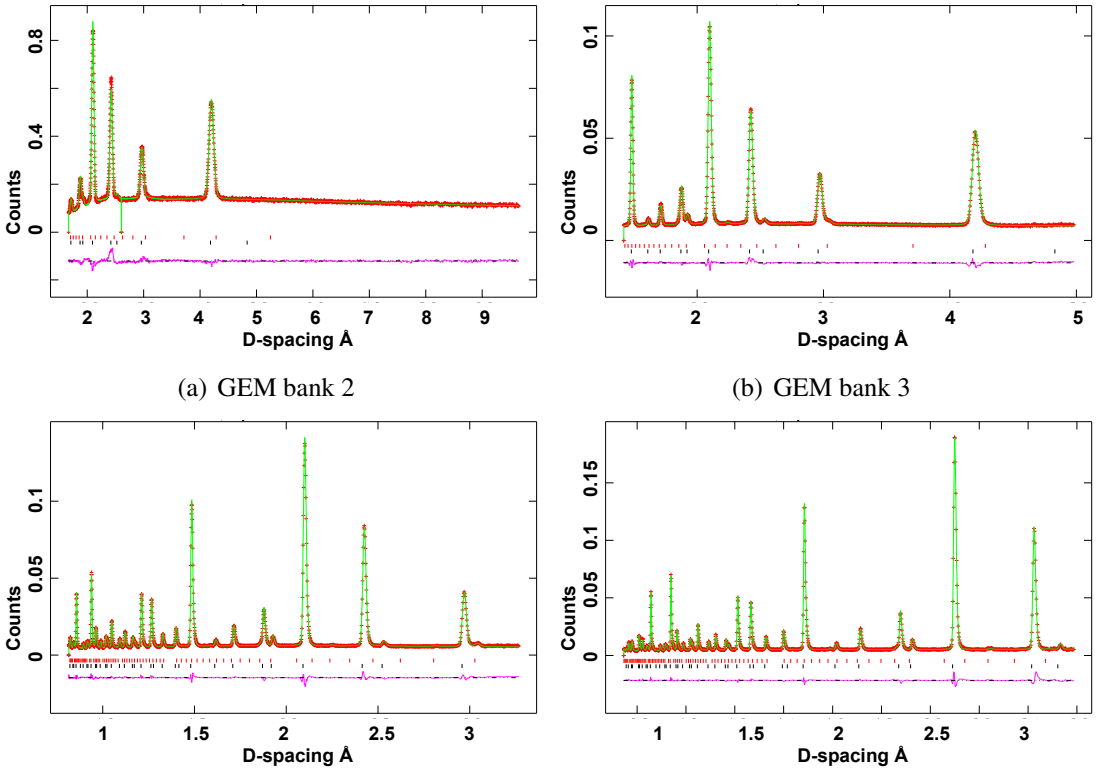

(a) GEM bank 2

(b) GEM bank 3

(c) GEM bank 4

(d) GEM bank 5

Figure 3.8: [Ba_2ErSbO_6] GSAS refinement of results for Ba_2ErSbO_6 at 20 K using an additional impurity phase of Er_2O_3. The two reflection ticks from top to bottom represent nuclear Er_2O_3 and nuclear Ba_2ErSbO_6 phases. The red crosses are the experimental data. The solid green line is the calculated diffraction using the parameters in table 3.5. The solid purple line is the difference between the calculated and experimental results. The unindexed peaks are now fitted to nuclear scattering of Er_2O_3.

3.3 Polarised neutron analysis of Ba_2RSbO_6 (R = Ho, Er)

In order to gain further information into any onset of magnetic order the temperature range of investigation was lowered to 60 mK. Since the magnetic correlations may be subtle due to frustration of the spin interactions xyz polarized neutron diffraction was carried out on D7 at the ILL, with the instruments operation being discussed in section 2.2.5.

3.3.1 Results from D7 for Ba_2HoSbO_6

Figure 3.9(a) compares the total scattering obtained at 5 K, 0.5 K and 60 mK on D7. There is no difference in the total scattering as the temperature is varied suggesting no magnetic correlations. However the power of the xyz polarised neutron analysis is that it allows the magnetic scattering to be separated out from the total scattering. The total scattering, separated nuclear component and magnetic component are shown in figure 3.9(b) for 60 mK. There is no evidence of magnetic order at 60 mK. The results from the nuclear scattering show the expected Bragg peaks for Ba_2HoSbO_6. The peaks around $\sim$1.5 Å^{-1} and $\sim$2.1 Å^{-1} are due to the coherent nuclear scattering. These peaks can be indexed for Ba_2HoSbO_6 at $(2, 0, 0)$ and $(2, 2, 0)$.

A comparison of the magnetic scattering between 5 K and 60 mK in figure 3.10 confirms the lack of magnetic ordering. The magnetic component shows no sharp or diffuse peaks which would be indicative of long or short range order down to 60 mK.

There is a clear drop off in magnetic intensity with increasing Q. Starting from empirical analytical formulas and using relevant coefficients [111] the magnetic form factor for Ho^{3+} was produced and a least squares analyses was used to fit this to the neutron results for the magnetic component. The magnetic results are found to follow

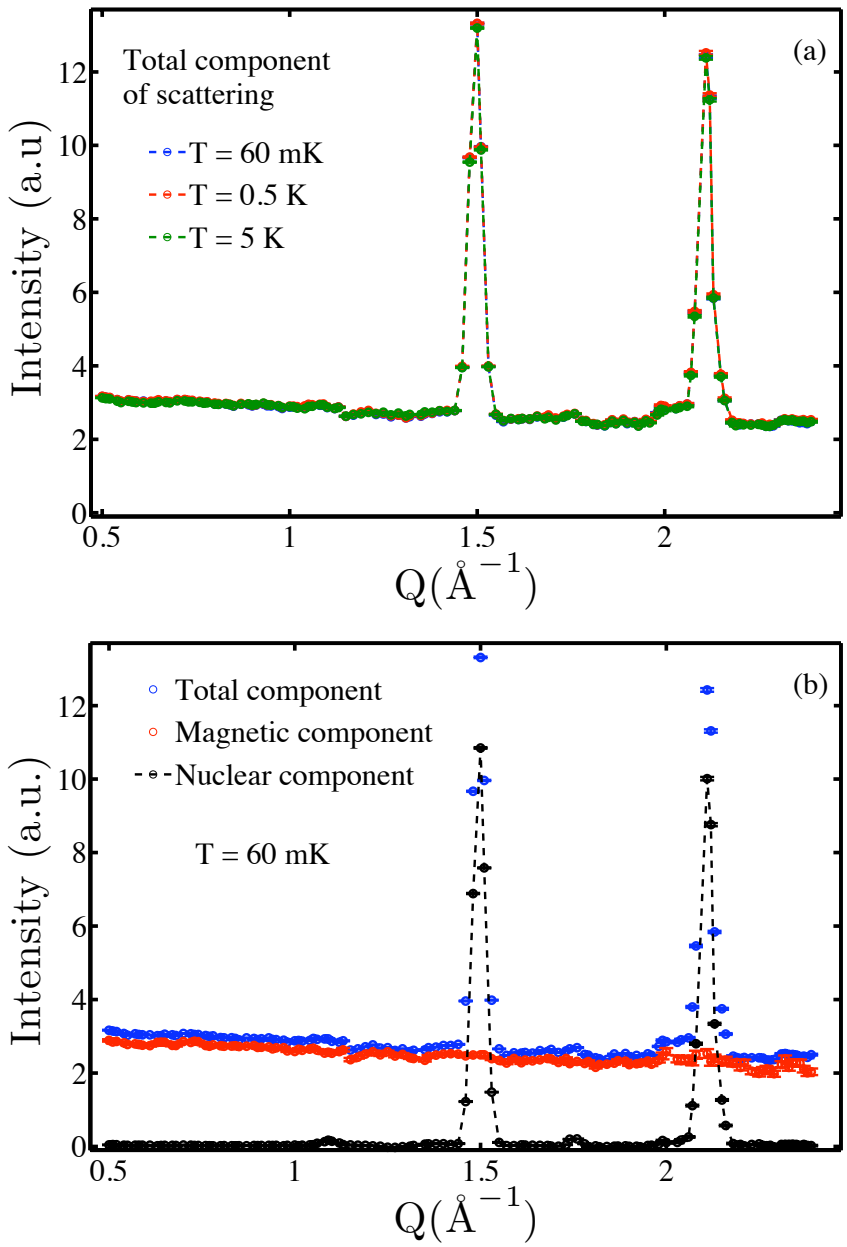

Figure 3.9: [Ba_2HoSbO_6] Polarised neutron analysis from D7. (a) Total component of scattering for Ba_2HoSbO_6 at 5 K, 0.5 K and 60 mK showing no change between temperatures. (b) The total scattering at 60 mK is shown along with the separated magnetic and nuclear components. No magnetic long or short range ordering is observed at 60 mK for Ba_2HoSbO_6.

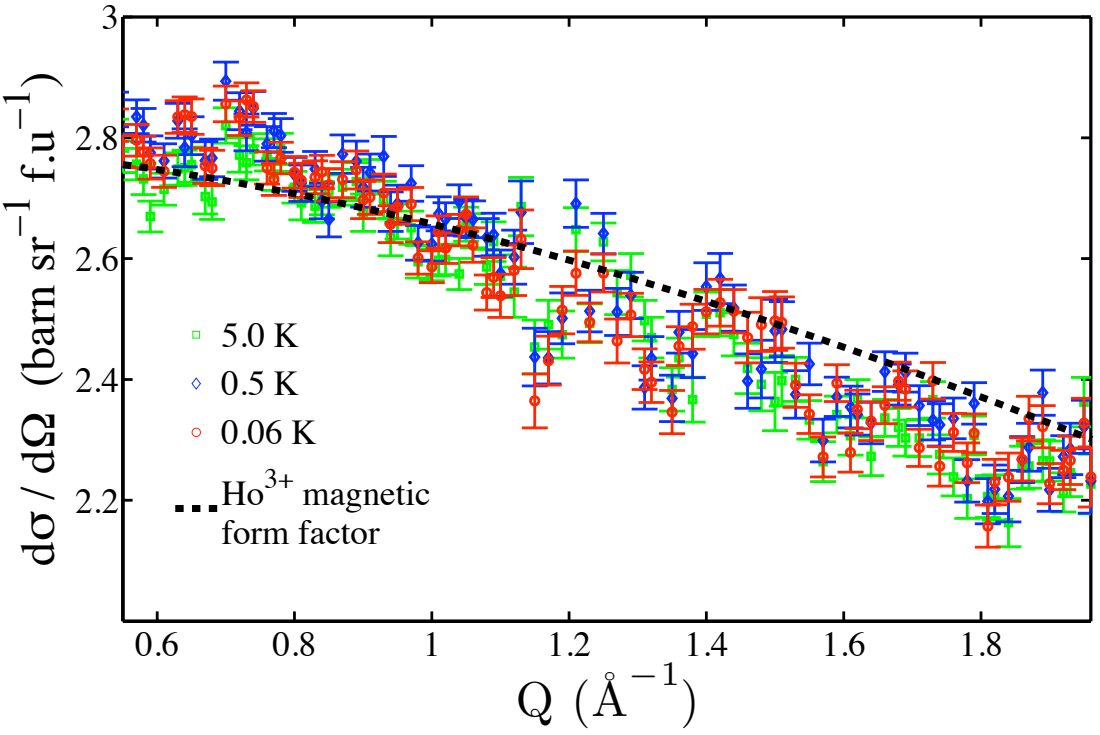

Figure 3.10: [Ba_2HoSbO_6] Magnetic component of Ba_2HoSbO_6 from the xyz polarized neutron diffractometer D7 at the ILL. No magnetic long or short range order is evident and the $|Q|$ dependent scattering fits the form factor for Ho^{3+} between 5 and 0.06 K.

the form factor of Ho^{3+} with no variation between 60 mK and 5 K. This would suggest that Ba_2HoSbO_6 remains in the paramagnetic regime in this temperature range. This is a surprising result given $\theta_W \approx -5$ K [26].

3.3.2 Results from D7 for Ba_2ErSbO_6

The total scattering observed on D7 for Ba_2ErSbO_6 is shown in figure 3.11(a). There is a large magnetic peak around 1.5 Å^{-1} and a peak at 0.84 Å^{-1}. These peaks can be understood with consideration of the separated nuclear and magnetic scattering shown in figure 3.11(b) and the knowledge gained of the impurity phase of Er_2O_3 found from the standard diffraction carried out on GEM. The peak at 0.84 Å^{-1} is due to purely magnetic scattering which develops between 4 K and 3 K. This peak matches that observed in the GEM experiment and is due to the impurity phase of Er_2O_3. Similarly the small peak observed in the magnetic scattering at 1.46 Å^{-1} is at the expected position, and orders at the expected temperature, for Er_2O_3. The large nuclear Bragg peak in the nuclear scattering component is due to Ba_2ErSbO_6. The slight antisymmetry of the peak in the total component and change in intensity with temperature in the total scattering in figure 3.11(a) is due to the overlap of the magnetic peak of Er_2O_3 and the nuclear peak of Ba_2ErSbO_6. From figure 3.11 there is no apparent diffuse scattering observed that could be due to magnetic correlations of Er^{3+} in Ba_2ErSbO_6.

A closer look at purely magnetic scattering is shown in figure 3.12. The two magnetic Bragg peaks at 0.84 Å^{-1} and 1.46 Å^{-1} are highlighted as being due to the impurity phase of Er_2O_3. The D7 results suggest a two stage temperature induced phase transition, however this was due to changing the sample environment from an orange cryostat to the dilution fridge without obtaining the correct background for deduction. Apart from the two peaks due to the magnetic order from Er_2O_3 the results look very similar to Ba_2HoSbO_6, i.e. there is no evidence of long or short range magnetic order. The magnetic scattering can be fitted to the form factor for Er^{3+}, as was done for Ba_2HoSbO_6. The close agreement to the magnetic form factor shows that the neutron is measuring magnetic moments, but they are not correlated.

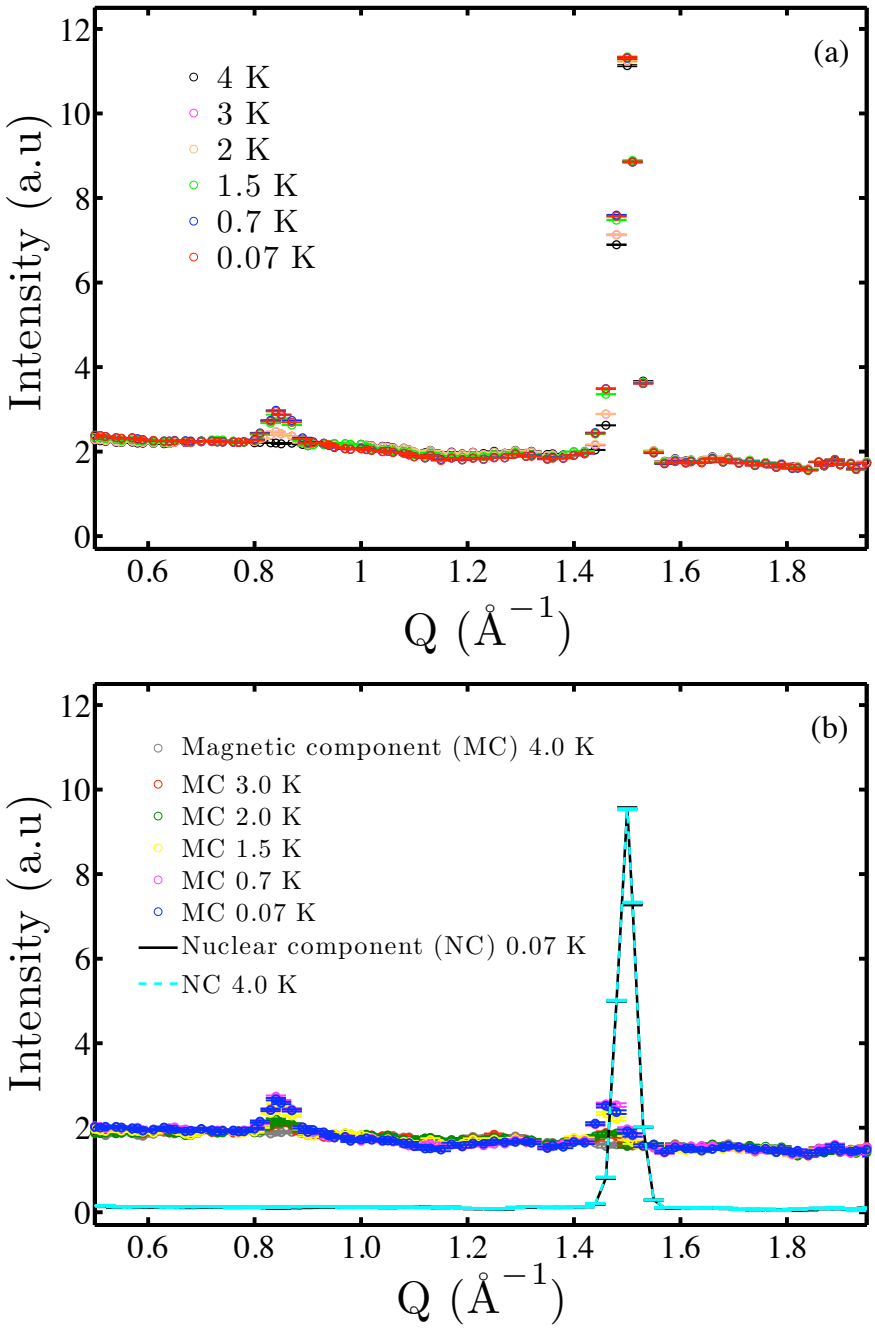

Figure 3.11: [Ba_2ErSbO_6] (a) Total component of the nuclear scattering for Ba_2ErSbO_6. (b) The nuclear and magnetic scattering is separated from the total scattering. It can be seen that the nuclear and magnetic peaks are not centred at the same position. The magnetic peaks have been found to be due to an impurity phase of Er_2O_3.

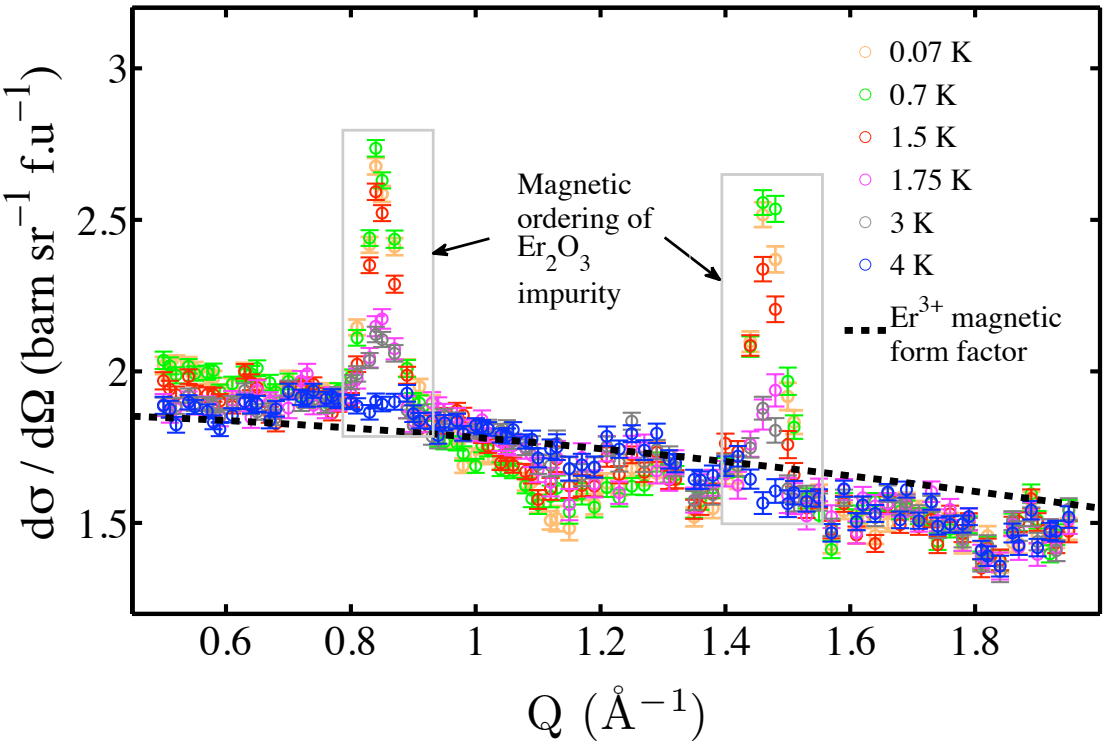

Figure 3.12: [Ba_2ErSbO_6] Magnetic component of Ba_2ErSbO_6 from the xyz polarized neutron diffractometer D7 at the ILL. No magnetic long or short range order is evident and the $|Q|$ dependent scattering fits the form factor for Er^{3+} between 4 and 0.07 K. The observed magnetic peaks are due to an impurity phase of Er_2O_3.

These results show unambiguously that there is no magnetic short or long range order for Ba_2HoSbO_6 and Ba_2ErSbO_6 down to 60 mK. They also confirm there is no structural change from cubic which will be useful in the following consideration.

3.4 Crystal field analysis of Ba_2RSbO_6 (R = Ho, Er)

In this section crystal field theory is reviewed and discussed in the context of the rare earth double perovskites. A crystalline electric field (CEF) analysis was carried out on Ba_2HoSbO_6 and Ba_2ErSbO_6 at ISIS using the MARI spectrometer. In the setting of frustration obtaining crystal field parameters and finding the associated crystal field level scheme has proven to be extremely useful in explaining observed properties and ground states adopted. One pertinent example is the crystal field analysis carried out on the rare earth pyrochlore $Ho_2Ti_2O_7$ [25], discussed in section 1.2.

3.4.1 Crystalline electric field theory

Crystalline electric field theory was first introduced by Bethe [112] and has proved extremely valuable in explaining and predicting behaviour in condensed matter systems, particularly where a rare earth ion is present. A review by Hutchings [113] goes through the derivation of the crystalline electric field and highlights the use of different notation in crystal field research. This is a common, although not insurmountable, hindrance to the understanding and use of CEF values obtained in the literature. Hutchings sets out to rectify this and it is the notation used in his review that will be employed in the discussions here.

Crystal field theory describes the effect of the surrounding electric field from the crystal on a particular ion. It does not take into account interactions between magnetic ions, treating them as uncoupled single ions. When considering a magnetic ion which is positively charged it is generally assumed to be surrounded by negative ions, such as oxygen, with the surrounding charges causing a splitting of the free ion quantum states. A point charge model is used where the crystal field effects is treated as a perturbation on the free ion wavefunctions and energy levels. The Hamiltonian for the crystal field

can be written as:

$$\mathscr{H}_{\mathrm{CEF}} = -|e| \sum_i V_{\mathrm{CEF}}(r_i). \tag{3.1}$$

In the case of the rare earth ions it is the $4f$ electrons which experience the CEF and hence the i sums over this shell. $\mathscr{H}_{\mathrm{CEF}}$ can be interpreted using the simple point charge model to set up the potential $V_{\mathrm{CEF}}(r_i)$ felt by the ion due to the neighbouring charges in the lattice. The resultant electrostatic potential is given by:

$$V(x,y,z) = \sum_{n\alpha} r^n \gamma_{n\alpha} Z_{n\alpha}(x,y,z) \tag{3.2}$$

where the coefficients $\gamma_{n\alpha}$ are related to the charge distribution $\rho(r)$ through the following relationship:

$$\gamma_{n\alpha} = \frac{4\pi}{2n+1} \int \mathrm{d}^3 r \frac{\rho(r)}{r^{n+1}} Z_{n\alpha}(x,y,z) \tag{3.3}$$

$Z_{n\alpha}(x,y,z)$ are the tesseral harmonics expressed in Cartesian coordinates and tabulated in Hutchings' review [113]. Stevens' "operator equivalents" method can be used, in which the rules are laid out [114]. For rare earth ions the spin-orbit energy is much larger than the CEF energy and hence it is generally sufficient to just consider the lowest J multiplet of the $4f$ shell. The "operator equivalent" method uses the fact that within a manifold of states for which J is constant there are simple relations between the matrix elements of potential operators and appropriate angular momentum operators. For example consider a Cartesian function $f(x,y,z)$ in the crystal field Hamiltonian function shown in equation 3.1. The operator equivalent is found by simply replacing x, y, and z in the function $\sum_i f(x,y,z)$ with J_x, J_y and J_z, taking into account non-commutation. The resultant operator has the same transformation properties under rotation as the potential. The operators act on the $4f$ shell as a whole as opposed to x, y, and z in $f(x,y,z)$ which acts on each individual single electron wave function in the $4f$ shell.

Some examples of the method are shown here:

$$\sum_i (x_i^2 - y_i^2) \equiv \alpha\langle r^2\rangle[J_x^2 - J_y^2] = \alpha\langle r^2\rangle O_2^0 \tag{3.4}$$

$$\sum_i (3z_i^2 - r_i^2) \equiv \alpha\langle r^2\rangle[3J_z^2 - J(J+1)] = \alpha\langle r^2\rangle O_2^2 \tag{3.5}$$

$\alpha\langle r^n\rangle$ are included as constants of proportionality which depend on the degree n of the polynomial and on L, S and J. Hutchings includes complete tables of O_n^m.

The operator equivalent Hamiltonian is generally written in one of the following forms:

$$\mathscr{H}_{\mathrm{CEF}} = \sum_{nm} B_n^m O_n^m \tag{3.6}$$

or,

$$\mathscr{H}_{\mathrm{CEF}} = \sum_{nm} A_n^m \langle r^n\rangle \theta_l O_n^m \tag{3.7}$$

where O_n^m are Stevens operators tabulated by Hutchings [113]. B_n^m (or A_n^m) are the CEF parameters which can be obtained experimentally to predict the effect of the crystal field on the free ion states. The values can also be predicted by the use of, for example, the point charge model, but this is of limited value.

The symmetry of the lattice under investigation determines the form of $\mathscr{H}_{\mathrm{CEF}}$ through non-zero O_n^m operators. The magnetic ions Ho^{3+} and Er^{3+} in Ba_2HoSbO_6 and Ba_2ErSbO_6 have the cubic point group symmetry of $m\bar{3}m$. The treatment of $\mathscr{H}_{\mathrm{CEF}}$ in a cubic potential is fully treated in Hutchings using the operator equivalent method and is given by:

$$\mathscr{H}_{\mathrm{CEF}} = B_4^0[O_4^0 + 5O_4^4] + B_6^0[O_6^0 - 21O_6^4]. \tag{3.8}$$

Hence for cubic symmetry there are two CEF parameters B_4^0 and B_6^0 to determine.

3.4.2 Simplification of CEF theory for cubic point symmetry

A convenient step, which allows for much easier analysis of experimental data, in finding values for the crystal field parameters for ions with cubic point group symmetry is to employ results obtained by Lea, Leask and Wolf (LLW) [115]. They tabulated normalized eigenvectors and eigenvalues for all integer and half integer J values between 2 and 8 using all possible values of the ratio between the two crystal field parameters B_4^0 and B_6^0. In this way the problem of finding values for the crystal field parameters in cubic symmetry was reduced to a one-dimensional problem.

They achieve this by rewriting equation (3.8) in the following form:

$$\mathscr{H}_{\mathrm{CEF}} = B_4^0 F(4)\frac{O_4^0 + 5O_4^4}{F(4)} + B_6^0 F(6)\frac{O_6^0 - 21O_6^4}{F(6)} \tag{3.9}$$

where $F(4)$ and $F(6)$ are constant factors for a particular J. To cover all the possible values of the ratio between B_4 and B_6 LLW set:

$$B_4^0 F(4) = Wx \tag{3.10}$$

$$B_6^0 F(6) = W(1 - |x|) \tag{3.11}$$

where $-1 \leq x \leq 1$ and W is introduced in these equations as an energy scale factor between $-\infty \leq W \leq \infty$ for the crystal field energy levels. LLW scanned through x from -1 to 1 and produced tables of the eigenvectors. Diagrams of the eigenstates are shown in figure 3.13, these show the CEF energy levels for the x values in the allowed range of $-1 \leq x \leq 1$. The CEF parameters can then be found by scanning for possible x values which match the pattern of the peaks from neutron spectroscopy, and then applying an appropriate scaling value W. It can be predicted whether x and W are positive or negative, thus giving a starting point for the likely energy level scheme. The sign of W is determined by the sign of B_6^0 and the sign of x is determined by the sign of $\frac{B_4^0}{B_6^0}$. For a particular local coordination and J value the sign is tabulated in LLW [115].

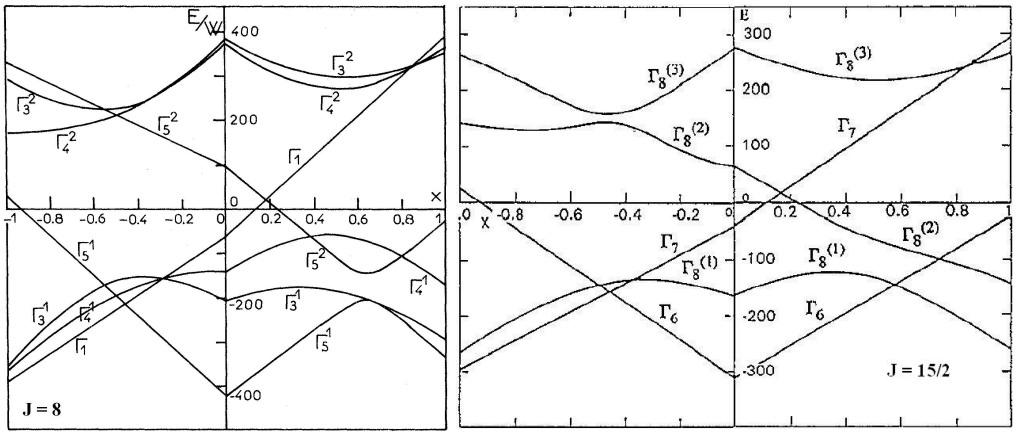

Figure 3.13: [Figure reproduced from ref. [115]] The possible eigenvalues found by LLW for the range of x and W values for $J = 8$ which corresponds to Ho^{3+} and for J = 15/2 which corresponds to Er^{3+}. These plots can be used to fit intensity peaks from neutron inelastic scattering experiments to predict crystal field parameters and the resultant energy levels.

The LLW method has been used successfully many times to predict structures in various cubic systems, see for example [116–119]. A similar analysis was carried out by Walter et al. to find crystal field parameters in lower than cubic symmetry [120]. Indeed this was employed by Rosenkranz et al. to find the crystal field parameters and resultant structure of $Ho_2Ti_2O_7$ [25].

There are, however, some limitations in the application of crystal field theory. Namely uncertainty in the free ion wavefunctions and possible admixtures of different J-manifolds by the crystal field. Although the calculations cannot be considered to be exact, at the very least they can be taken as a good first approximation.

3.5 Determining the crystal field level scheme by neutron scattering

3.5.1 Inelastic neutron scattering results and crystal field analysis

Time of flight (TOF) neutron inelastic scattering (INS) was carried out on polycrystalline samples of the rare earth double perovskites Ba_2HoSbO_6 and Ba_2ErSbO_6. The process involves scattering neutrons from the sample and measuring the transfer in energy which occurs. A transfer in energy occurs when the neutron induces excitations between the different allowed crystal field energy levels resulting in intensity in the scattering observed in $S(\mathbf{Q}, \omega)$. Various scattering angles are used and the intensity and energy transfer are measured to produce maps as shown in figure 3.14. These transitions show up as peaks in intensity versus energy plots.

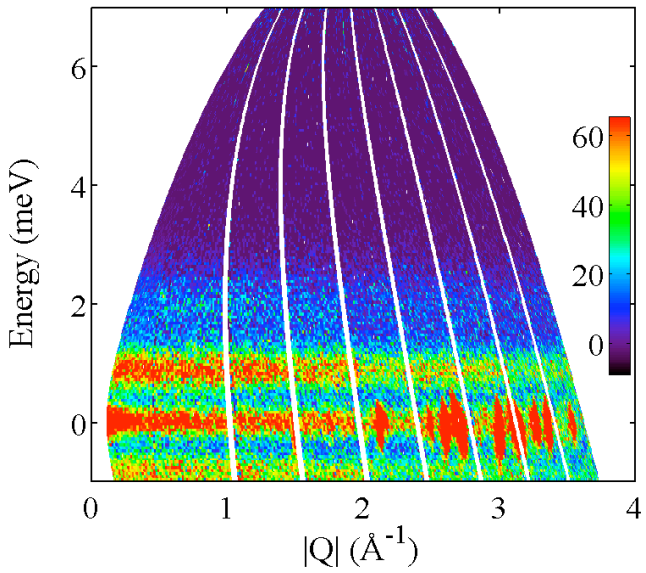

Figure 3.14: [Ba_2HoSbO_6] Inelastic neutron scattering obtained from MARI for Ba_2HoSbO_6 for an energy of 8 meV at 50 K. The inelastic scattering can be seen around 1 meV. The quantitative analysis relies on taking cuts along constant Q and E.

3.5.2 Theory and rules for obtaining crystal field levels from inelastic neutron scattering results

The scattering cross section $\frac{\mathrm{d}^2\sigma}{\mathrm{d}\Omega dE}$ for a transition from the initial state $|i\rangle$ to the final state $|f\rangle$ in a single J multiplet containing N non-interacting magnetic ions is given by [89, 92]:

$$\frac{\mathrm{d}^2\sigma}{\mathrm{d}\Omega dE} = N\left(\frac{1.91e^2 g_j}{2mc^2}\right)^2 F^2(\mathbf{Q}) \times \frac{k_f}{k_i}\sum_{i,f} P_i \left|\langle i|\mathbf{J}_\perp|f\rangle\right|^2 \delta(E_i - E_f - E) \quad (3.12)$$

This equation is valid for small $\mathbf{Q}$ and for unpolarized neutrons. It is this scattering cross section that is measured in a neutron scattering experiment. There are some key points that can be obtained from this equation. The energy of the CEF levels does not depend on the value of $\hbar Q$ (the momentum transferred from the neutron to the sample) since the measurement is of a single ion cross-section. The intensity does however depend on the magnetic form factor, $F^2(Q)$. The scattering intensity between two energy levels is given by the ratio of $P_i \left|\langle i|\mathbf{J}_\perp|f\rangle\right|^2$, where P_i is the occupational probability described by Boltzmann statistics. The transition matrix element is obtained by diagonalizing the Hamiltonian. Birgeneau listed these transition probabilities for the f-electron J-multiplets in cubic crystal field environments [121].

By taking intensity cuts at constant Q through energy or constant energy through Q the results of the INS can be analysed. Qualitative information can be obtained from these plots by considering the following rules regarding CEF excitations [25, 117, 119]:

1. The inelastic peak intensity decreases for ground state transitions as the temperature is increased.

2. For transitions between the excited states the inelastic peaks increase in intensity with increasing temperature as they become more populated at higher temperatures.

3. Crystal field peaks are non-dispersive since they are single ion excitations, although a dispersion may arise as a result of exchange coupling.

4. For a single transition peak at constant temperature the intensity should decrease with increasing Q due to the magnetic form factor $F^2(Q)$.

This last point allows a distinction to be made between phonon and crystal field scattering since phonon scattering increases as $|Q|^2$.

It should also be noted that the occurrence of a peak in an INS experiment is due to its matrix element value between the two levels of a transition. Transitions which have zero matrix element will not be present in these plots.

3.5.3 Inelastic neutron scattering on the MARI spectrometer

The experiment was carried out at the ISIS pulsed neutron source using the MARI spectrometer instrument. This instrument is detailed in section 2.2.1. For Ba_2HoSbO_6 measurements were taken for incident energies of 8 meV and 60 meV at 5, 15, 25, 50, 75, 100, 200 and 300 K. Ba_2ErSbO_6 measurements were taken at 5, 50, 100 and 200 K for incident energies of 8, 35 and 75 meV.

Temperature variation of inelastic neutron scattering results

The rules for finding CEF levels can now be applied to the results obtained from INS on MARI. Constant Q cuts are shown in figure 3.15 for Ba_2HoSbO_6. The variation of the peaks with intensity can be used to assign whether the peaks are due to CEF level transitions and whether it is for transitions between the ground state to the excited state or between excited states. In this way possible CEF levels and energy gaps can be postulated and then the LLW figures used to help in obtaining the true CEF level scheme.

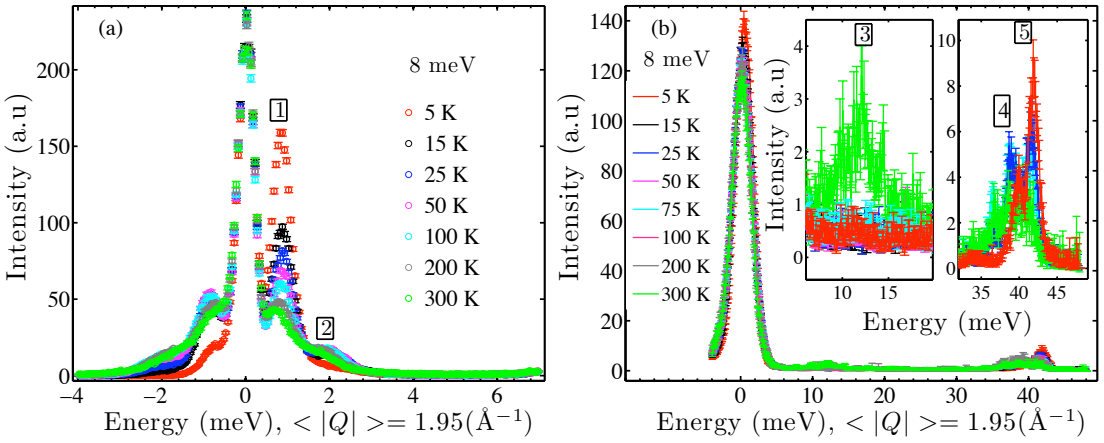

Figure 3.15: [Ba_2HoSbO_6] Intensity variation with energy at constant Q for inelastic neutron scattering results obtained on MARI at the ISIS pulsed neutron facility. (a) Initial neutron energy of 8 meV. Two peaks are observed, labelled 1 and 2. (b) Increasing the incoming energy to 60 meV allows additional peaks to be identified, labelled 3,4 and 5.

There are two peaks numbered in figure 3.15(a). Peak 1 is centred around ∼0.9 meV and can be seen to decrease with increasing temperature and is therefore due to a transition between the GS and an excited level. Peak 2 behaves differently, increasing with increasing temperature. This suggests it is due to excited energy levels separated by ∼2 meV. This could either mean that there is an energy level 2 meV above level 1 at ∼3 meV, or it is due to transitions between higher energy levels.

Figure 3.15(b) shows the results obtained for 60 meV. The large elastic peak obscures peaks 1 and 2. Peak 3 occurs around ∼12 meV and increases with increasing temperature and is therefore due to transitions between excited levels separated by 12 meV. Peaks 4 and 5 occur around 40 meV and decrease with increasing temperature so are assigned as GS to excited levels. There is a suggestion of a peak around 38 meV which can be attributed to transitions between excited levels.

The outcome of inspecting the INS results as they vary with temperature is shown in table 3.6. This analysis of the peaks was used to limit the possible areas in the LLW

Peak number	Aprrox. energy (meV)	Peak size with increasing temp.	Assignment of peak
1	0.9	Decrease	GS to excited
2	2.0	Increase	excited to excited
3	12	Increase	excited to excited
4	40	Decrease	GS to excited
5	42	Decrease	GS to excited

Table 3.6: Assignment of inelastic peaks due to their variation with temperature for Ba_2HoSbO_6.

Peak number	Aprrox. energy (meV)	Peak size with increasing temp.	Assignment of peak
i	3	Varies	unassigned
ii	5	Decrease	GS to excited
1	12	Decrease	GS to excited
2	15	Decrease	GS to excited
3	45	increase	excited to excited

Table 3.7: Assignment of inelastic peaks due to their variation with temperature for Ba_2ErSbO_6.

tables to be used as starting points for finding the CEF energy levels.

A similar analysis was carried out for Ba_2ErSbO_6, see figure 3.16. Figure 3.16(a) shows the results for an incoming energy of 8 meV and appears flat initially, but looking at it with a lower intensity scale shows some peaks at $\boxed{\text{i}}$ and $\boxed{\text{ii}}$. Peak $\boxed{\text{ii}}$ behaves as a CEF transition from GS to an excited level. But as with all peaks they have to be looked upon with caution, using the knowledge that there is an impurity phase of Er_2O_3 and noting the small size of the peak (the first GS to excited state transition peak should be large since it will be highly populated at 5 K). A literature search shows that there is a CEF level at $\sim$5 meV for Er_2O_3 [122–124]. This would mean that caution must be exercised if this peak is to be assigned to Ba_2ErSbO_6.

Figure 3.16(b) was obtained using an incident energy of 35 meV on MARI and has peaks $\boxed{1}$ and $\boxed{2}$ around $\sim$13 and 15 meV which both decrease with increasing

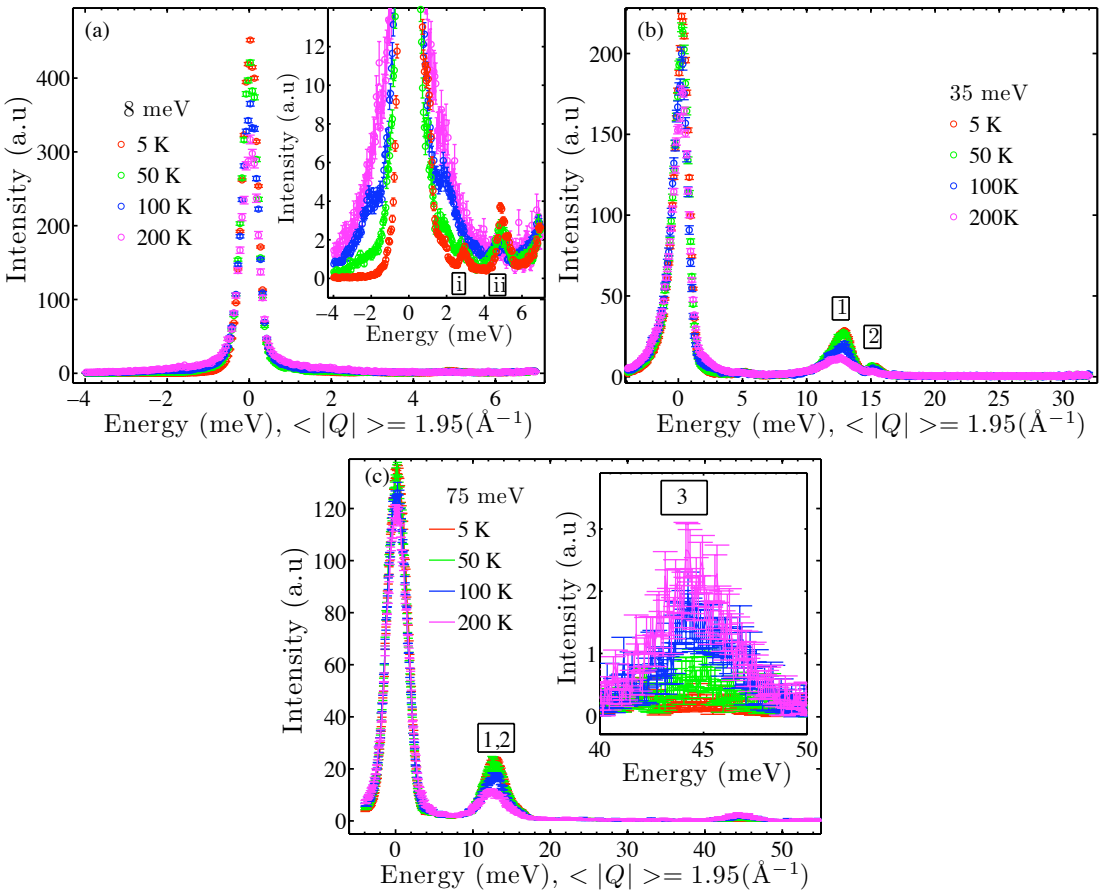

Figure 3.16: [Ba_2ErSbO_6] Intensity variation with energy at constant Q for inelastic neutron scattering results obtained on MARI at the ISIS pulsed neutron facility for Ba_2ErSbO_6. (a) Initial neutron energy of 8 meV. Two low intensity peaks are observed at 3 and 5 meV. (b) Results for incoming energy of 35 meV shows two further peaks 1 and 2. (c) Increasing the energy further to 75 meV reveals a broad peak centred around 45 meV.

temperature. These are attributed to GS to excited level transitions.

The results of incoming energy of 75 meV is shown in figure 3.16(c). Peaks $\boxed{1}$ and $\boxed{2}$ are merged together due to the lower resolution at higher energy. There is another peak around 45 meV which increases with increasing temperature and is therefore due to transitions between excited levels. This peak could therefore be due to a transition between peaks $\boxed{1}$ or $\boxed{2}$ (or both) to excited levels around $\sim$60 meV. The results for Ba_2ErSbO_6 are summarised in table 3.7.

A peak observed in inelastic neutron scattering can only be attributed to being due to transitions between crystal field energy levels if it follows $F^2(Q)$, where $F(Q)$ is the form factor for the magnetic ion, due to rule 4 in section 3.5.2. The peaks were therefore tested to ensure they were not due to other phenomena, such as phonons. The results for Ba_2HoSbO_6 are shown in figure 3.17. All the peaks can be seen to be following $F^2(Q)$ and along with their temperature behaviour can be confidently attributed as resulting due to crystal field transitions.

Similarly the peaks identified for Ba_2HoSbO_6 are shown in figure 3.18. They also follow $F^2(Q)$ and are attributed to CEF excitations during the INS experiment.

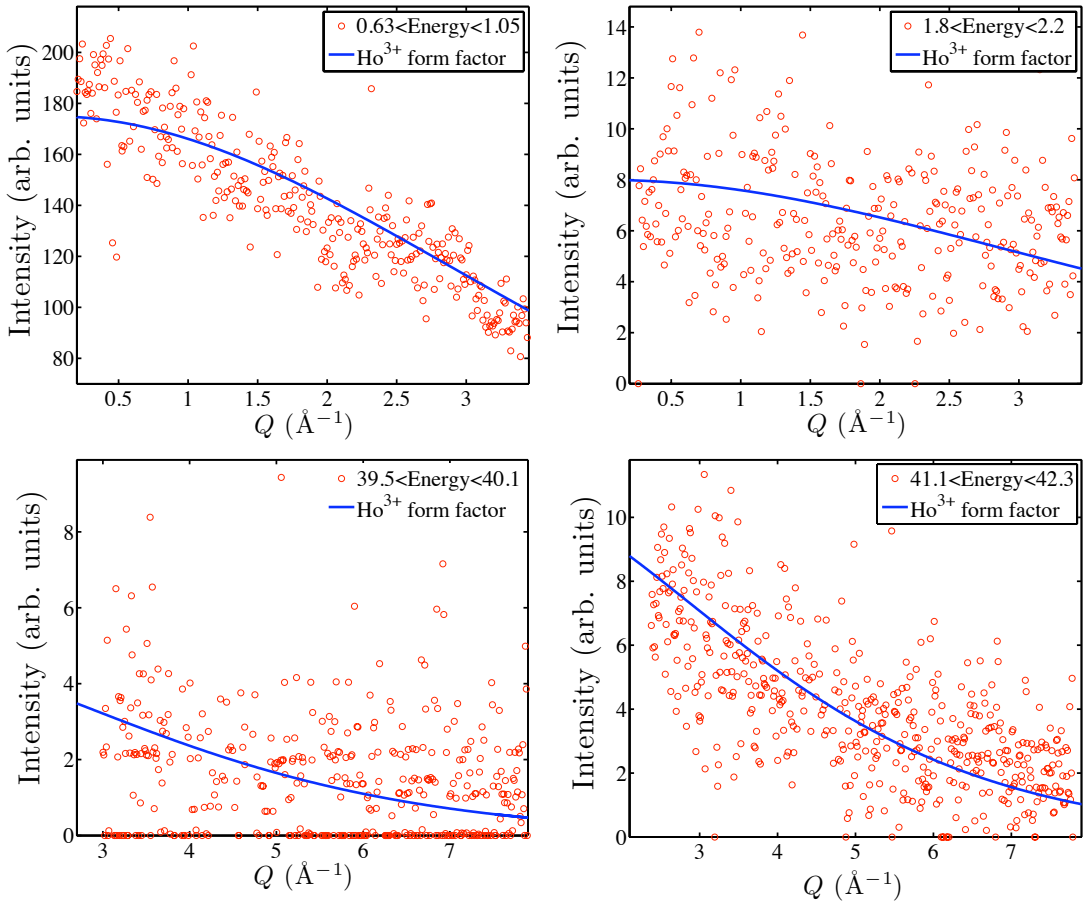

Figure 3.17: [Ba_2HoSbO_6] Variation of intensity against Q for constant energy from inelastic neutron scattering for Ba_2HoSbO_6. The solid line is $F^2(Q)$ for Ho^{3+}.

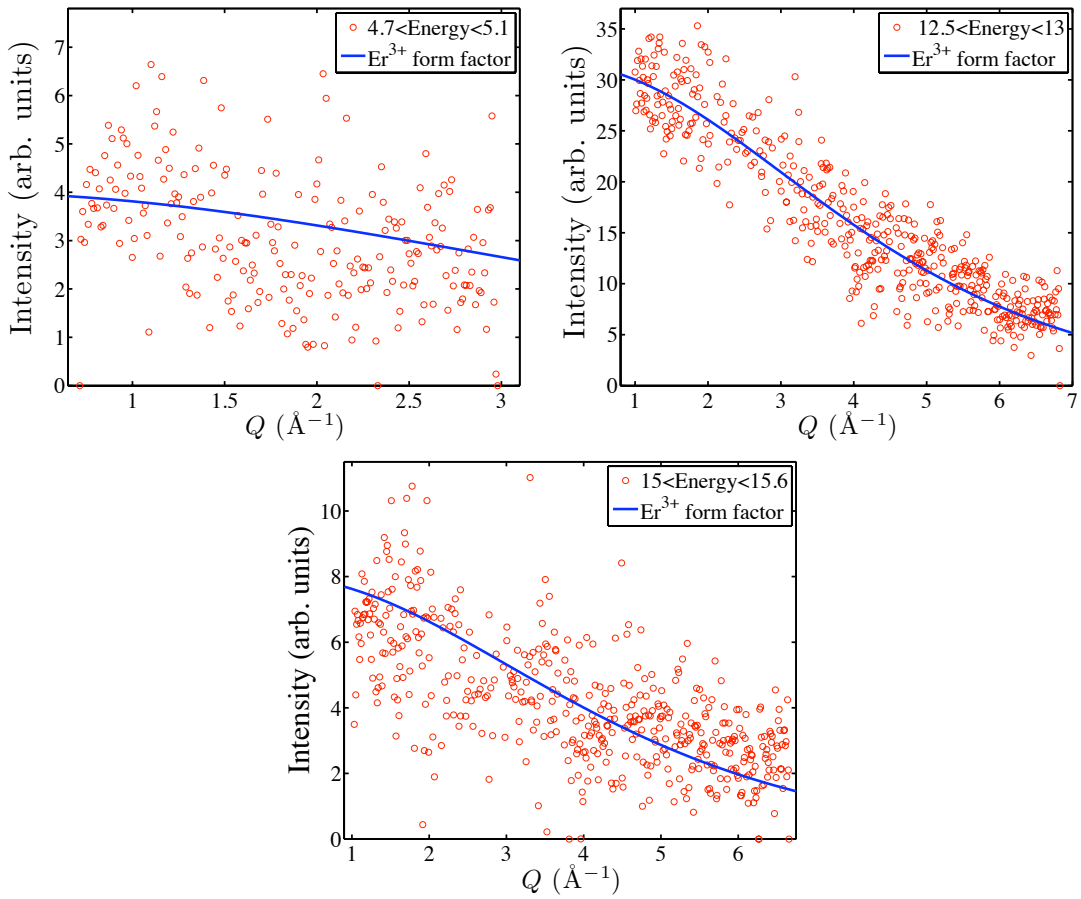

Figure 3.18: [Ba_2ErSbO_6] Variation of intensity against Q for constant energy from inelastic neutron scattering for Ba_2ErSbO_6. The solid line is $F^2(Q)$ for Er^{3+}.

3.5.4 Using inelastic neutron scattering results to obtain the CEF level scheme

Ba_2HoSbO_6 and Ba_2ErSbO_6 have the same structural symmetry, namely cubic space group and cubic point symmetry. This means the LLW method of finding the crystal field parameters, discussed in section 3.4.1, is applicable. This reduced the problem of varying the two crystal field parameters to a linear problem of varying only the value of x. Starting from the LLW plots in figure 3.13 all the possible x positions that could be reasonably matched to the INS results where fitted using the least squared fitting package FOCUS obtained through ISIS [125]. This software reads in the experimental data and then plots a fit over the top using instrumental and experimental parameters. The two CEF parameters B_4^0 and B_6^0 are free to be varied and these determine the position and intensity of the peaks. Values for the predicted energy levels and the excitations are outputted, along with the predicted eigenvectors.

3.5.5 Determining the CEF level scheme for Ho^{3+} in Ba_2HoSbO_6

Looking at the predicted energy levels for the $J = 8$ case it appears there might be several regions which are candidates for the correct fitting parameters, such as around $x = -0.5$ with negative W, or around $x = 0.9$ with negative W. LLW provide predictions based on the point charge model as to what the sign of x and W should be. A more reliable test is the fact that INS probes both the eigenvalues (i.e. the energy level values) and the eigenfunctions which determine the intensity of the transitions. Hence the predicted eigenfunctions for a set of parameters give out expected intensities at each eigenvalue and this allows for a check of the parameters by looking at the experimental intensities.

For Ho^{3+} in Ba_2HoSbO_6 the $x = 0.761$ position and intensity $W = -0.0504$ meV

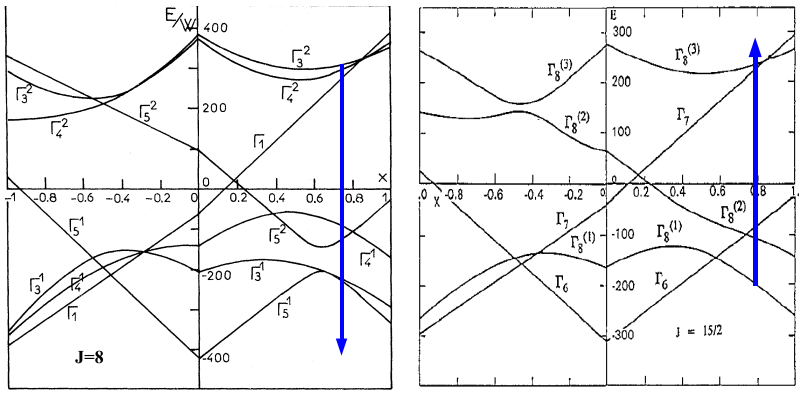

(a) J = 8 (b) J = 15/2

Figure 3.19: LLW energy levels [115] for (a) $J = 8$ corresponding to Ho^{3+} in Ba_2HoSbO_6 and (b) $J = 15/2$ corresponding to Er^{3+} in Ba_2ErSbO_6. The blue lines represents the x positions in LLW notation found to reproduce the experimental results most accurately. The direction the arrow points shows the direction in which the energy increases and hence gives the ordering of the CEF levels from lowest energy to highest. The arrow points in the opposite direction in the two plots indicating for Ho^{3+} the ground state is $\Gamma_3^{(2)}$ whereas for Er^{3+} the ground state is $\Gamma_8^{(1)}$, with the excited states given by the arrow direction at fixed x.

(area highlighted in figure 3.19(b)), where the negative defines the direction of the vertical axes, was found to be the only one that matched the positions and intensities of the crystal field peaks. A good fit to the observed data using the parameters for Ba_2HoSbO_6 was produced for all temperatures, as shown in figure 3.20.

The CEF parameters for Ho^{3+} in Ba_2HoSbO_6 are therefore found to be:

$$B_4^0 = -0.123 \times 10^{-2} \text{ meV}$$

$$B_6^0 = -0.167 \times 10^{-5} \text{ meV}$$

with an error of $\pm 0.007 \times 10^{-2}$ meV and $\pm 0.007 \times 10^{-5}$ meV on B_4^0 and B_6^0, respectively. These CEF parameters provide a very powerful tool and will be used below to explain the temperature and field dependent neutron scattering behaviour reported here and to predict further magnetic properties.

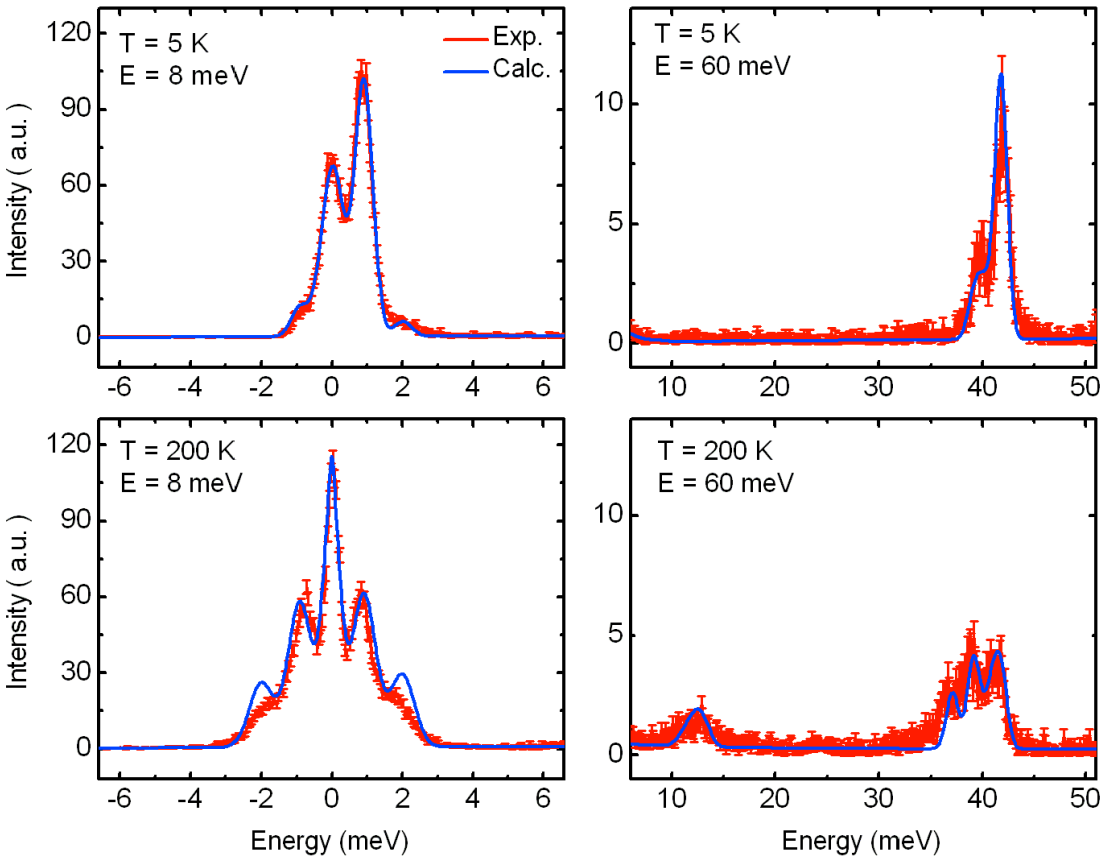

Figure 3.20: [Ba_2HoSbO_6] The solid line shows the best fit of the INS data (crosses) using the FOCUS fitting package. The fits were obtained using the same crystal field parameters throughout. In LLW notation $x = 0.761$. Good agreement are observed for the peak positions at all temperatures. For E_i = 8 meV and $T = 200$ K, however, discrepancies between the fitted intensity and the measured intensity is observed and this is attributed to limited control over the linewidth within FOCUS.

The parameters give a good fit to the positions of the observed peaks for all the temperatures and energies. There is, however, not exact agreement in the predicted intensity and the actual intensity of the excited peak which occurs around 2 meV for the data taken at 200 K. There are several possible explanations for this, assuming that the crystal field parameters being used are correct. The high calculated intensity could be due to the line width of this excitation being bigger than the other excitations. This would mean the parameters are correct and that the model used by the fitting software is not predicting the correct intensities or there is not enough control in the software to vary the width of the peaks. The peak may not be simply due to the crystal field. The structure of the rare earth double perovskites Ba_2RSbO_6 may not be strictly cubic. The peak may not be dispersionless. The predictions made by this model could be checked against another fitting model. There is work under way to produce a model using the MATLAB programming language which should give more control and hence give more confidence in the results obtained. By working on this new model there will be a deeper understanding of any discrepancies between calculated and measured spectra.

3.5.6 Determining the CEF level scheme for Er^{3+} in Ba_2ErSbO_6

The same strategy of trying all sensible positions on the LLW tables and performing a least squares analysis was employed for Er^{3+} in Ba_2ErSbO_6, however it was not possible to achieve such good agreement when trying to fit all the peaks i, ii, 1, 2 and 3 identified. This could be indicative of Ba_2ErSbO_6 changing from its ideal cubic symmetry to a lower symmetry which is too subtle to be picked up by neutron scattering. However the previous experiments have shown that this sample of Ba_2ErSbO_6 contains an impurity phase of Er_2O_3 and as discussed this has a CEF level around 5 meV. Peak ii occurs at 5 meV and can thus be attributed to Er_2O_3. Ignoring the low energy peaks and

trying to fit the two peaks around 12 and 15 meV which can be attributed to Ba_2ErSbO_6 leads to a unique CEF level scheme.

The region marked in figure 3.19 at $x = 0.8$ gives the CEF parameters which replicate the observed levels and intensities found in the neutron results most accurately. This also agrees with the parameters obtained when converting the result for Ho^{3+} to Er^{3+}, see section 3.8. The resultant fit using FOCUS is shown in figure 3.21.

Therefore for Er^{3+} in Ba_2ErSbO_6 the following parameters are proposed as the best fit for the obtained data:

$$B_4^0 = 0.179 \times 10^{-2} \text{ meV}$$

$$B_6^0 = 0.194 \times 10^{-5} \text{ meV}$$

with an error of $\pm 0.007 \times 10^{-2}$ and $\pm 0.007 \times 10^{-5}$ on B_4^0 and B_6^0, respectively.

3.5.7 The CEF level scheme for Ho^{3+} and Er^{3+} in Ba_2RSbO_6 (R = Ho, Er)

The parameters obtained for Ho^{3+} and Er^{3+} give the CEF energy level schemes shown in figure 3.22. The predicted level schemes for Ba_2HoSbO_6 and Ba_2ErSbO_6 are markedly different.

The lowest lying energy level for Ba_2HoSbO_6 is in Bethe's notation Γ_3 [112], which is a non-magnetic doublet. The Γ_3 doublet is non-magnetic since both degenerate eigenstates ($\Gamma_3(a)$ and $\Gamma_3(b)$) have symmetric wavefunctions with no matching m_J states between the wavefunctions, as shown in table 3.8. For Ho^{3+} in Ba_2HoSbO_6:

$$\begin{aligned}
\Gamma_3(a) &= 0.574|{-8.0}\rangle - 0.229|{-4.0}\rangle - 0.486|0\rangle - 0.229|4.0\rangle + 0.574|8.0\rangle \\
\Gamma_3(b) &= 0.045|{-6.0}\rangle + 0.706|{-2.0}\rangle + 0.706|2.0\rangle + 0.045|6.0\rangle
\end{aligned}$$

Hence the magnetic moment, given by the expectation $\mu = g_J|\langle\Gamma_i|J_z|\Gamma_i\rangle|\mu_B$, is zero.

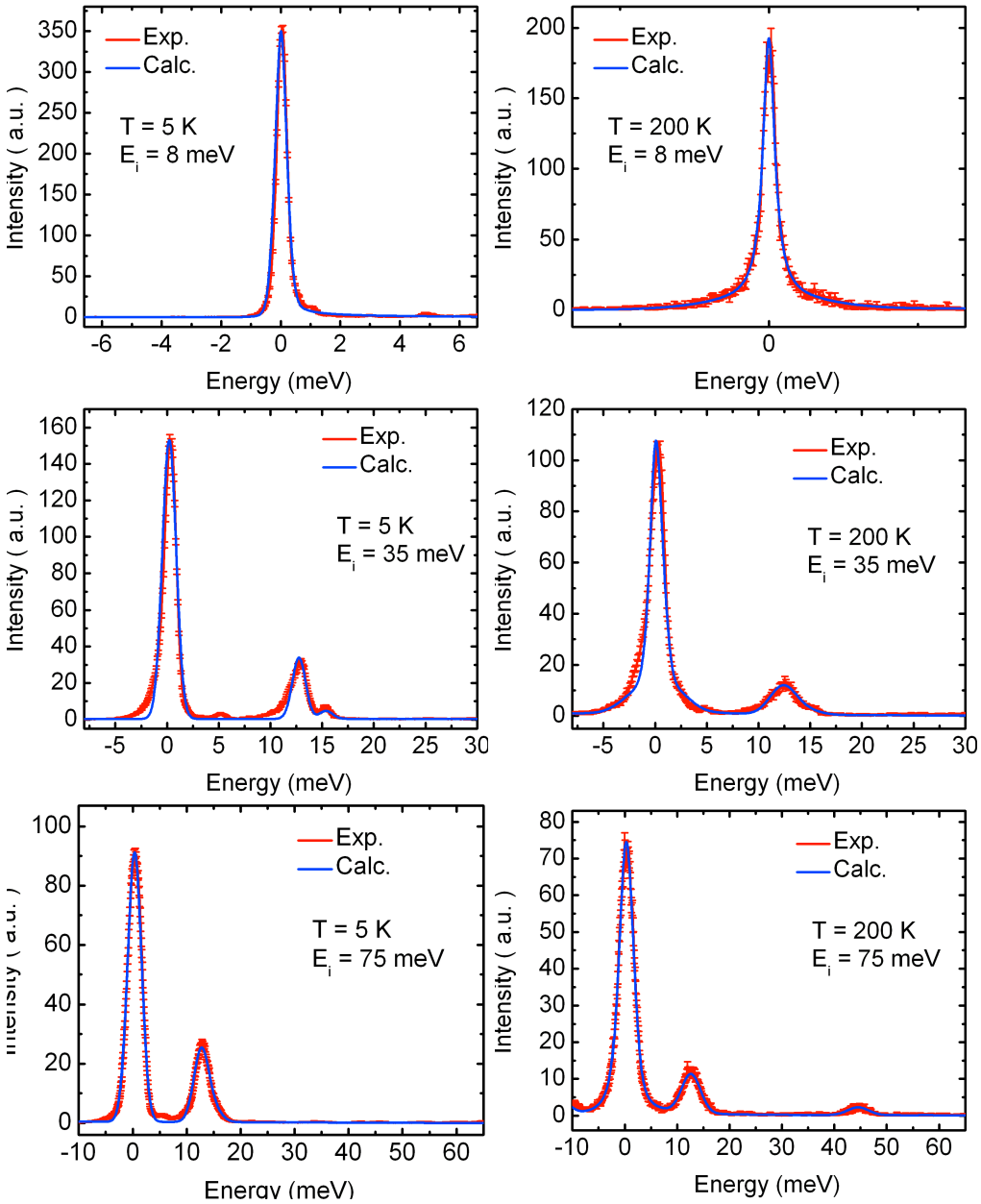

Figure 3.21: [Ba_2ErSbO_6] The solid line shows the best fit of the INS data (crosses) using the FOCUS fitting package. The fits were obtained using the same crystal field parameters throughout. The fits were obtained using the crystal field parameters $B_4^0 = 0.179 \times 10^{-2}$ meV and $B_6^0 = 0.194 \times 10^{-5}$ meV.

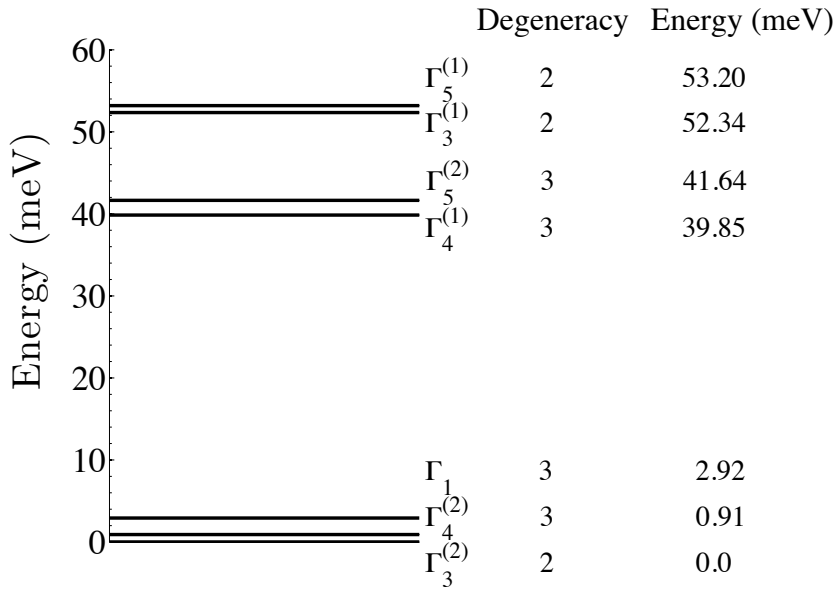

(a) Ho^{3+}

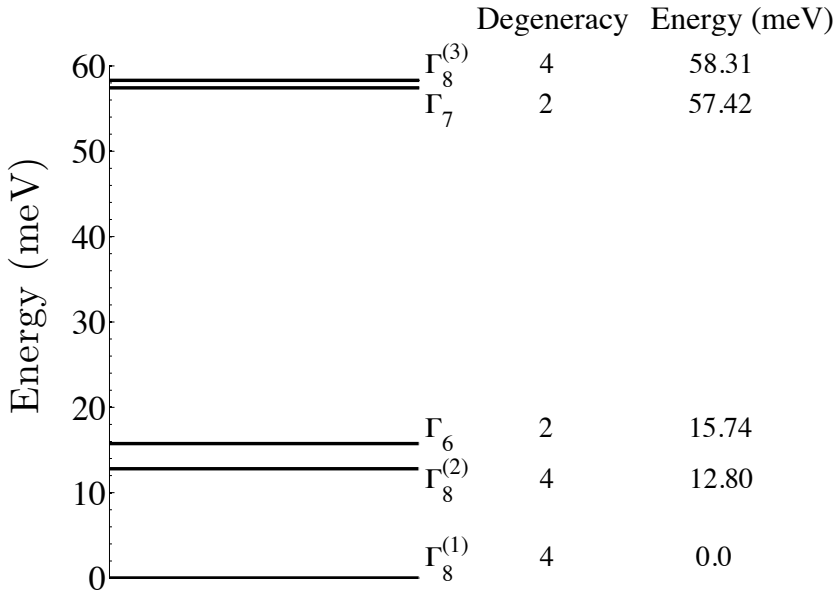

(b) Er^{3+}

Figure 3.22: The predicted crystal field energy levels for (a) Ba_2HoSbO_6 and (b) Ba_2ErSbO_6. The Ho^{3+} ion has three low lying energy levels which dominate the low temperature behaviour. The ground state is non-magnetic with a closely separated magnetic level at 0.91meV ($\sim$11 K) above the ground state, this is expected to result in magnetic behavior due to population of this magnetic level at finite temperatures. The Er^{3+} ion has a magnetic ground state well separated from the first excited state. This is predicted to dominate the magnetic behaviour.

Wavefunction	E (meV)
$\|\Gamma_5^{(1)}(a)\rangle = 0.029\|-7\rangle + 0.347\|-5\rangle + 0.304\|-3\rangle - 0.160\|-1\rangle - 0.362\|1\rangle + 0.135\|3\rangle + 0.782\|5\rangle + 0.013\|7\rangle$	53.20
$\|\Gamma_5^{(1)}(b)\rangle = -0.012\|-7\rangle + 0.782\|-5\rangle - 0.135\|-3\rangle - 0.362\|-1\rangle + 0.160\|1\rangle + 0.304\|3\rangle - 0.347\|5\rangle + 0.029\|7\rangle$	53.20
$\|\Gamma_5^{(1)}(c)\rangle = 0.673\|-6\rangle + -0.216\|-2\rangle + 0.216\|2\rangle - 0.673\|6\rangle$	53.20
$\|\Gamma_3^{(1)}(d)\rangle = 0.033\|-8\rangle + 0.612\|-4\rangle + -0.498\|0\rangle + 0.612\|4\rangle + 0.033\|8\rangle$	52.34
$\|\Gamma_3^{(1)}(e)\rangle = 0.706\|-6\rangle - 0.045\|-2\rangle - 0.045\|2\rangle + 0.706\|6\rangle$	52.34
$\|\Gamma_5^{(2)}(f)\rangle = 0.741\|-7\rangle + 0.030\|-5\rangle + 0.505\|-3\rangle + 0.023\|-1\rangle - 0.263\|1\rangle - 0.043\|3\rangle - 0.345\|5\rangle - 0.064\|7\rangle$	41.64
$\|\Gamma_5^{(2)}(g)\rangle = 0.064\|-7\rangle + -0.345\|-5\rangle + 0.043\|-3\rangle - 0.263\|-1\rangle - 0.023\|1\rangle + 0.505\|3\rangle - 0.030\|5\rangle + 0.741\|7\rangle$	41.64
$\|\Gamma_5^{(2)}(h)\rangle = -0.2155\|-6\rangle - 0.673\|-2\rangle + 0.673\|2\rangle + 0.2155\|6\rangle$	41.64
$\|\Gamma_4^{(1)}(i)\rangle = -0.100\|-7\rangle + 0.346\|-5\rangle + 0.086\|-3\rangle + 0.329\|-1\rangle - 0.051\|1\rangle - 0.560\|3\rangle - 0.053\|5\rangle + 0.659\|7\rangle$	39.85
$\|\Gamma_4^{(1)}(j)\rangle = 0.659\|-7\rangle + 0.053\|-5\rangle - 0.560\|-3\rangle + 0.051\|-1\rangle + 0.329\|1\rangle - 0.086\|3\rangle + 0.346\|5\rangle + 0.101\|7\rangle$	39.85
$\|\Gamma_4^{(1)}(k)\rangle = 0.0495\|-8\rangle + 0.705\|-4\rangle - 0.705\|4\rangle - 0.0495\|8\rangle$	39.85
$\|\Gamma_1\rangle = 0.411\|-8\rangle + 0.270\|-4\rangle + 0.718\|0\rangle + 0.270\|4\rangle + 0.411\|8\rangle$	2.92
$\|\Gamma_4^{(2)}(l)\rangle = 0.705\|-8\rangle - 0.050\|-4\rangle 0.050\|4\rangle - 0.705\|8\rangle$	0.91
$\|\Gamma_4^{(2)}(m)\rangle = -0.015\|-7\rangle + 0.001\|-5\rangle + 0.558\|-3\rangle + 0.005\|-1\rangle + 0.814\|1\rangle + 0.003\|3\rangle + 0.160\|5\rangle$	0.91
$\|\Gamma_4^{(2)}(n)\rangle = 0.160\|-5\rangle - 0.003\|-3\rangle + 0.814\|-1\rangle - 0.005\|1\rangle + 0.558\|3\rangle - 0.001\|5\rangle - 0.016\|7\rangle$	0.91
$\|\Gamma_3^{(2)}(o)\rangle = 0.574\|-8\rangle - 0.229\|-4\rangle - 0.486\|0\rangle - 0.229\|4\rangle + 0.574\|8\rangle$	0
$\|\Gamma_3^{(2)}(p)\rangle = 0.045\|-6\rangle + 0.706\|-2\rangle + 0.706\|2\rangle + 0.045\|6\rangle$	0

Table 3.8: [Ba_2HoSbO_6] Wavefunctions and energies for the CEF level scheme of Ho^{3+} in Ba_2HoSbO_6.

Wavefunction	E (meV)
$\Gamma_8^{(3)}(a) = 0.026\|-\frac{13}{2}\rangle + 0.617\|-\frac{5}{2}\rangle + 0.004\|-\frac{3}{2}\rangle + 0.780\|\frac{3}{2}\rangle + 0.003\|\frac{5}{2}\rangle + 0.100\|\frac{11}{2}\rangle$	58.31
$\Gamma_8^{(3)}3(b) = 0.100\|-\frac{11}{2}\rangle - 0.003\|-\frac{5}{2}\rangle + 0.780\|-\frac{3}{2}\rangle - 0.004\|\frac{3}{2}\rangle + 0.617\|\frac{5}{2}\rangle + 0.026\|\frac{13}{2}\rangle$	58.31
$\Gamma_8^{(3)}(c) = -0.131\|-\frac{9}{2}\rangle - 0.505\|-\frac{1}{2}\rangle - 0.258\|\frac{7}{2}\rangle + 0.813\|\frac{15}{2}\rangle$	58.31
$\Gamma_8^{(3)}(d) = 0.813\|-\frac{15}{2}\rangle - 0.258\|-\frac{7}{2}\rangle - 0.505\|0.5\rangle - 0.132\|\frac{9}{2}\rangle$	58.31
$\Gamma_7(e) = 0.191\|-\frac{9}{2}\rangle + 0.718\|-\frac{1}{2}\rangle + 0.331\|\frac{7}{2}\rangle + 0.582\|\frac{15}{2}\rangle$	57.42
$\Gamma_7(f) = 0.582\|-\frac{15}{2}\rangle + 0.331\|-\frac{7}{2}\rangle + 0.718\|\frac{1}{2}\rangle + 0.191\|\frac{9}{2}\rangle$	57.42
$\Gamma_6(g) = 0.633\|-\frac{13}{2}\rangle + 0.582\|-\frac{5}{2}\rangle - 0.451\|\frac{3}{2}\rangle - 0.239\|\frac{11}{2}\rangle$	15.74
$\Gamma_6(h) = -0.238\|-\frac{11}{2}\rangle - 0.451\|-\frac{3}{2}\rangle + 0.582\|\frac{5}{2}\rangle + 0.633\|\frac{13}{2}\rangle$	15.74
$\Gamma_8^{(2)}(i) = 0.018\|-\frac{15}{2}\rangle + 0.803\|-\frac{7}{2}\rangle - 0.239\|\frac{1}{2}\rangle - 0.546\|\frac{9}{2}\rangle$	12.80
$\Gamma_8^{(2)}(j) = -0.545\|-\frac{9}{2}\rangle - 0.239\|-\frac{1}{2}\rangle + 0.803\|\frac{7}{2}\rangle + 0.018\|\frac{15}{2}\rangle$	12.80
$\Gamma_8^{(2)}(k) = 0.234\|-\frac{13}{2}\rangle + 0.215\|-\frac{11}{2}\rangle - 0.148\|-\frac{5}{2}\rangle + 0.317\|-\frac{3}{2}\rangle + 0.101\|\frac{3}{2}\rangle - 0.468\|\frac{5}{2}\rangle + 0.068\|\frac{11}{2}\rangle + 0.737\|\frac{13}{2}\rangle$	12.80
$\Gamma_8^{(2)}(l) = 0.737\|-\frac{13}{2}\rangle - 0.068\|-\frac{11}{2}\rangle - 0.468\|-\frac{5}{2}\rangle - 0.101\|-\frac{3}{2}\rangle + 0.317\|\frac{3}{2}\rangle + 0.148\|\frac{5}{2}\rangle + 0.215\|\frac{11}{2}\rangle - 0.234\|\frac{13}{2}\rangle$	12.80
$\Gamma_8^{(1)}(m) = 0.007\|-\frac{15}{2}\rangle + 0.424\|-\frac{7}{2}\rangle - 0.415\|\frac{1}{2}\rangle + 0.805\|\frac{9}{2}\rangle$	0
$\Gamma_8^{(1)}(n) = 0.805\|-\frac{9}{2}\rangle - 0.415\|-\frac{1}{2}\rangle + 0.424\|\frac{7}{2}\rangle + 0.007\|\frac{15}{2}\rangle$	0
$\Gamma_8^{(1)}(o) = 0.939\|-\frac{11}{2}\rangle - 0.001\|-\frac{5}{2}\rangle - 0.278\|-\frac{3}{2}\rangle + 0.002\|\frac{3}{2}\rangle + 0.200\|\frac{5}{2}\rangle - 0.007\|\frac{11}{2}\rangle - 0.027\|\frac{13}{2}\rangle$	0
$\Gamma_8^{(1)}(p) = -0.026\|-\frac{13}{2}\rangle + 0.007\|-\frac{11}{2}\rangle + 0.200\|-\frac{5}{2}\rangle - 0.002\|-\frac{3}{2}\rangle - 0.278\|\frac{3}{2}\rangle + 0.001\|\frac{5}{2}\rangle + 0.939\|\frac{11}{2}\rangle$	0

Table 3.9: [Ba_2ErSbO_6] Wavefunctions and energies for the CEF level scheme of Er^{3+} in Ba_2ErSbO_6.

This is also the case for the singlet Γ_1. This supports the lack of magnetic ordering observed in the investigations carried out so far on Ba_2HoSbO_6. It is, however, important to note that the presence of a non-magnetic ground state does not preclude the development of magnetic order in the system since this can occur through mixing of higher crystal field levels into the ground state by the magnetic exchange interaction. This possibility is considered later in this chapter.

The three closely spaced lowest energy levels in Ba_2HoSbO_6, two non-magnetic levels ($\Gamma_3^{(2)}$ and Γ_1) and one magnetic ($\Gamma_4^{(2)}$), suggests that they are governing the field dependent results.

Er^{3+} in Ba_2ErSbO_6 has a well separated magnetic ground state that will control the magnetic behaviour.

3.5.8 Application of a magnetic field within the single ion CEF model

An applied field induces a splitting of crystal field levels and lifts the degeneracy leading to the possibility of crossover of the lowest lying energy levels. This idea of level crossover and associated magnetic anomalies has been investigated in other compounds [126–129].

The effect of an applied field, $\mathbf{H}$, on the crystal field levels can be predicted by adding the Zeeman term, $H_Z = -g_j\mu_{\rm B}\mathbf{H}.\mathbf{J}$, to the CEF Hamiltonian shown in equation 3.8 to produce the following:

$$\mathscr{H}_{\rm field} = B_4^0[O_4^0 + 5O_4^4] + B_6^0[O_6^0 - 21O_6^4] - g_j\mu_{\rm B}\mathbf{H}.\mathbf{J} \qquad (3.13)$$

This neglects other terms which will have an influence on the energy levels in an applied field that make up the full in field Hamiltonian $\mathscr{H} = H_{\rm CF} + H_{\rm Z} + H_{\rm B} + H_{\rm QT}$. Here $H_{\rm B}$ is the bilinear term describing the interaction of the $4f$ angular momentum J

with the external applied field and exchange fields and H_{QT} is the quadrupolar interaction. The results calculated here for the applied field energy level variation are therefore only to be taken as an approximation to the true behaviour.

The small separation in CEF GS and 1st excited energy levels in Ba_2HoSbO_6 could result in crossover and lead to interesting experimental consequences. In this way the magnetic ground state that has been precluded by Ho^{3+} adopting a non-magnetic crystal field ground state would be allowed to manifest itself in small fields. This feature would give a large and interesting scope of investigation of frustration effects and a unique experimental control. The results are shown in figure 3.23. They show no evidence of level crossing of the non-magnetic GS in Ba_2HoSbO_6 using equation 3.13.

Figure 3.24 shows the effect the applied magnetic field has on the CEF levels of Er^{3+} in Ba_2ErSbO_6. They can be seen to split with a linear behaviour. The energy level splitting is largely unaffected by the field direction.

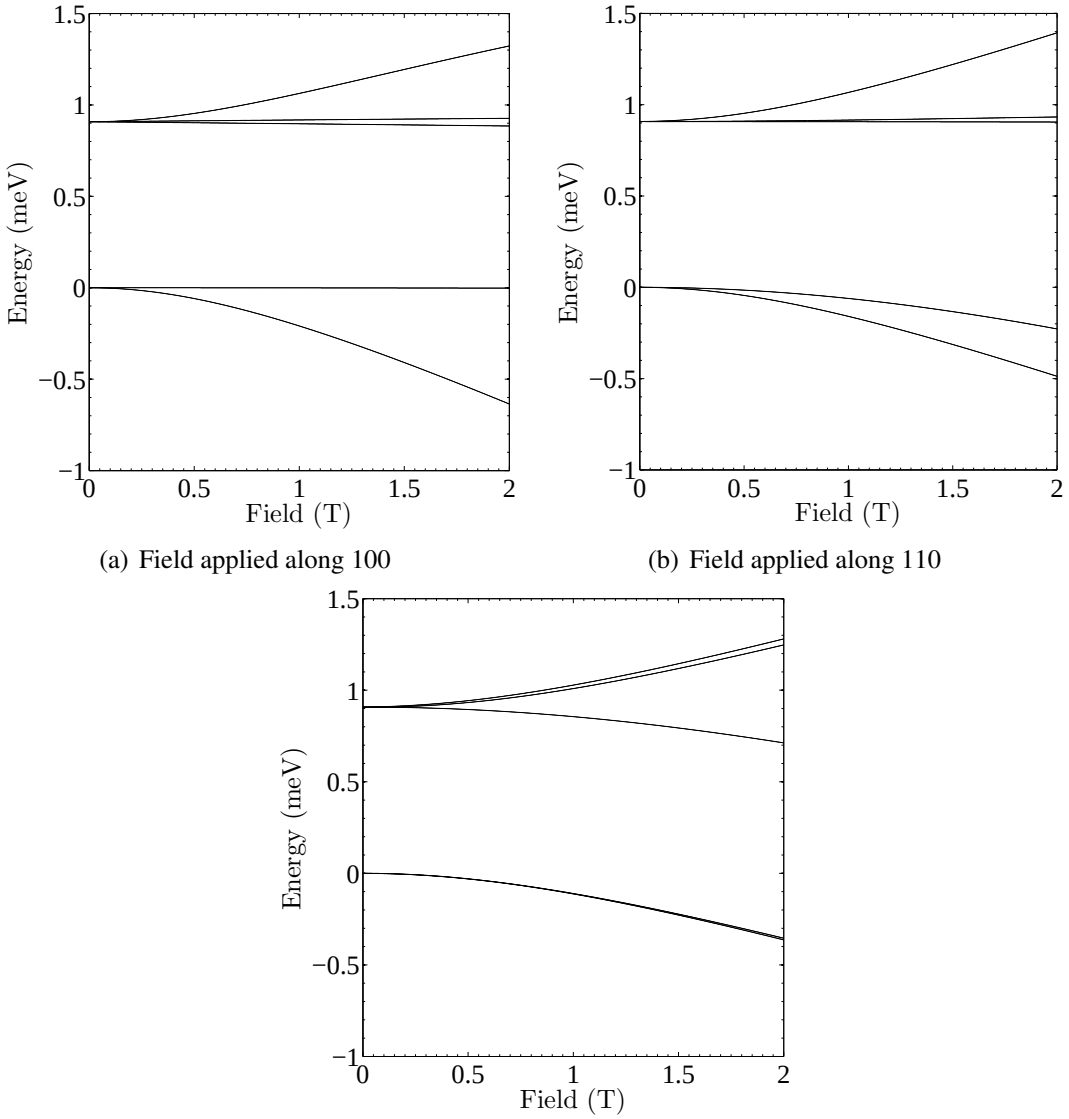

(a) Field applied along 100

(b) Field applied along 110

(c) Field applied along 111

Figure 3.23: [Ba_2HoSbO_6] Calculated splitting of CEF energy levels in an applied magnetic field for Ba_2HoSbO_6 as calculated using equation 3.13.

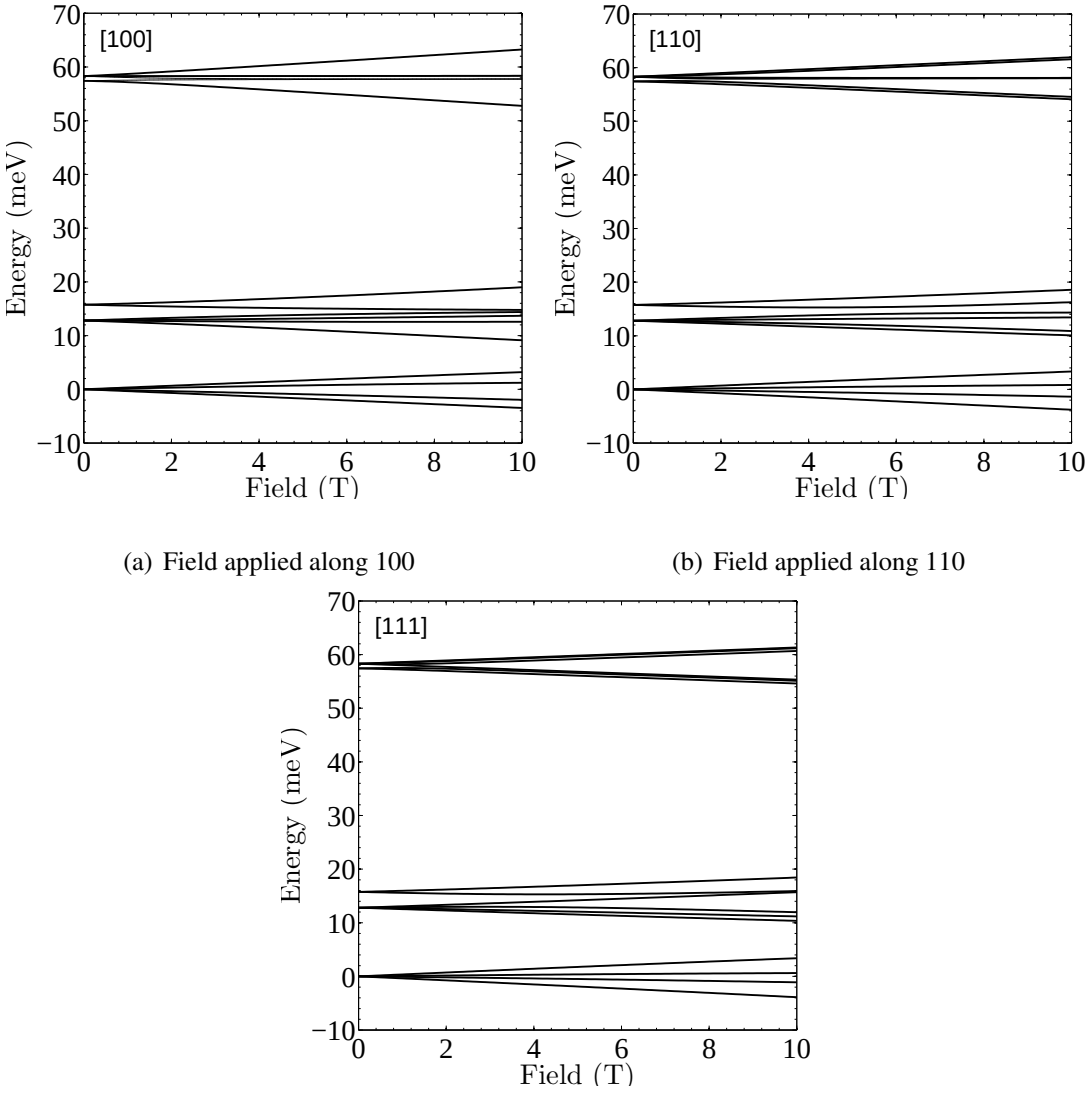

(a) Field applied along 100

(b) Field applied along 110

(c) Field applied along 111

Figure 3.24: [Ba_2ErSbO_6] Splitting of energy levels for Er^{3+} in Ba_2ErSbO_6 due to an applied field as calculated using equation 3.13.

3.6 Properties of Ba_2HoSbO_6 obtained using crystal field parameters

The solved crystal field level scheme gives an unambiguous explanation as to why no magnetic ordering is observed in zero field neutron experiments for Ba_2HoSbO_6. The obtained crystal field parameters also allow the opportunity to derive exact results for the magnetic moment, susceptibility, magnetisation and specific heat.

3.6.1 Calculation of susceptibility for Ba_2HoSbO_6

Van Vleck was responsible for much of the early work on relating the burgeoning field of quantum mechanics to magnetism. He related susceptibility to the wavefunctions derived from the crystal field Hamiltonian, thus allowing an exact prediction of how the induced magnetic moment should vary with temperature. The magnetic susceptibility per mole χ is derived here by creating a $(2J+1) \times (2J+1)$ matrix of the expectation values of J_Z from the crystal field parameters and applying equation 1.10 introduced in section 1.1.2. The wavefunctions and energies are shown in tables 3.8 and 3.9.

The first term of equation 1.10 only contains terms within each degenerate crystal field level. These correspond to diagonal elements of the matrix of J_z for the Ho^{3+} ion in Ba_2HoSbO_6 which cause the Curie-Weiss paramagnetic behaviour. The non-diagonal elements describe transitions between the non-degenerate energy levels and give the Van Vleck temperature independent paramagnetic behaviour.

The resultant calculated Van Vleck susceptibility for Ba_2HoSbO_6 is shown in figure 3.25. This result agrees with published susceptibility results [26], as will be shown later in section 3.6.4.

An interesting point to note is that the application of the Curie-Weiss law (as defined in equation 1.9) to the calculated susceptibility over the range 100 to 250 K gives

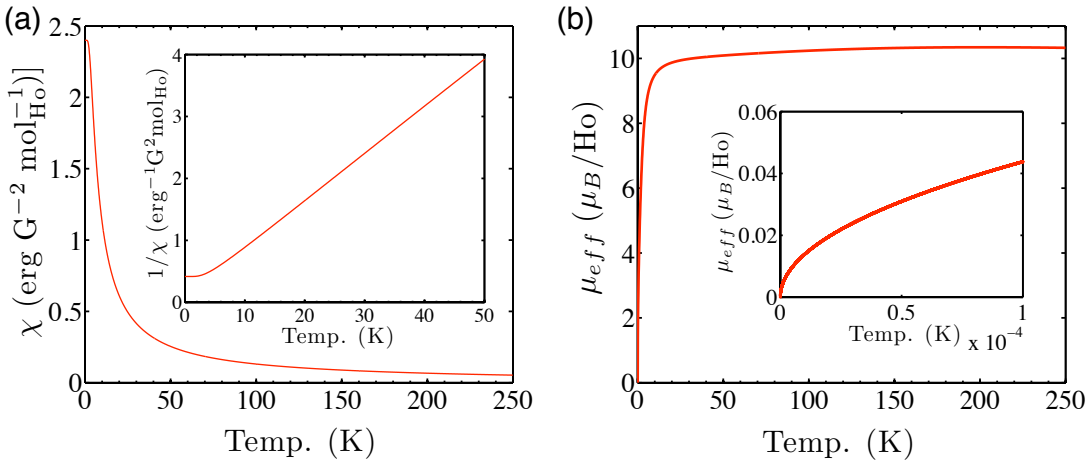

Figure 3.25: [Ba_2HoSbO_6] (a) Van Vleck susceptibility for Ba_2HoSbO_6 calculated from the crystal field parameters. No magnetic ordering with temperature is observed. (b) Effective moment calculated from the Van Vleck susceptibility. The effective moment agrees with the free ion moment of Ho^{3+} down to 20 K. As the temperature goes below 20 K the effective moment is seen to drop off dramatically and reaches $0\mu_B$ at 0 K indicating no induced magnetic moment in zero field.

a magnetic moment of $10\mu_B$. This agrees well with the free ion moment of $10.6\mu_B$ for Ho^{3+}. This does not, however, preclude a non-magnetic ground state since it only takes account of the magnetic moment over the region at which the Curie-Weiss law was applied, which means in this case higher magnetic CEF levels are populated and contribute to the moment. The Curie-Weiss method is an estimate of the magnetic moment with the true answer being given by the crystal field Hamiltonian.

The non-magnetic ground state gives a magnetic moment of $0\mu_B$. The first excited state has a magnetic moment of $0.18\mu_B$. Taking into account second order transitions between the ground state and the first excited state through:

$$\mu = \frac{g_J \sum_{i,j} \langle \Gamma_i | J_z | \Gamma_j \rangle}{E_i - E_j} \mu_B \tag{3.14}$$

gives $\mu = 5.1\mu_B$. This value is similar to the magnetic moment contribution from the CEF GS for the frustrated rare earth pyrochlore $Er_2Ti_2O_7$ [42], giving confidence to the

postulate of interesting field induced behaviour. The effective moment found from the calculated susceptibility gives the true moment as a function of temperature through the identity $\mu_{eff} \equiv 2.827\sqrt{\chi_m T}$ and is shown in figure 3.25(b). The moment remains at close to the free ion moment of $10.6\mu_{\rm B}$ down to around 20 K. Then there is a sharp drop off due to depopulation of excited states due to thermal excitations being ever more statistically prohibited until the moment reaches $0\mu_{\rm B}$ at 0 K indicating there is no induced moment effects in zero field. Experimental confirmation of this would provide clear evidence of the non-magnetic ground state in which there is no mixing of levels due to exchange interactions which would lead to a non-zero induced moment at 0 K.

This therefore explains the mechanism involved in producing the form factor behaviour observed in xyz polarized neutron scattering. Since a neutron measures $\chi(Q)$, if the susceptibility is large then the neutron scattering will reflect this and produce the observed form factor dependence. It rules out the possibility of there being any induced moment due to mixing of energy levels which can occur if the critical ratio of the effective exchange field to the crystal field is reached. The single ion crystal field model used here can explain all the zero field behaviour observed for Ba_2HoSbO_6 to date, but as a conclusive test then this low temperature magnetic moment variation would unambiguously show if the dominant behaviour is due to single ion effects in Ba_2HoSbO_6 or if there are further interactions that lead to an induced moment that lie out with this model.

3.6.2 Calculation of magnetisation for Ba_2HoSbO_6

The magnetisation $M(H,T)$ is found by adding the Zeeman term to the crystal field Hamiltonian and is given by the following equation [130]:

$$M(H,T) = g_j\mu_{\rm B}\frac{\sum_i < i|\mathbf{J}.\hat{\mathbf{H}}|i > \exp(\frac{-E_i(H)}{kT})}{\sum_i \exp(\frac{-E_i(H)}{kT})} \tag{3.15}$$

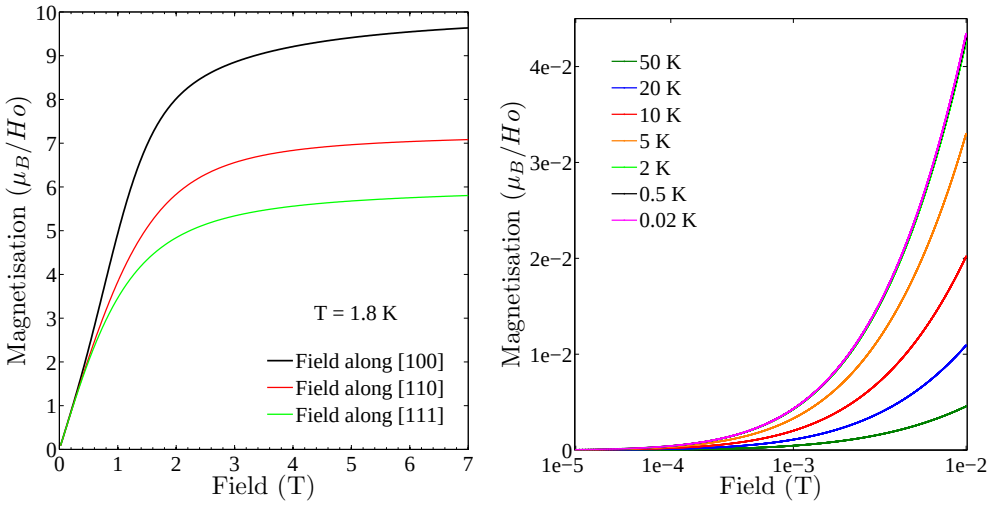

Figure 3.26: [Ba_2HoSbO_6] (Left) Calculated magnetisation from CEF parameters for Ba_2HoSbO_6 at 1.8 K. (Right) Low field calculated magnetisation on double log scale.

The result for Ba_2HoSbO_6 at 1.8 K is shown in figure 3.26. The magnetisation is not observed to saturate in fields up to 7 T, with differing behaviour observed depending on what axis the field is applied along.

The calculated magnetisation can be used to provide evidence of any crossover field, H_c, and highlight other anomalies in the magnetisation curves that could be indicating magnetic anomalies. A magnetic field induced change is characterized by a deviation of the magnetic moment and is shown by a dM/dH peak. This can be seen to occur in low fields for Ba_2HoSbO_6, as shown in figure 3.27. For a field applied along the $[100]$ or $[110]$ axis a peak centred below 1 T is present, indicating H_c of less than 1 T. This peak is temperature dependent and shifts to smaller fields as the temperature is decreased, as observed in similar field induced phase transitions [131]. This could suggest that a crossover has occurred, however the calculated splitting of CEF energy levels in an applied field do not support there being any crossover around this field. In the $[110]$ direction the only peak between 0 to 500 T occurs around 200 T. For a field applied

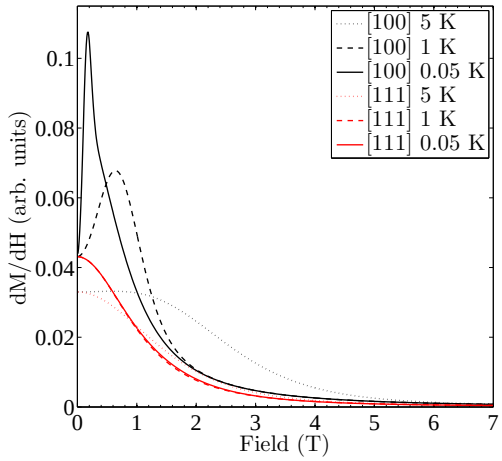

(a) Low field induced magnetic anomaly for Ba_2HoSbO_6

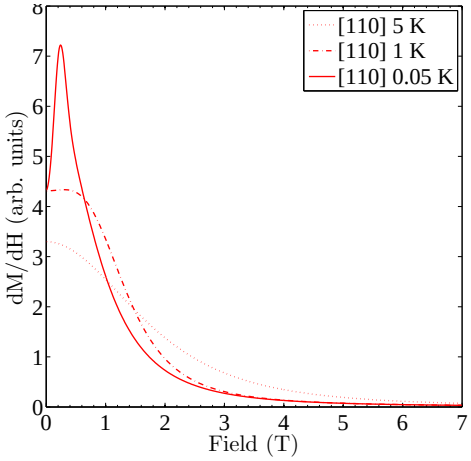

(b) Low field induced magnetic anomaly for Ba_2HoSbO_6

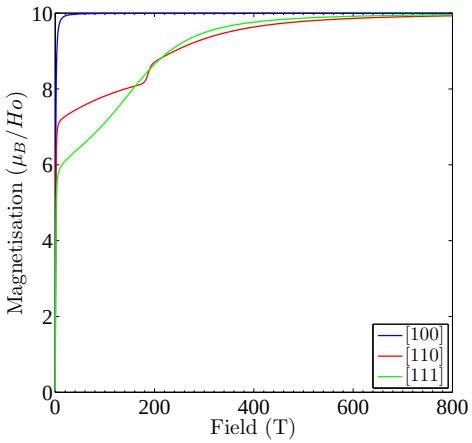

(c) Calculated magnetisation at 1 K for Ba_2HoSbO_6

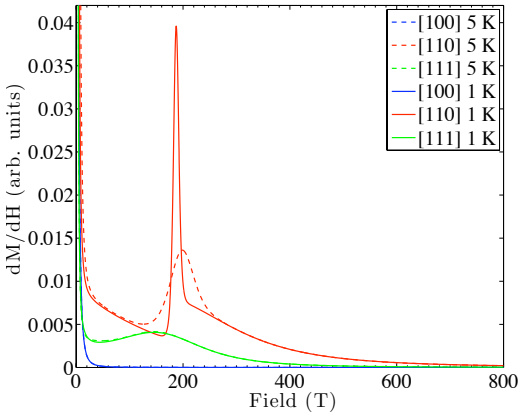

(d) High field induced magnetic anomaly for Ba_2HoSbO_6

Figure 3.27: [Ba_2HoSbO_6] (a) A peak below 1 T is observed in the calculated dM/dH plot for a field applied along the [100] and the [110] axis for Ba_2HoSbO_6. (b) A further anomaly occurs in the [110] direction around 200 T, this can be clearly seen as a step in (c) around that field. The [111] axis has a broad peak extending over several hundred Tesla which suggests no abrupt change in magnetic order. The magnetisation saturates in a fields of 30 T along the [100], however for the [110] and [111] axis fields of the order of 800 T are required.

along the $[111]$ direction there is a large hump which extends over several hundreds of Tesla which is not consistent to any abrupt crossover of energy levels. Instead some other mechanism seems to be present.

3.6.3 Calculation of specific heat for Ba_2HoSbO_6

The specific heat can be calculated from the CEF level scheme solved for Ba_2HoSbO_6. It was initially calculated using the two level Schottky specific heat and then a more rigourous calculation was carried out by a collaborator, C. Carboni of Sultan Qaboos University, Oman, which takes into account hyperfine interactions.

The two level Schottky specific heat is calculated by taking into account only the CEF energy level splitting of the GS and 1st excited states and their subsequent populations with temperature. It is given by:

$$C_{\text{Schottky}} = \frac{R\left(\frac{\Delta}{T}\right)^2 \frac{g_0}{g_1} \exp\left(\frac{\Delta}{T}\right)}{\left(1 + \frac{g_0}{g_1}\exp(\frac{\Delta}{T})\right)^2} \tag{3.16}$$

where C has units J/K mol f.u, Δ is the difference between the ground state and first excited state, R is the gas constant, g_0 is the degeneracy of the ground state and g_1 is the degeneracy of the first excited state. The resultant specific heat obtained using the values for the CEF level scheme of Ba_2HoSbO_6 is shown in figure 3.28. As this only considers transitions between the two lowest levels it only gives an approximate answer to the true specific heat, however the agreement is close to the more thorough calculation in this section and the experimental specific heat shown in section 3.6.4. This result again supports the claim that the magnetic effects are dominated by the non-magnetic GS and magnetic 1st excited CEF level.

A more rigorous method is to consider dipole interactions between the nuclear spin moment and magnetic field through the Zeeman term which lead to hyperfine splitting.

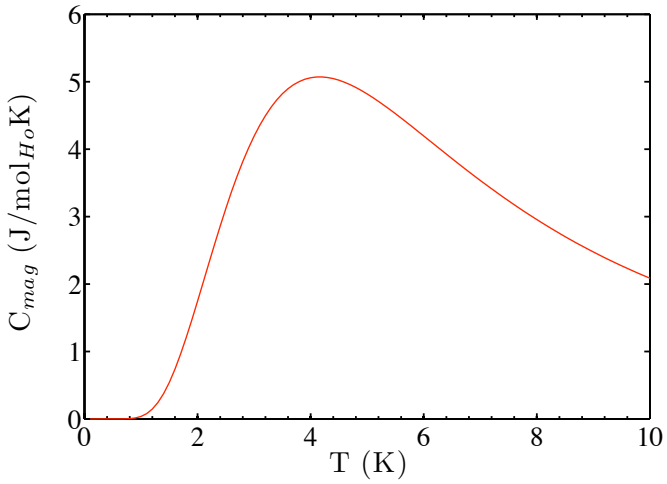

Figure 3.28: [Ba_2HoSbO_6] Specific heat calculated from the two level Schottky equation using the CEF level scheme solved for Ba_2HoSbO_6.

The eigenvalues of the Hamiltonian made up of crystal field and Zeeman terms are found. Then for each state the hyperfine splitting is calculated using:

$$a_t I_Z + P_t \left(I_Z^2 - \frac{1}{3} I(I+1) \right) \tag{3.17}$$

where I is the nuclear spin and P_t is a quadrupolar parameter. The extra ionic contribution a_t is the only factor included from the applied field. The hyperfine splitting is then added to each electronic state and the 136 energy levels are obtained. The temperature dependence of these energy level populations is constructed and the specific heat found through:

$$C = \frac{k_B}{(k_B T)^2} \left(\sum_i E_i^2 P_i - \left(\sum_i E_i P_i \right)^2 \right) \tag{3.18}$$

where P_i is the population of the state.

The results of this analysis in various applied fields are shown in figure 3.29. In the zero field result there is no evidence of any change to long range order; instead a broad curve implies the development of short range correlations below the Curie-Weiss temperature. What is striking is the change from zero field to applied field. In zero field

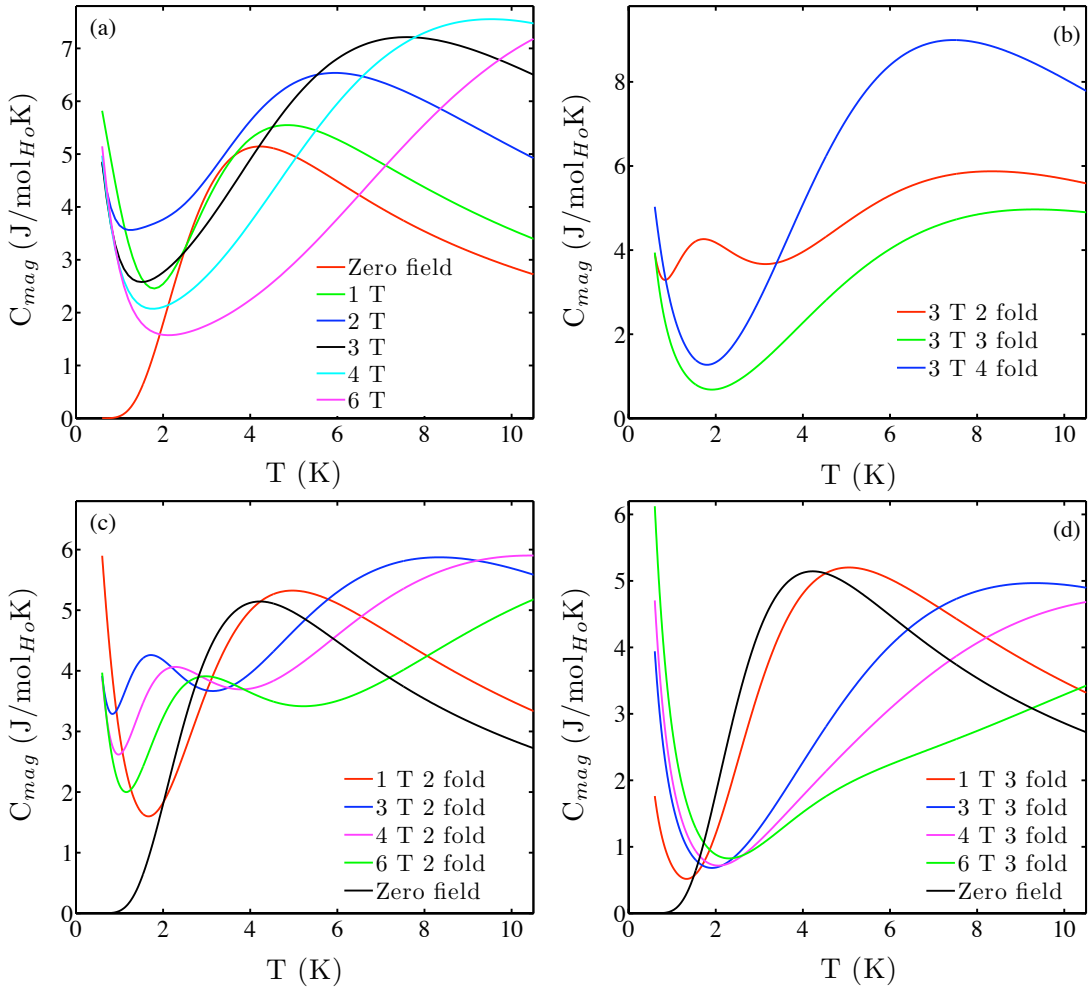

Figure 3.29: [Ba_2HoSbO_6] Specific heat for Ba_2HoSbO_6 calculated from crystal field parameters as described in the text. The average results give good agreement to experimental results, as shown in figure 3.31. A new peak is seen to develop when the field is applied along the 2 fold axis for fields above 3 T. The 3 fold results match closest to the actual experimental results.

there is no nuclear Schottky anomaly which is usually present in the specific heat results of holmium compounds [132]. This, however, fits into the proposed model of the ground state being non-magnetic meaning the nuclear levels do not feel any magnetic field. When a field is applied the system becomes magnetic causing the expected hyperfine interactions. The direction of the applied field gives different results. If the field is applied along the 2-fold axis an extra peak due to the first excited state appears between 2 and 4 T which is not observed for fields applied along the 3 or 4-fold.

3.6.4 Comparison of experimental and theoretical bulk properties

Bulk experimental measurements were carried out by X. Ke at Penn State University and are shown here in comparison with the theoretically determined results from the solved CEF.

Figure 3.30(a) shows the comparison of calculated (blue line) and experimental (red points) susceptibility results for Ba_2HoSbO_6. The results match closely with both having finite susceptibility as $T \rightarrow 0$ K. This only occurs for non-magnetic ground states in which there is no induced moment.

The comparison of calculated (blue line) and experimental (red points) magnetisation is shown in figure 3.30(b). A powder average was taken over all the possible directions of the crystal axis in the calculation. Again what is observed is a close agreement between experiment and theory giving more validity to the CEF level scheme calculated.

Figure 3.31 shows the (a) experimental and (b) calculated specific heat results. These results match closely and importantly behave the same in zero and applied field showing that the non-magnetic ground state is responsible for the lack of the Schottky anomaly observed experimentally.

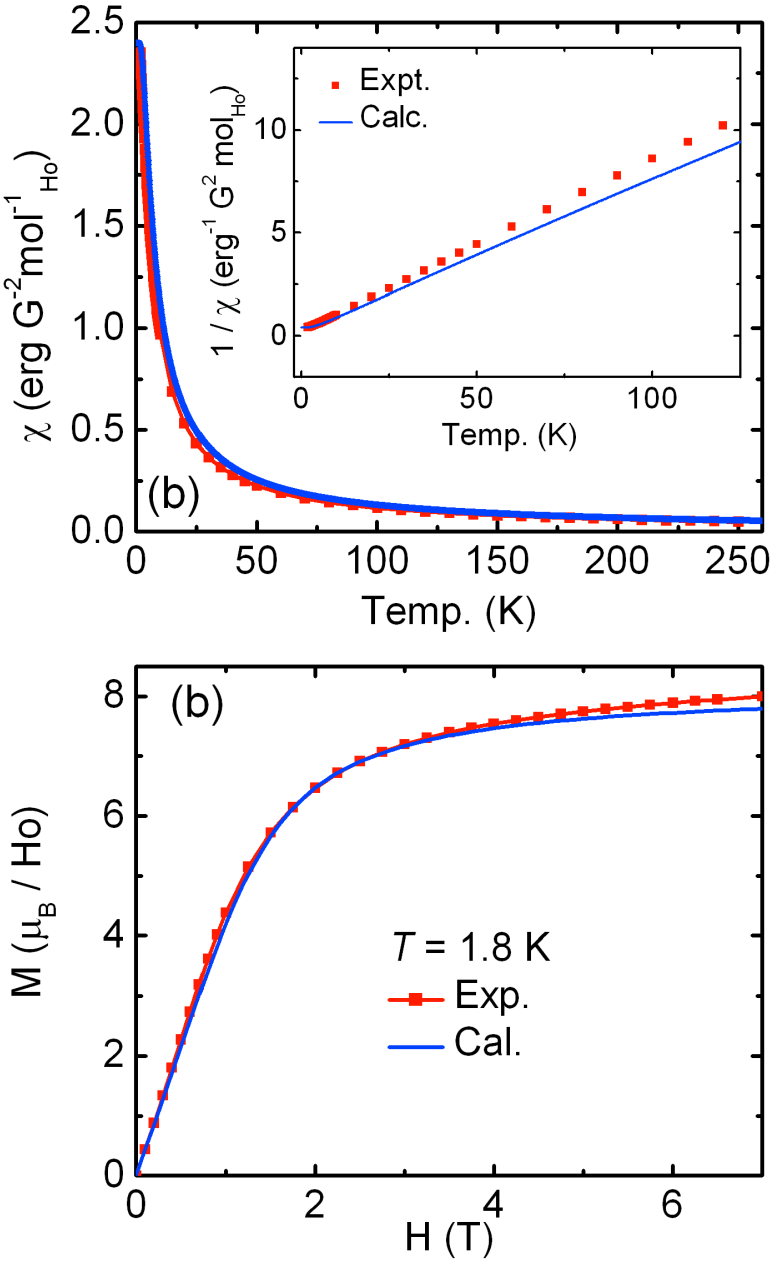

Figure 3.30: [Ba_2HoSbO_6] (a) DC magnetic susceptibility (M/H) as a function of temperature in a 100 Oe applied field (FC and ZFC results are identical); Inset shows the low temperature inverse DC susceptibility. (b) The magnetic field dependence of the magnetisation M at 1.8 K for Ba_2HoSbO_6. Red and blue curves represent experimental and calculated data, respectively.

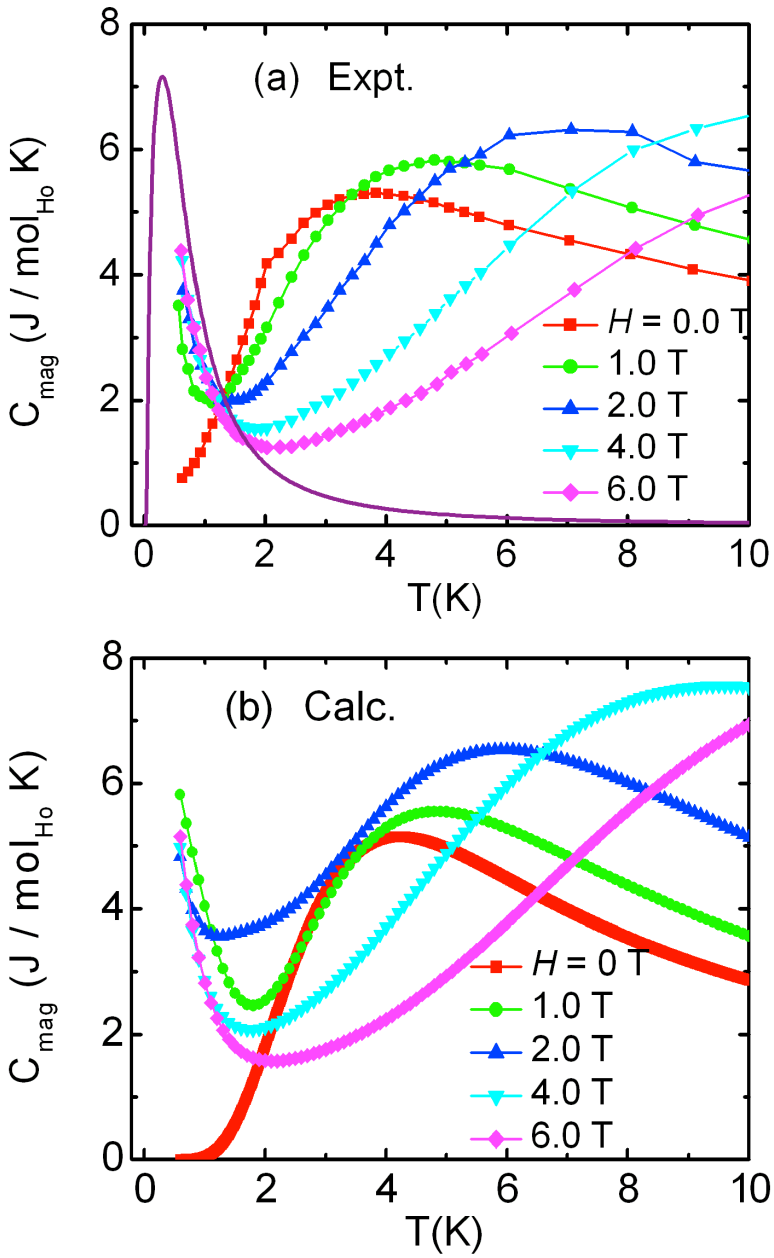

Figure 3.31: [Ba_2HoSbO_6] (a) Temperature dependence of heat capacity after phonon subtraction in different applied fields for Ba_2HoSbO_6 and (b) the corresponding calculated heat capacity data. The purple line in (a) represents the expected Schottky heat capacity value of holmium at this temperature for magnetic Ho^{3+}.

3.7 Properties of Ba_2ErSbO_6 obtained using crystal field parameters

Using the CEF parameters found for Er^{3+} in Ba_2ErSbO_6, and the same procedure as outlined above for Ba_2HoSbO_6, susceptibility, the magnetic moment and magnetisation are calculated.

3.7.1 Calculation of susceptibility for Ba_2ErSbO_6

The susceptibility for a 136.5(6) mg powder sample of Ba_2ErSbO_6 was measured experimentally using a Quantum Design Superconducting Quantum Interference Device (SQUID) magnetometer to recorded the dc-magnetisation in the temperature range 300 K to 1.7 K. Zero field cooled (ZFC) measurements were taken first by cooling to 1.7 K in zero field and then measuring the magnetisation as the sample is heated up to 300 K with a field of 1000 Oe applied. Field cooled (FC) results were obtained by cooling the sample back down to 1.7 K in a 1000 Oe field and then heating the sample up to 300 K recording the magnetisation. The field was then switched off. The results from the measurements are shown in figure 3.32.

The Van Vleck formula shown in equation 1.10 was used to calculated the susceptibility against temperature for Ba_2ErSbO_6 from the CEF parameters. The calculated susceptibility is compared to the measured susceptibility in figure 3.32. As can be seen the experimental and calculated results match closely. This gives confidence that the CEF level scheme predicted here for Er^{3+} in Ba_2ErSbO_6 is indeed correct.

The susceptibility clearly shows the difference between Ba_2HoSbO_6 and Ba_2ErSbO_6 CEF ground states. The inverse susceptibility for Ba_2ErSbO_6 goes to zero, unlike Ba_2HoSbO_6. This difference occurs since Ba_2ErSbO_6 has a magnetic GS while Ba_2HoSbO_6 has a non-magnetic GS. For Ba_2ErSbO_6 μ_{eff} has a constant value at 0 K, whereas μ_{eff}

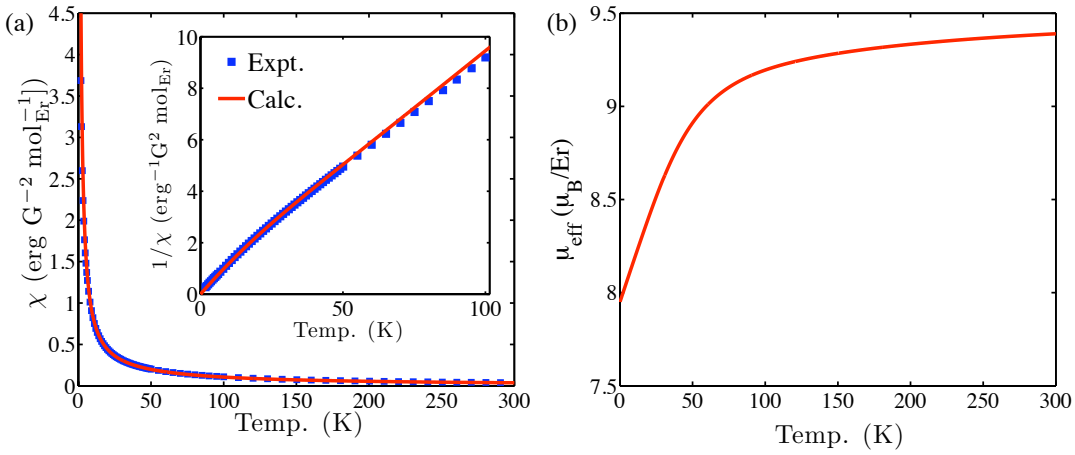

Figure 3.32: [Ba_2ErSbO_6] (a) Van Vleck susceptibility for Ba_2ErSbO_6 calculated from the crystal field parameters compared with SQUID results. (b) Effective moment calculated from the Van Vleck susceptibility. As opposed to Ho^{3+} in Ba_2HoSbO_6 the magnetic moment is not zero at 0 K due to Er^{3+} having a magnetic ground state.

for Ba_2HoSbO_6 goes to zero at 0 K.

The 4-fold degenerate ground state is separated by $\sim$150 K from the first excited state in the proposed CEF level scheme. This large energy gap will result in the ground state dominating the low temperature behaviour with only a small probability of transitions to excited CEF levels. The magnetic moment is given by $\mu_Z = g_J J_Z \mu_B$, where J_Z is given by $|\langle \Gamma_i | J_z | \Gamma_i \rangle|$. The 4-fold degenerate ground state is made up of two degenerate doublets which have magnetic moments $2.8\mu_B$ and $5.8\mu_B$.

3.7.2 Calculation of specific heat for Ba_2ErSbO_6

The specific heat was calculated using the two level Schottky equation (equation 3.16) and is shown in figure 3.33(a). The large difference in GS and 1st excited level means that this calculation must be looked upon with caution. The broad hump is centred at a much higher temperature compared with that of Ba_2HoSbO_6.

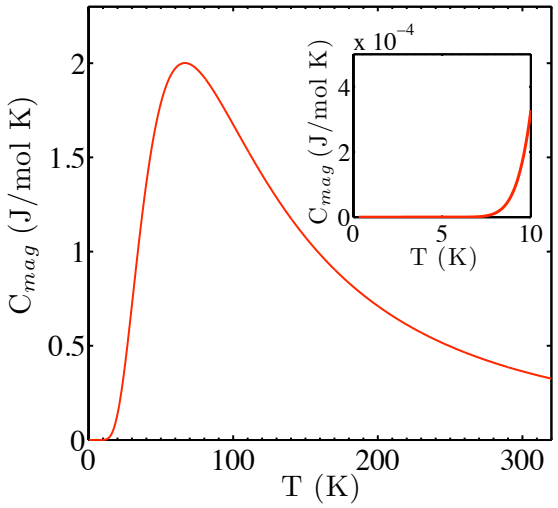

(a) Calculated specific heat

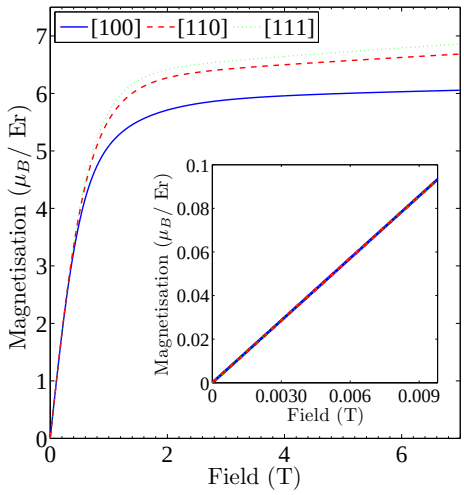

(b) magnetisation

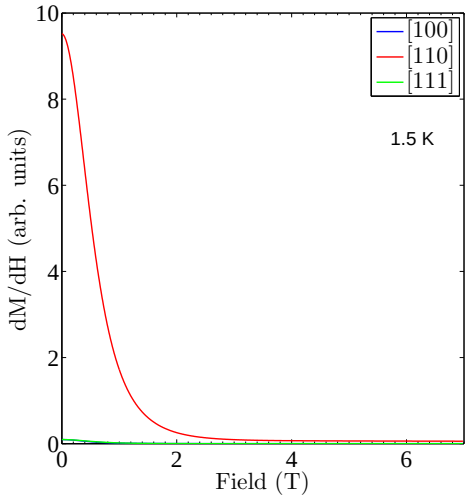

(c) Calculated dM/dH

Figure 3.33: [Ba_2ErSbO_6] (a) Specific heat calculated from the two level Schottky equation using the CEF level scheme. Calculated (b) magnetisation and (c) gradient of magnetisation with applied field at 1.5 K.

3.7.3 Calculation of magnetisation for Ba_2ErSbO_6

The applied field magnetisation was calculated in the same way as described in section 3.6.2 by including the Zeeman term in the Hamiltonian. The results for 1.5 K are shown in figure 3.33(b). The results are similar to that for Ba_2HoSbO_6 with a sharp increase around 1 to 2 Tesla and the magnetic moment not being saturated in fields up to 7 T. Plots of dM/dH are shown in figure 3.33(c). For Ba_2ErSbO_6 there is no anomaly associated with magnetic crossover or magnetic order.

3.8 Predictions for other members of the series from CEF results

It is possible to use CEF parameters from one particular ion to predict the CEF parameters and energy levels of a different ion. This is most effective for compounds with similar crystal structures. B_n^m was introduced in equation 3.6. In Stevens' notation it is given by:

$$B_n^m = A_n^m \langle r_n \rangle \Theta_n \tag{3.19}$$

B_n^m are the CEF parameters which have been determined experimentally above and is also the parameter for prediction in this consideration. Θ_n is the Stevens' multiplicative factors listed in Hutchings' review [113]. $\langle r_n \rangle$ is the radial integral and values are tabulated in ref. [133].

Rearranging equation 3.19 allows the value of A_n^m to be calculated:

$$A_n^m = \frac{B_n^m}{\langle r_n \rangle \Theta_n} \tag{3.20}$$

Inserting the values for Ho^{3+} in Ba_2HoSbO_6 and the values in refs. [113, 133] gives the expression for A_n^m for Ho^{3+} in Ba_2HoSbO_6. This value of A_n^m can be used to calcu-

late CEF parameters for another ion by substituting the calculated value for A_n^m and the relevant values from refs. [113, 133] for the new ion into equation 3.19.

Using the values for Ho^{3+} in Ba_2HoSbO_6 the predicted CEF parameters for Er^{3+} in Ba_2ErSbO_6 are $B_4 = 0.151 \times 10^{-2}$ meV and $B_6 = 0.239 \times 10^{-5}$ meV. This gives estimated energy levels at (in meV): 0 (4-fold degenerate), 9.63 (4-fold degenerate), 10.68 (2-fold degenerate), 47.47 (2-fold degenerate), 50.13 (4-fold degenerate). This is in qualitatively good agreement to the CEF level scheme found experimentally for Er^{3+} in Ba_2ErSbO_6, showing the usefulness of this method of estimating CEF parameters.

For Tb^{3+} in Ba_2TbSbO_6 the above method predicts $B_4 = 1.62 \times 10^{-2}$ meV and $B_6 = -1.84 \times 10^{-6}$ meV. This gives estimated energy levels at (in meV): 0 (non-magnetic singlet), 29.35 (magnetic triplet), 62.96 (magnetic triplet), 184.89 (non-magnetic singlet), 222.62 (magnetic doublet) and 234.79 (non-magnetic doublet). Therefore Ba_2TbSbO_6 is predicted to have a non-magnetic singlet ground state with two closely spaced magnetic triplets. This points towards similar properties to Ba_2HoSbO_6, but with the possibility of greater magnetic effects due to the increased number of magnetic levels close to the ground state. Rare earth ions with non-integer J values necessarily have only magnetic crystal field levels which could result in further interesting magnetic behaviour in other members of this series.

3.9 Summary of neutron and CEF results

Due to the ideal nature of the double perovskite, which has the magnetic ions in a cubic lattice on a site of cubic symmetry forming a *fcc* lattice, theoretical models can be applied and solved without approximation. The methods used here have been shown to agree well with experimental results obtained. The solved crystal field scheme for Ba_2HoSbO_6 has been shown to have a non-magnetic ground state. The small energy

gap between the non-magnetic GS and 1st excited magnetic state results in magnetic behaviour that can be predicted by the single ion model. Ba_2ErSbO_6 has a magnetic CEF ground state. No long or short range magnetic order is observed, however, and this can be explained by the agreement between theory and experiment for susceptibility. Thus the Er^{3+} ions behave as nearly perfect single ions with no interactions and as such do not form magnetic structures in zero field down to at least 60 mK.

Chapter 4

$LuCuGaO_4$: a spin-charge frustrated system

4.1 Characterisation of $LuCuGaO_4$

This chapter extends the investigations of potentially frustrated systems to include charge frustration in $LuCuGaO_4$. As an initial step magnetic susceptibility and neutron powder diffraction measurements were conducted to establish the basic quality of the powder sample to ensure fair comparison to previous studies in the literature.

4.1.1 Powder sample synthesis of $LuCuGaO_4$

The powder sample of $LuCuGaO_4$ was prepared by D. Parker at Oxford University [134]. The starting materials were Lu_2O_3, CuO and Ga_2O_3. CuO and Ga_2O_3 were pre-treated by heating in air for 24 hours at 900 and 1200 °C respectively. The starting materials were ground together, pelletized and heated in air at 1050 °C for a total of 120 hrs with 1 intermediate grinding. Approximately 19 grams of $LuCuGaO_4$ was produced.

4.1.2 Susceptibility results for $LuCuGaO_4$

A SQUID magnetometer was used to measure dc-magnetisation in the temperature range 300 K to 1.7 K as described in section 3.7.1 for the Ba_2ErSbO_6 powder sample.

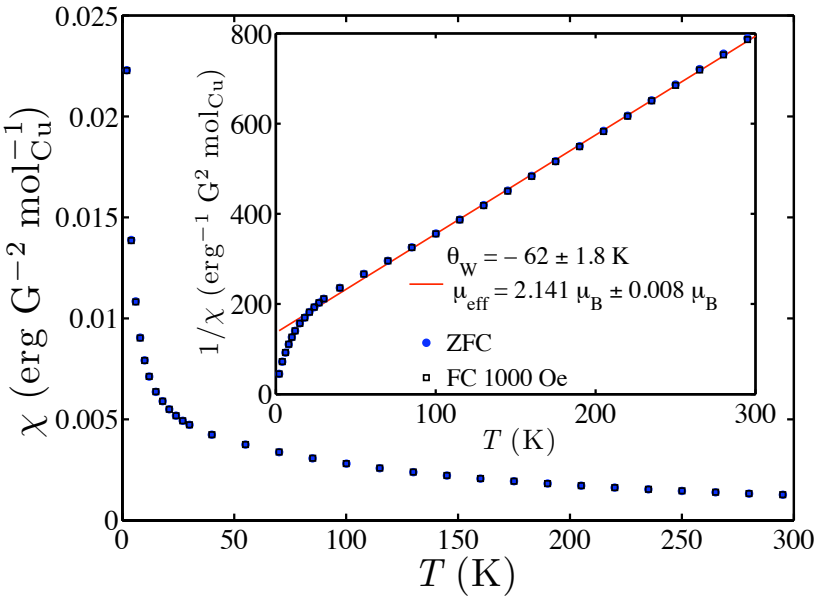

Figure 4.1: Susceptibility and (inset) inverse susceptibility for FC dc SQUID measurements at 1000 Oe for $LuCuGaO_4$. The solid line is a fit to the Curie-Wiess law between 200 and 60 K. ZFC results are identical to FC within experimental error.

A 160.93 $\pm$ 0.05 mg mass of $LuCuGaO_4$ was used. The results from the measurements are shown in figure 4.1.

There is no discernible splitting between FC and ZFC magnetization. The high temperature susceptibility data (300 to 150 K) can be fitted well to equation 1.9 for the Curie-Weiss law (solid line in figure 4.1) giving a magnetic moment per ion value of $2.141\mu_B \pm 0.008\mu_B$, close to the expected value for Cu^{2+} of $1.7\mu_B$ [135]. It should be noted that the slightly higher value of magnetic moment found here is not a result of experimental error, but an inherent overestimation in the technique of fitting susceptibility results to the Curie-Weiss law. Using $\mu_{eff} \equiv 2.827\sqrt{\chi_m T}$ (equation 1.8 in chapter 1) gives values of $1.73\mu_B \pm 0.06\mu_B$ at 295 K which fall off as the temperature is reduced. A negative Curie-Weiss temperature of $\theta_W = -62 \pm 1.8$ K indicates antiferromagnetic interactions. There is no suggestion of ordering or anomalies in the

susceptibility data down to 1.7 K. This suggests a highly frustrated sample. Using equation 1.13 in chapter 1 gives a "frustration index" of $f = -\frac{\theta_W}{T_c} > 42$. Any value over 10 would suggest a strongly frustrated sample [8] meaning $LuCuGaO_4$ is expected to be highly frustrated.There is deviation from the Curie-Weiss behaviour below $\sim$50 K which indicates an increase in correlations of spins. The susceptibility results found here agree well with those in the literature for $LuCuGaO_4$ [72].

4.1.3 Neutron scattering structural investigation on D1A at the ILL

The sample was characterized using neutron powder diffraction at the high resolution diffractometer D1A at the ILL with an incident wavelength of 1.91 Å. This instrument is described in section 2.2.4. Two temperatures were chosen: 70 K, since this lies well inside the paramagnetic regime and 1.5 K, which was the lowest available temperature with the instrumental arrangement.

The main aim of the characterisation was to test the powder sample produced against results published in the literature for $LuCuGaO_4$ in ref. [72] and confirm there is no structural change below the characterisation previously carried out at 11 K.

Previously the structure of $R Fe_2O_4$ (R = Y and Er) has been found using TOF neutron scattering [84]. Interestingly they state that the values of the thermal paramter U_{33} (the anisotropic thermal parameter along the c-axis) was unusually large for the R ion. They suggest this could be due to the rare earth ion's site being split along the c-axis since a high thermal parameter suggests an unstable atom site in GSAS [106].

In a later, apparently independent, structural characterisation of $LuCuGaO_4$ this idea was explored further in discussing diffraction results at 300 and 11 K [72]. The structural characterisation in ref. [72] considered three different models (M1, M2 and M3) concerned with the position of the rare earth ion, which is controlled by the bonding to

the bilayers of transition metals (see figure 1.6 in chapter 1):

- M1 has Lu^{3+} positioned in the standard $(0, 0, 0)$ coordinate. It was found in this model that the isotropic thermal parameter for Lu^{3+} was anomalously large.
- M2 allows the Lu^{3+} ion to move freely in an anisotropic way along the a, b and c-axis. There was an improved χ^2 in the results reported in ref. [72] . The thermal parameter, however, for Lu^{3+}, in the c-axis was found to be anomalously large compared to the a or b-axis.
- M3 has the Lu^{3+} ion shifted to the new, well defined, position $(0, 0, z)$. This had a similar χ^2 to M2 in their results but with low values for the thermal parameters indicating the ions are at stable positions.

A similar treatment of the diffraction results to ref. [72] was carried out on the experimental results obtained here from D1A using the refinement programme GSAS. A comparison of the results are shown in tables 4.1 and 4.2. The experimental scattering results at 1.5 and 70 K and their corresponding fits to the M3 model are shown in figure 4.2.

As can be seen in tables 4.1 and 4.2 the thermal parameters, denoted by U, are anomalously high for Lu^{3+} in all but M3. The refinement analysis carried out here agrees with the previously published results in which M1 and M2 are unstable and M3 is the correct structure. These results therefore extend the validity of the model down to 1.5 K. It also shows that the powder sample in ref. [72] behaves the same as the powder sample produced for this work. This means that the low temperature ac-susceptibility and specific heat results in ref. [72] can be confidently used in this discussion of $LuCuGaO_4$.

Further information can be gained from the diffraction results. Figure 4.2 shows that all the Bragg peaks at 1.5 K and 70 K are indexed by the single phase model of

			M1	M2	M3
		a (Å)	3.4390(4)	3.4390(4)	3.4390(4)
		b (Å)	3.4390(4)	3.4390(4)	3.4390(4)
		c (Å)	24.323(5)	24.323(5)	24.323(5)
Lu	$3a$	U_{iso} (Å^2)	0.014(2)		
		$U_{11} = U_{22}$ (Å^2)		0.00044(5)	
		U_{33} (Å^2)		0.055(2)	
		U_{12} (Å^2)		0.0002(2)	
	$6c$	z			0.009(1)
		n			0.5
		U_{iso} (Å^2)			0.0008(4)
Cu/Ga	$6c$	z	0.213(4)	0.213(5)	0.213(4)
		U_{iso} (Å^2)	0.005(1)		0.0043(3)
		$U_{11} = U_{22}$ (Å^2)		0.0044(2)	
		U_{33} (Å^2)		0.0033(3)	
		U_{12} (Å^2)		0.0022(1)	
O1	$6c$	z	0.291(3)	0.291(2)	0.291(3)
		U_{iso} (Å^2)	0.009(4)		0.010(2)
		$U_{11} = U_{22}$ (Å^2)		0.010(5)	
		U_{33} (Å^2)		0.008(4)	
		U_{12} (Å^2)		0.005(2)	
O2	$6c$	z	0.128(4)	0.125(7)	0.125(7)
		U_{iso} (Å^2)	0.025(1)		0.024(5)
		$U_{11} = U_{22}$ (Å^2)		0.021(5)	
		U_{33} (Å^2)		0.032(2)	
		U_{12} (Å^2)		0.010(5)	
		$R_{wp}(\%)$	3.48	3.42	3.43
		χ^2	9.047	8.761	8.839

Table 4.1: Parameters from GSAS refinement at 1.5 K for $LuCuGaO_4$. M1 represents the Lu^{3+} ion having an isotropic thermal parameter, M2 allows Lu^{3+} to vary in an anisotropic manner along the a, b, c axis and M3 has Lu^{3+} positioned on a well defined point $(0, 0, z)$.

			M1	M2	M3
		a (Å)	3.4401(2)	3.4401(2)	3.4401(2)
		b (Å)	3.4401(2)	3.4401(2)	3.4401(2)
		c (Å)	24.321(3)	24.321(2)	24.321(3)
Lu	$3a$	U_{iso} (Å^2)	0.013(3)		
		$U_{11} = U_{22}$ (Å^2)		0.00044(2)	
		U_{33} (Å^2)		0.055(3)	
		U_{12} (Å^2)		0.0004(5)	
	$6c$	z			0.009(1)
		n			0.5
		U_{iso} (Å^2)			0.0006(1)
Cu/Ga	$6c$	z	0.213(3)	0.213(9)	0.213(4)
		U_{iso} (Å^2)	0.004(1)		0.005(2)
		$U_{11} = U_{22}$ (Å^2)		0.0043(5)	
		U_{33} (Å^2)		0.0057(3)	
		U_{12} (Å^2)		0.0021(7)	
O1	$6c$	z	0.297(3)	0.291(2)	0.291(3)
		U_{iso} (Å^2)	0.018(4)		0.0086(3)
		$U_{11} = U_{22}$ (Å^2)		0.010(4)	
		U_{33} (Å^2)		0.0064(3)	
		U_{12} (Å^2)		0.0053(3)	
O2	$6c$	z	0.102(1)	0.128(4)	0.128(3)
		U_{iso} (Å^2)	0.133(3)		0.024(5)
		$U_{11} = U_{22}$ (Å^2)		0.021(1)	
		U_{33} (Å^2)		0.031(3)	
		U_{12} (Å^2)		0.010(2)	
		$R_{wp}(\%)$	3.73	3.52	3.70
		χ^2	8.682	7.723	8.537

Table 4.2: Parameters from GSAS refinement at 70 K for $LuCuGaO_4$. M1 represents the Lu^{3+} ion having an isotropic thermal parameter, M2 allows Lu^{3+} to vary in an anisotropic manner along the a, b, c axis and M3 has Lu^{3+} positioned on a well defined point $(0, 0, z)$.

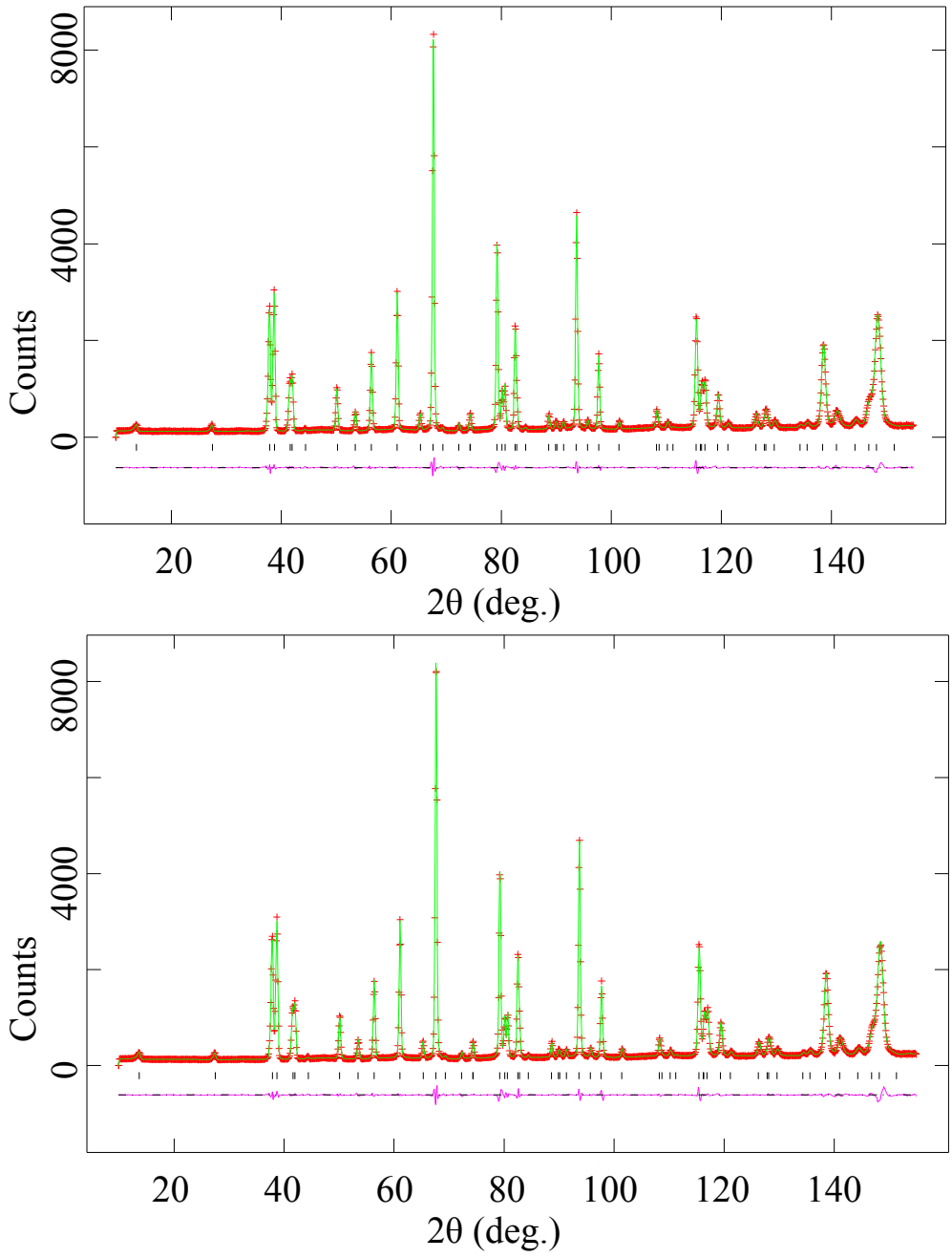

Figure 4.2: Neutron powder diffraction at (top) 1.5 K and (bottom) 70 K from D1A at the ILL. The fits were obtained using the rietveld refinement program GSAS for M3 which has Lu^{3+} at a well defined position $(0, 0, z)$.

$LuCuGaO_4$ showing that there is no impurity phase evident in the high resolution neutron scattering results. Another point is that there is no evidence of additional peaks between 70 and 1.5 K indicating that there is no long or short range ordering of spins evident in these results. This will be investigated further below with different experimental techniques. A higher background was observed at 70 K compared to 1.5 K, which can be explained by increased thermal scattering. There was also no indication of structural changes between these two temperatures. The diffraction results show that $LuCuGaO_4$ remains in the $R\bar{3}m$ structure between ambient temperature and at least 1.5 K.

4.2 Low temperature results for $LuCuGaO_4$

4.2.1 An xyz polarized neutron analysis

An xyz polarised neutron analysis was performed on D7 at the ILL at a wavelength of 4.8 Å at 50 K, 5 K, 0.5 K and 80 mK. The mass of the sample used was 18.61 $\pm$ 0.03 g. This instrument is described in section 2.2.5.

The temperatures were selected to compare the paramagnetic regime (50 K), with the regime in which correlations are appearing and the inverse susceptibility becomes non-linear (5 K) , and the low temperature regime below the previously predicted spin glass transition from anomalies in the susceptibility and specific heat results in the literature around 0.4 K in ref. [72].

Figure 4.3(a) and 4.3(b) show the separated nuclear and magnetic scattering. The nuclear component shows a change in intensity between high temperature (50 K) and low temperature (0.08 K to 5 K) which can be attributed to higher thermal scattering at high temperature. From susceptibility and specific heat results for $LuCuGaO_4$ there is a predicted spin glass transition around 0.4 K in ref. [72]. The low temperature mag-

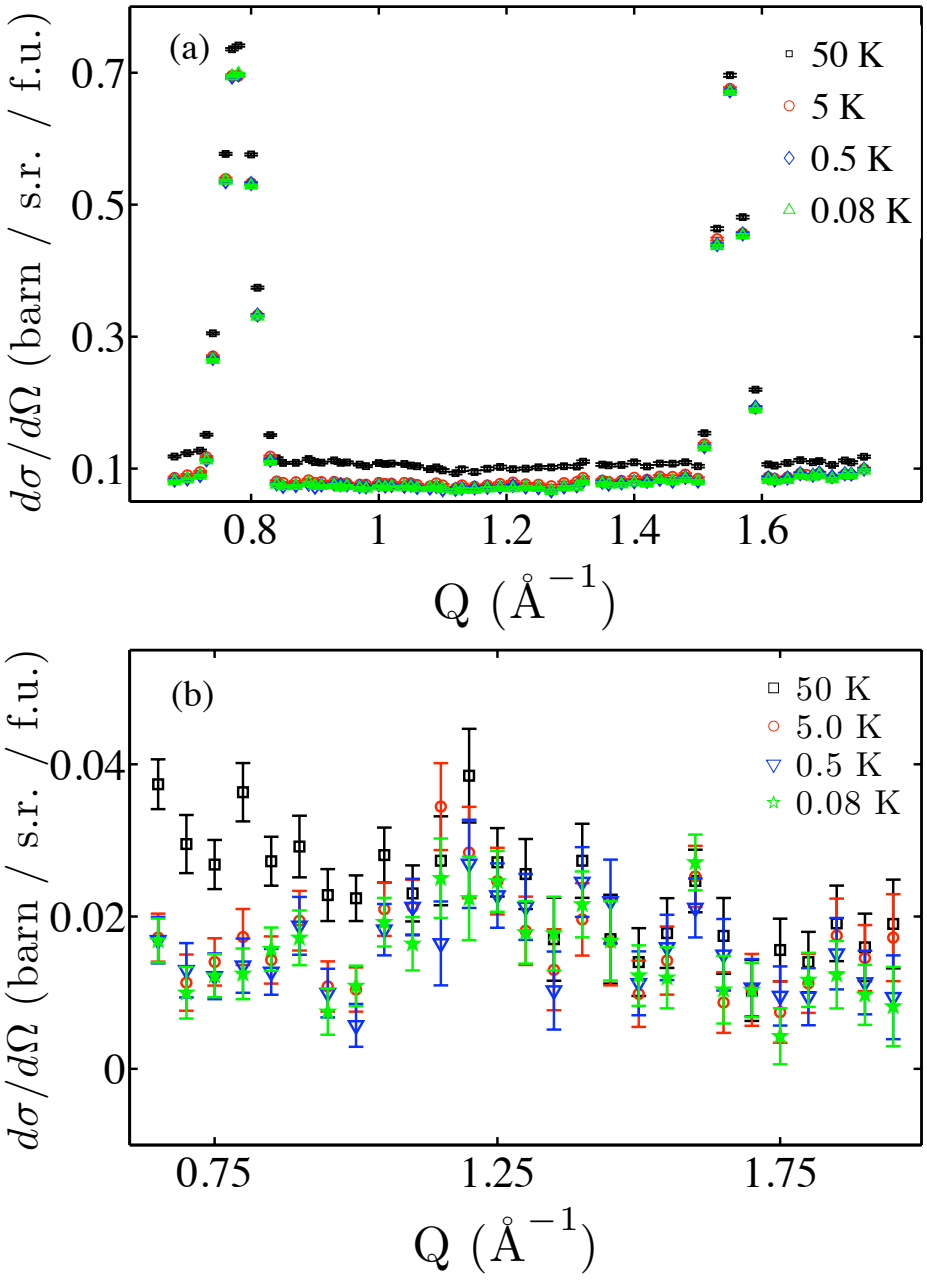

Figure 4.3: Polarized neutron scattering from D7 at the ILL on a $LuCuGaO_4$ powder sample. The results are separated (a) nuclear and (b) magnetic components.

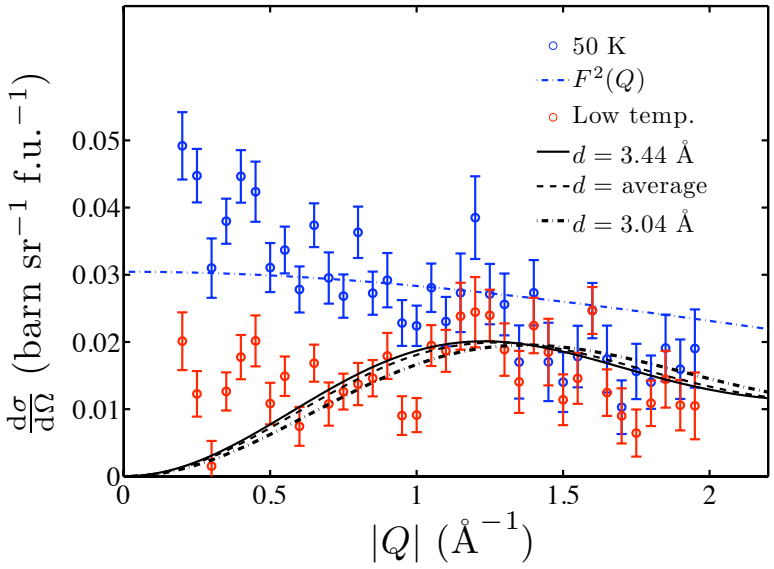

Figure 4.4: Separated magnetic component from polarized neutron analysis on D7 at the ILL. The combined low temperature results (0.08 to 5 K) fit well to nn AFM correlations (equation) for either the nn in plane ($d = 3.44$ Å), nn between layers ($d = 3.04$ Å) or a weighted average of both. The results at 50 K are in the paramagnetic regime and fit well to the form factor ($F^2(Q)$) for Cu^{2+}.

netic data above and below this temperature show no evidence of this with no change observed through the transition temperature. There is, however, a clear change in magnetic scattering between 50 K and low temperature.

Starting from empirical analytical formulas and using relevant coefficients [111] the magnetic form factor for Cu^{2+} [111] was produced and a least squares analysis was used to fit this to the neutron results for the magnetic component. The high temperature data fits well to the expected form factor behaviour for Cu^{2+}, therefore confirming it to be in the paramagnetic regime, as shown in figure 4.4(b). This is not the case for the low temperature data. A broad bump centred around $\sim$1.25 Å^{-1} in Q is observed. Interestingly this corresponds to a peak observed in the initial structural determination of ref. [72] which occurred around 18° for a wavelength of 1.5396(1) Å (corresponding to $\sim$1.27 Å^{-1} in Q) for $LuCuFeO_4$, $LuZnFeO_4$ and $LuCoGaO_4$ and also in a separate

study on the related compound $LuFeMgO_4$ [77].

A similar peak has been observed on the $S = \frac{1}{2}$ kagomé antiferromagnetic herbertsmithite $ZnCu_3(OH)_6Cl_2$ [136]. This peak was fit to the structure factor for disordered near-neighbour AF dimers or spin-singlet correlations, given by:

$$I(Q) \propto F^2(Q) \left(1 - \frac{\sin(Qd)}{Qd}\right) \tag{4.1}$$

where $F^2(Q)$ is the form factor and d the distance between the AFM correlated ions. A fit was obtained as shown in figure 4.4(a). Two values of the Cu-Cu distance were used: 3.44 Å, which corresponds exactly to the nearest neighbour distance between Cu-Cu (or Cu-Ga etc) in the triangular layers, and 3.04 Å, which is the nn Cu-Cu distance between the layers. These values were found here from the structural characterisation and in agreement with the literature [72]. A weighted average was also used. The results are shown in figure 4.4. A good fit with no appreciable difference between the two nn distances is found. The low temperature results provide strong evidence that the Cu^{2+} ions have AFM nn magnetic correlations in $LuCuGaO_4$. This would explain the deviation below 50 K from Curie-Weiss behaviour observed in the susceptibility results reflecting a build up of these correlations.

An alternative expression (equation 1.15 in chapter 1) was used to reproduce the similar magnetic peak observed in $LuFeMgO_4$ by Wiedenmann et al. [77]. The equation describes the neutron scattering cross-section and allows each shell of nearest neighbours to be built up. Results of this process are shown in figure 4.5. The distances are as follows: r1 = 3.04 Å; r2 = 3.44 Å; r3 = 4.59 Å; r4 = 5.74 Å and r5 = 5.958 Å. r1, r3 and r4 are Cu^{2+} near neighbour distances between the triangular layers, r2 and r5 are near neighbour distances within the same triangular layer. Figure 4.5 shows that extending beyond the nearest neighbour distance in the plane (r2) and between the planes (r1) to

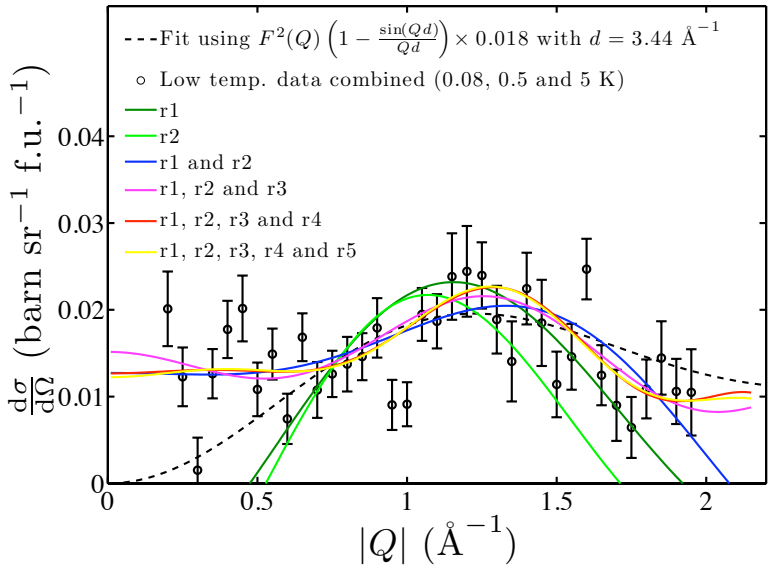

Figure 4.5: Various fits using equation 4.1 for near neighbour correlations to the magnetic component of scattering from D7 for $LuCuGaO_4$. r1 represents the first near neighbour shell. r2 the second near neighbour, etc.

next nearest neighbours does not result in a significantly better fit to the experimental data. The fit to the AFM near neighbour correlations from equation 4.1 is also shown and this is seen to give appreciably the same fit as equation 1.15.

There is no sign of this broad peak in the D1A data, however this will be due to instrumental parameters making the low angle scattering not as evident. Interestingly there is no mention of any evidence of a peak in the earlier study of $LuCuGaO_4$ [72]. This suggests that $LuCuGaO_4$ has the least pronounced magnetic interactions out of the compounds $LuZnFeO_4$, $LuCoGaO_4$, $YbCuGaO_4$, $LuCuFeO_4$ and $LuCuGaO_4$ investigated by ref. [72]. The observation of the peak in the magnetic scattering component of xyz polarised neutron analysis unambiguously attributes this to magnetic correlations within the sample.

These neutron scattering results, however, do not clarify the cause of the anomaly around 0.4 K in the susceptibility and specific heat results reported in ref. [72]. This

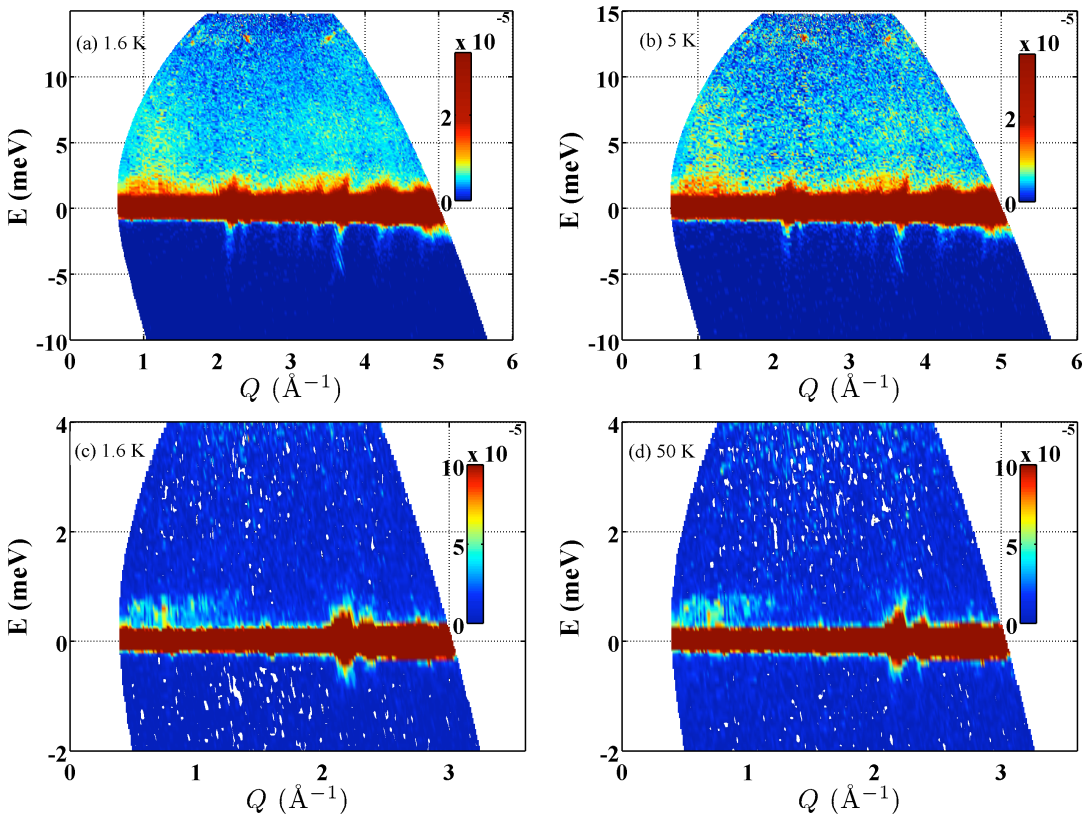

Figure 4.6: Inelastic neutron scattering on IN4 at the ILL for (a) 1.6 K and 17 meV incident energy (b) 5 K and 17 meV incident energy (c) 1.6 K and 6.3 meV incident energy and (d) 50 K and 6.3 meV incident energy. An area of high intensity scattering is observed around $Q \approx 1.25$ Å^{-1} which corresponds to the magnetic scattering observed from the polarized neutron analysis on D7. The results for 6.3 meV are effected by the nuclear scattering from the Bragg peak at 0.8 Å^{-1}.

is also a feature of $LuMgFeO_4$ where no change in the neutron scattering intensity is observed across the susceptibility cusp [78, 85].

4.2.2 IN4 measurements at the ILL

As a further step to investigate the magnetic behaviour that occurs in $LuCuGaO_4$ inelastic neutron scattering measurements were performed on IN4 at the ILL for temperatures of 1.6, 5 and 50 K using incident energies of 6.3 and 17 meV. The instrument is de-

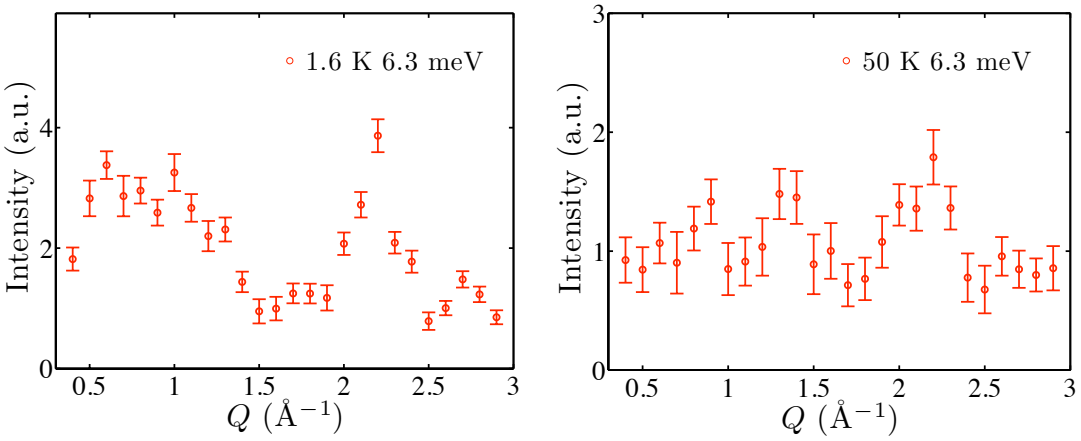

Figure 4.7: Constant energy cuts of the IN4 $LuCuGaO_4$ data. For 6.3 meV incident energy measurement the overlap of nuclear Bragg peaks from elastic scattering does not allow a fit to be obtained. The 50 K result also does not fit the scattering function, confirming previous results showing no magnetic correlations at 50 K.

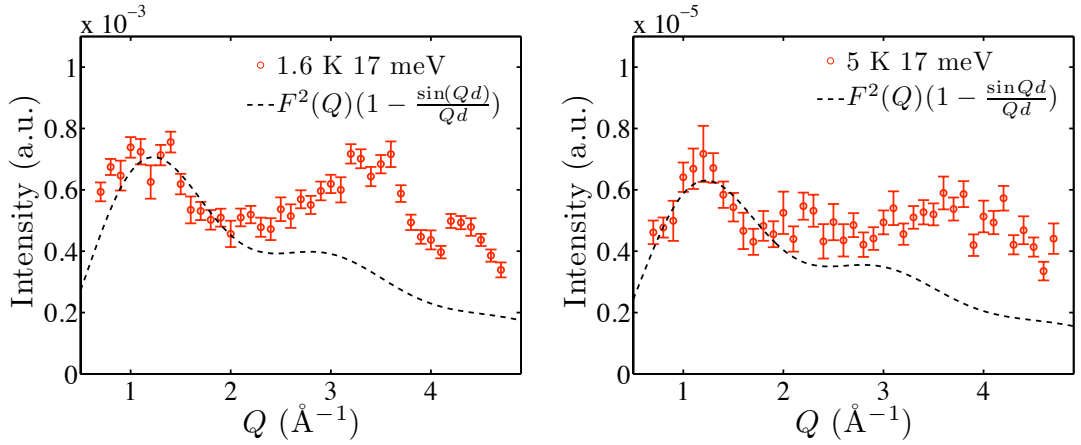

Figure 4.8: Constant energy cuts of the IN4 $LuCuGaO_4$ data. The results are fitted to a nearest neighbour AFM scattering function. The peak around $Q \approx 1.25$ Å^{-1} can be seen to fit well to this model for the 17 meV incident energy results.

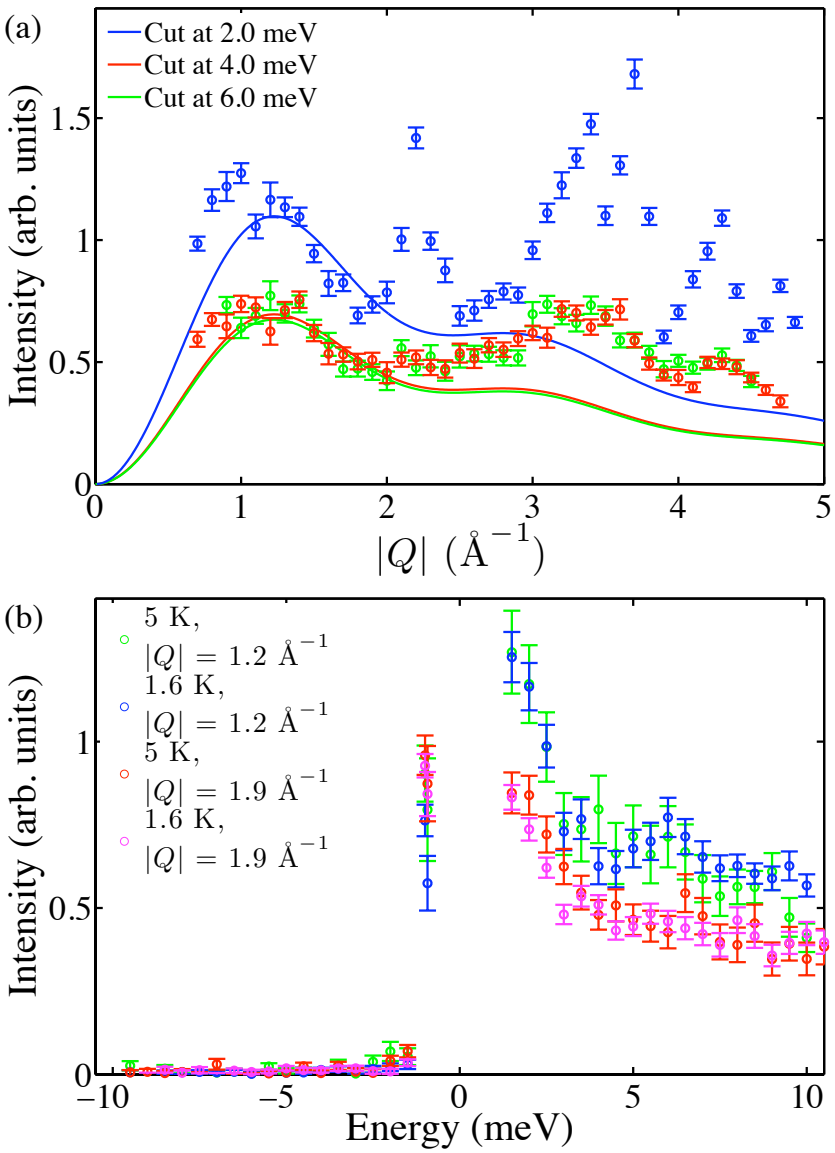

Figure 4.9: (a) Constant energy cuts for 1.6 K and incident energy of 17 meV. The energy of the cut is shown. It can be seen that the peak at $\sim$1.25 Å^{-1} can be fitted between 2 meV and 6 meV. (b) Constant Q cuts at $Q = 1.2$ Å^{-1} and 1.9 Å^{-1} for 5 and 1.6 K.

scribed in section 2.2.3. The results are shown in figure 4.6 for energies of 6.3 and 17 meV.

Constant energy cuts are shown for the four different energies and temperatures in figures 4.7 and 4.8. The results for an incident energy of 6.3 meV have to be interpreted carefully since there is a nuclear peak at 0.8 Å^{-1}. This is seen to mix with the magnetic scattering around 1.25 Å^{-1} and create a large peak with its centre shifted. The results obtained whilst using 17 meV incident energy are much more informative since the energy cuts can be taken far enough away from the elastic and quasi-elastic scattering to negate its effect. The constant energy cuts show a peak around 1.25 Å^{-1} which can be fitted to nearest neighbour AFM interactions used to fit the magnetic peak in the D7 results (equation 4.1). Fits to the peaks using the model discussed are shown for different energy cuts in figure 4.9(a). The results show that for $LuCuGaO_4$ the region of $0.75 < Q < 1.75$ from energies of 0 meV to at least 6 meV constitutes magnetic scattering that is due to nn AFM correlations of Cu^{2+}. There is an increase in phonon scattering at higher Q observed in the plots.

Constant Q plots are shown in figure 4.9(b). There is no indication of a "gap" in energy in Q. This means that the agreement found in the neutron scattering to equation 4.1 can only be considered to be due to the fact that there is nn AFM correlations and not to the interpretation that there are dimers formed on the bilayers. If there were dimers there would be the expectation that there would be an energy gap in the constant Q cuts due to singlet-triplet formation of the spin $\frac{1}{2}$ Cu^{2+} ions.

These INS results, however, do not clarify the behaviour occurring between 50 K and 5 K. The 50 K results were only taken at energies 6.3 meV which is affected by nuclear peaks and therefore cannot give conclusive results. It would have been more informative to gain 50 K and intermediate temperature results at 17 meV, however time

constraints and instrumental parameters did not allow for this to be achieved.

4.2.3 μSR investigations

The spin interactions in $LuCuGaO_4$ were probed using μSR. A longitudinal applied field and zero field study was conducted using the MuSR instrument at the ISIS pulsed muon source from 50 K down to 60 mK in fields up to 0.2 T. This instrument is described in section 2.3.5. μSR gives a picture of local susceptibility which cannot be obtained from standard neutron techniques.

The field dependence was used to determine the most appropriate function to fit to the zero field temperature dependence. μSR is sensitive to magnetic fluctuations with nuclear and electronic origins on a timescale of 10^{-5} to 10^{-7} seconds. In a paramagnet the electronic fluctuations are mostly very rapid and lie outside the window of the μSR experiment, while the nuclear component can be decoupled using a small applied field of $\sim$10 G. This is shown in figure 4.10(a), where at 50 K the depolarization rate falls rapidly and is independent of field above 10 G. At lower temperatures the field dependence is modified, with fields of up to 100 G required to decouple the fluctuations. This indicates that at low temperature there is an increasing electronic contribution, i.e. that magnetic fluctuations are slowing and falling into the muon time window as the temperature decreases.

Examples of the zero field muon polarization decay for different temperatures are shown in the inset of 4.10(b). The asymmetry between 50 K and 5 K remains the same, showing the local environment of the spin structure is unchanged. The asymmetry drop-off rate increases as the temperature is lowered indicating a change in the local magnetic structure.

To gain further information the μSR spectra, using the muon data analysis pro-

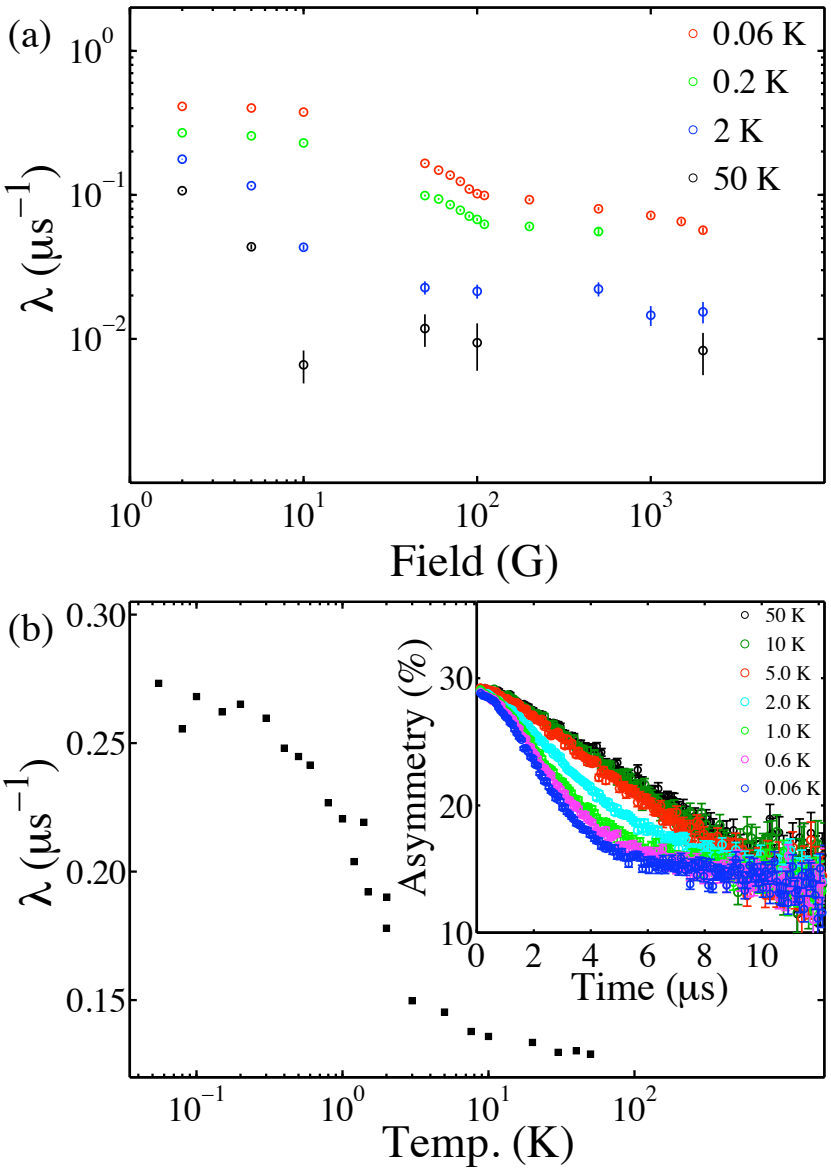

Figure 4.10: μSR results for $LuCuGaO_4$ taken on MuSR at ISIS in applied field and zero field. (a) The muon depolarization rate, λ, as a function of applied field. At high temperature electronic fluctuations are rapid. Nuclear fluctuations can be decoupled with a small field of 10 G. At low temperature, the increasing importance of electronic fluctuations means stronger fields are required to decouple the muon response, i.e. to achieve field independence. (b) (inset) Variation of depolarization with time and fits to the data using a stretched exponential and Kubo-Toyabe showing the changing dynamics with temperature.

gram Wimda [137], were fit to a combination of two equations: one fitting the nuclear and the other fitting the electronic component. The temperature independent nuclear component was modelled using the static Kubo-Toyabe equation: $1/3 + 2/3(1 - (\gamma_\mu \Delta t)^2) \exp(-1/2(\gamma_\mu \Delta t)^2)$. A stretched exponential of the type $\exp(-(\lambda t)^\beta)$ was used to model the temperature dependent electronic component. β is a constant to model the electrons' response. The muon relaxation rate λ is related to the relaxation time and distribution of the local magnetic field probed by the muons and is found from the fits.

The value of λ for each temperature measured in ZF is shown in figure 4.10(b). This shows a relatively flat feature as the temperature goes from 50 K to 5 K. Then the depolarization rate increases until it plateaus off around the previously reported spin glass transition temperature of $\sim$0.4 K.

μSR allows a clear distinction between spin glass behaviour or otherwise. Canonical spin glasses such as AgMn(0.5 at. $\%$) have been extensively investigated by μSR [138]. The combination of geometric frustration and quenched random disorder in AgMn causes the spins to freeze at the glass transition temperature, T_g, resulting in a distribution of static fields. The depolarization rate increases as the system approaches T_g but then falls rapidly as the field distribution becomes static and the precessing muons are not so rapidly dephased. Evidently the behaviour of the relaxation rate in $LuCuGaO_4$ is completely different. Instead it matches that of a spin liquid, as will be considered.

4.3 Discussion of $LuCuGaO_4$ results

From the experimental investigations above the conclusion proposed is that $LuCuGaO_4$ is a spin liquid, rather than the previously proposed spin glass. There are numerous definitions of a spin liquid, but the one used here is by Fåk et al. who used the analogy with an actual liquid in which a spin liquid is a system with short ranged, dynamic

correlations [139]. Referring to the experimental results evidence for this conclusion will be presented firstly from the structural disorder of the cations and secondly the liquid like dynamics.

4.3.1 Arrangement of cations in the triangular layers

In all previous studies of $RMM'O_4$ the arrangement of the cations has been treated as disordered. However, although the ordering of two different cation species on the triangular bilayer is frustrated, a completely random distribution seems unlikely since triangles containing entirely Cu^{2+} or Ga^{3+} will incur a Coulombic cost. Thus the possibility that the Cu/Ga ions are correlated was considered.

The scattering lengths of the cations are close ($b_{\mathrm{Cu}} = 7.718$ and $b_{\mathrm{Ga}} = 7.288$). This prohibits the direct detection of long or short range order of the Cu/Ga ions from the neutron results presented in this chapter.

There is, however, less direct evidence of the cation arrangement. As has been shown in section 4.1.3 Lu^{3+} sits at a well defined, but shifted position, above or below the bilayers. Each Lu^{3+} sits above (or below) the centre of two triangles formed from Cu/Ga (M/M') in the bilayers. The position of the Lu^{3+} ion is therefore expected to be controlled by the arrangement of the cations on the bilayer. At the nearest neighbour level there is a combination of six M and M' that make up the two triangles that a Lu ion is between. This implies seven possible positions of Lu in the z-direction. Excluding MMM or $M'M'M'$ on Coulombic grounds leaves just three positions. The zero displacement situation corresponds to $MMM' - MMM'$; however these also have a Coulombic cost compared to the $MMM' - MM'M'$ type and their exclusion leaves two well defined cation positions along z, as is found in section 4.1.3, rather than disorder causing the Lu^{3+} to centre at $z = 0$.

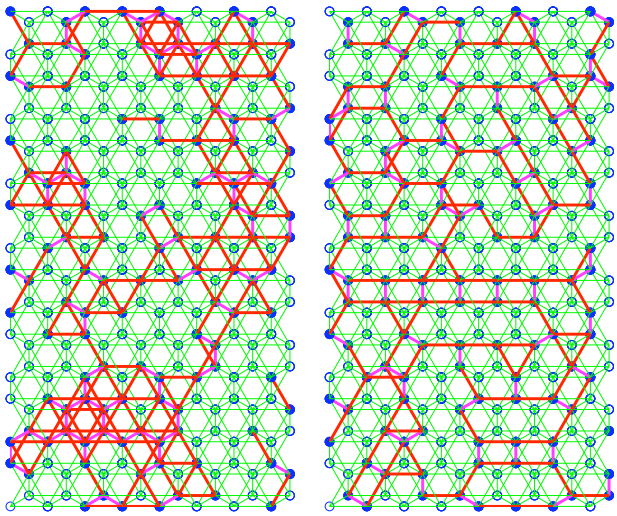

Figure 4.11: [Figure produced by T. Fennell] Examples of the types of network formed by (left) random cation configurations or (right) minimisation of near neighbour interactions. The random configuration can contain clusters of spins which are small or large with some isolated spins. The correlated configuration contains branching loops of spins, in which each spin typically has three nearest neighbours and no isolated spins.

T. Fennell at the ILL (formerly at UCL) collaborated with this experimental study of $LuCuGaO_4$ and produced figure 4.11 showing the arrangement of cations on the bilayers from a Monte Carlo simulation for (left) a disordered arrangement or (right) minimisation of near neighbour interactions. The two models produce distinctly different ordering of the cations. Random population of the cation sites leads to clusters of different sizes and an appreciable number of isolated spins, as discussed in section 1.5.2. Minimisation of near neighbour Coulombic frustration produces a network of branching loops with no isolated spins. The absence of a dominant orphan spin population would explain why there is no remnant form factor-like response in the diffuse magnetic scattering at low temperature: all the spins are involved in the magnetic groundstate.

Schiffer et al. reported results on geometric frustrated materials with a similar inverse susceptibility [140]. A phenomenological model was formed describing the sys-

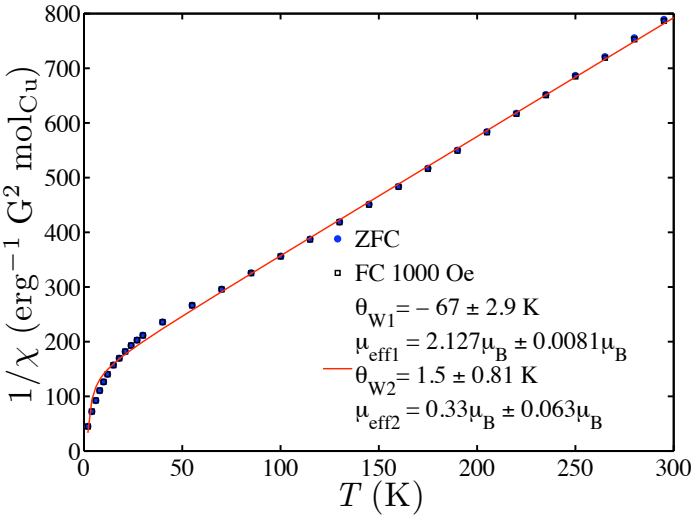

Figure 4.12: Inverse susceptibility measurements for $LuCuGaO_4$. Solid line shows a fit to the two population model (equation 4.2).

tem as having the majority of spins in a correlated form, but with some "orphan" spins remaining uncorrelated and essentially behaving as free spins. The susceptibility was found to follow the form:

$$\chi = \frac{C_1}{(T - \theta_{W1})} + \frac{C_2}{(T - \theta_{W2})} \tag{4.2}$$

where C_1 and C_2 are the Curie constants which depend on the size and fraction of the spins in the correlated and orphan populations. The constants θ_{W1} and θ_{W2} are the effective values of θ_W which reflect the exchange field for the spins in the correlated and orphan populations. The results of fitting equation 4.2 are shown in figure 4.12. The values obtained are: $\theta_{W1} = 67 \pm 2.9$ K, $\mu_{\mathrm{eff1}} = 2.127 \pm 0.0081\mu_{\mathrm{B}}$, $\theta_{W2} = 1.5 \pm 0.81$ K and $\mu_{\mathrm{eff2}} = 0.33 \pm 0.063\mu_{\mathrm{B}}$. The fact that the erro bars do not add up highlights that the model may be unfeasible for the susceptibility results for $LuCuGaO_4$. As in ref. [140] the close fit suggests that there are correlated near neighbour antiferromagnetic interactions responsible for the overall behaviour while the non-zero C_2 and θ_{W2} suggest that the orphan spins are subject to small, but non zero, effective exchange fields. The

presence of orphan spins supports the random ordering of cations. However, the need to include interactions could imply that there is not a dominant orphan population and be consistent with the ordering of cations resulting from minimisation of similar near neighbours.

Agreement with equation 4.2 was used as evidence to support spin liquid behaviour in ref. [140], however it was stressed that the simplicity of the model means it has to be applied carefully with each result treated as material specific and related evidence would be required to support the models claims. It has recently been proposed also that the downward curve in χ^{-1} is a general feature of many frustrated antiferromagnetic systems and as such not explained by orphan spins [141].

4.3.2 Magnetic correlations in $LuCuGaO_4$: spin liquid behaviour

The smooth deviation from Curie-Weiss behaviour below 50 K and simultaneous increase in muon depolarization rate, absence of FC/ZFC splitting in the temperature range from susceptibility results, and appearance of the peak in the magnetic diffuse scattering implies that the magnetic correlations build up gradually as the temperature decreases with no associated spin freezing. The depolarization rate of the muons from the μSR results increases steadily implying that the spins are entering a correlated but fluctuating state.

The μSR result is the strongest indication of a spin liquid state. Examining materials for a similar response leads to the Herbertsmithite compound $ZnCu_3(OD)_6Cl_2$ which is claimed to be a "structurally perfect S = 1/2 kagomé antiferromagnet" [16]. Detailed μSR investigations found a similar stretched exponential relaxation and increasing depolarisation rate at low temperature [142]. It was proposed as evidence for either a resonance valence bond (RVB) or cooperative paramagnetism in a spin liquid state.

Comparable neutron scattering responses are observed in several compounds. In particular $ZnCu_3(OD)_6Cl_2$ [136] and deuteronium jarosite, $(D_3O)Fe_3(SO_4)_2(OD)_6$, a kagomé antiferromagnet [139]. In each case a non-dispersive, gapless feature extends across all observed energies at the wavevector transfer characteristic of the near neighbour distance in question. In $ZnCu_3(OD)_6Cl_2$ the magnetic scattering can be fitted to the dimer structure factor (equation 4.1) at all available energies, and at all temperatures between 2 and 120 K. The scattering feature is attributed to a temperature and energy independent spectrum of near-neighbour antiferromagnetic dimers. In deuteronium jarosite there are short range dynamical correlations, as observed in $LuCuGaO_4$.

Essentially the same physics seems to exist in $LuCuGaO_4$ and Herbertsmithite. The results of the study of $LuCuGaO_4$, however, do not show the explicit existence of dimers, instead the agreement with the structure factor shows that a description of purely near neighbour antiferromagnetic correlations describes the magnetic behaviour. A comparable interpretation to Fåk et al. [139] who concluded that deuteronium jarosite shows short ranged correlations and liquid like dynamics describes the behaviour of $LuCuGaO_4$.

Chapter 5

Probing frustrated systems with an alternative μSR technique

μSR has been shown in chapter 5 to complement neutron scattering and bulk techniques, when applied to frustrated systems. What has also become evident is the need for careful interpretation due to the subtle and often competing interactions involved in magnetic systems at low temperature. In this chapter an alternative μSR technique is developed that gives more control over the interpretation of the μSR experiment. The experimental work was carried out by S. T. Bramwell (STB) and S. R. Giblin (SRG). I carried out the numerical analysis.

5.1 "Far field" μSR

The standard μSR experiment described in section 2.3 probes the local internal field of the sample given by $\mathbf{B}_{\rm int}(\mathbf{r}, t)$. The result is a reduction of this four dimensional quantity into a one dimensional decay signal. There can therefore be considerable ambiguity in how to relate the results to properties of the local magnetic field in the sample. Additionally, in some cases, the muons cannot be considered a passive probe, resulting in a loss of full and reliable information [102, 143, 144]. The use of a separate "implanta-

tion sample", which is situated a known distance from the sample under investigation, was considered as one solution to these problems, as, when compared with conventional μSR, it enables a separation of near and far field components.

5.1.1 μSR experiments: passive and active

In a conventional experiment, once the muons have been produced and implanted into the sample under investigation and then the resultant positron has been emitted, there are essentially two ways in which to use the results to gain information about the sample:

(i) treat the muon as a passive probe that measures properties of the material with no perturbing effects.

(ii) treat the muon as an active probe in which its interactions with the material are a dominant feature.

Both cases are used extensively. One such example of using a muon as an active probe is to be found in conducting polymers [143]. There are also many examples in which the muon is used as an active probe as it diffuses around a sample [102, 144].

A problem arises when using a sample in which it is not possible to distinguish either case (i) or (ii) with significant confidence. This inspired the development and use of the novel technique described here.

Using an external sample to probe the bulk dipolar field distribution allows a measure of the magnetisation, similar to that obtained through susceptibility, but on the time-scale of muons, i.e. millisecond to nanosecond. In this way the same frequency response for muons can be utilized, without any need to include possible interactions with the sample. This was designed to act as an aid to the interpretation of standard μSR experiments, therefore enhancing the use and interpretation of μSR. This new method

would ideally be used alongside the traditional technique and will provide a crucial new handle on interpreting experimental results. The exterior implantation sample technique can also be used as a stand alone experiment in which bulk dynamics on the time scale of nanoseconds to microseconds can be sensitively measured.

One such area where this "far field" technique is immediately applicable is in the field of frustrated spin systems which have high ground state degeneracies that are sensitive to local perturbations. Long and short range order is of interest in these systems with slight perturbations potentially resulting in drastically different behaviour due to competing effects between spins. If there is damage to the structure by the implantation of muons then this could alter its overall behaviour, which would consequently be measured by the muon. After describing a calibration experiment in which this technique was verified as viable, a brief example of how this method has been applied to the study of the frustrated material $Tb_2Sn_2O_7$, with reference to work carried out by STB and SRG, will be discussed.

5.1.2 Using a separate "implantation" sample

A calibration experiment was carried out to test whether it was possible to modify a standard μSR experiment to incorporate a separate implantation sample in which the dipolar field from the sample can be accurately measured. A block of ferromagnetic nickel was chosen as the sample to be investigated, and a similarly sized block of silver used as the exterior "implantation" sample. The muon's relaxation is unperturbed by silver, meaning any response is from the sum of the applied field and the magnetized nickel sample's dipolar field. The distance between the two blocks was accurately controlled. Expressions for the dipolar field from a magnetised cuboid have been calculated by Engel-Herbert et al. [145]. These give the value of the dipolar field at any point $\mathbf{r}$

outside the magnetised volume, which in this case is the nickel block. This expression thus allows the distribution of the dipolar field $\mathbf{H}_{\rm ext}(\mathbf{r})$ to be calculated numerically throughout the volume of the silver implantation sample. The negligible demagnetization effects of silver mean the dipolar field in air and silver can be considered to be the same in the calculations.

5.1.3 Implantation sample experimental technique

The μSR experiment was carried out by STB and SRG on the MuSR spectrometer at the ISIS pulsed muon source situated in the Rutherford Appleton Laboratory. A schematic is shown in figure 5.1. The MuSR instrument in its standard configuration is described in Chapter 2. The only alteration in this case was placing the implantation sample in front of the sample under investigation.

Referring to figure 5.1, the muons were implanted into a silver block sufficiently thick to ensure that all muons would come to rest within it. The silver block was positioned a known distance from the polycrystalline nickel block of dimensions $40 \times 40 \times 0.5$ mm^3, that had previously been fully magnetised transverse to the direction of muon polarisation by the application and subsequent removal of a 50 mT magnetic field. This ensured the nickel was of single domain. Muons implanted into a silver sample have negligible relaxation so any observed relaxation is a direct consequence of the field arising from the nickel sample.

The muons implanted into the silver thus precessed in response to the field $\mathbf{H}_{\rm ext}(\mathbf{r})$ arising from the nickel and the mean magnetic field within the silver block was derived from the observed precession frequency. This Larmor precession is given by $\omega_\mu = \gamma_\mu B$ where γ_μ is the gyromagnetic ratio for the muon and $B = \mu_0 H$. Hence the field observed is H, the field perpendicular to the magnetisation of nickel (i.e. the field in the

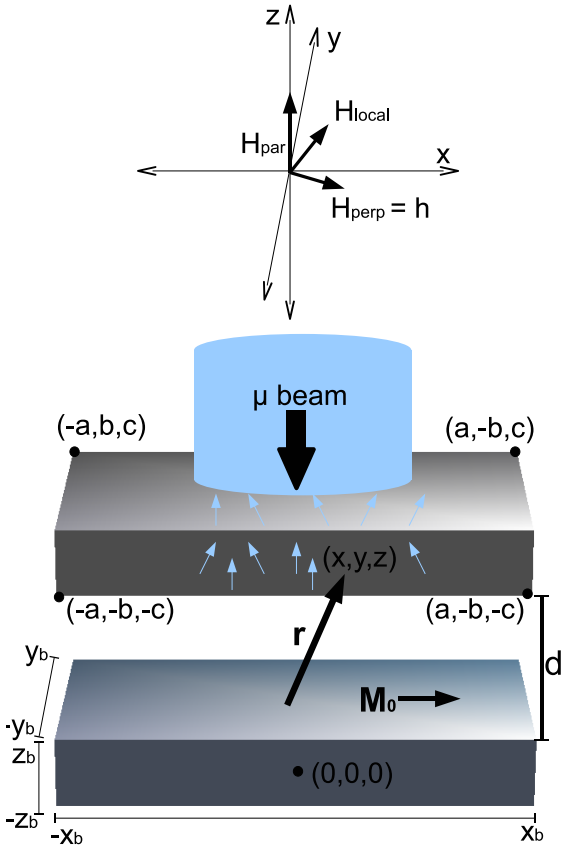

Figure 5.1: A schematic of the “far field” μSR experiment in which the muon beam is not implanted into the magnetic sample under investigation, instead a separate silver implantation sample is used which is a known distance from the magnetic sample under investigation.

xy plane in figure 5.1). The average response of the muons in the implantation sample thus gives the bulk magnetic properties of the sample under investigation.

5.1.4 Magnetic dipolar field equations

Starting from Maxwell’s equations, Engel-Herbert et al. [145] derived expressions for the vector field $\mathbf{H}_{\text{ext}}(\mathbf{r})$ arising from a uniformly magnetised bar magnet, assumed to be a parallelepiped with arbitrary dimensions and 90° angles. Equations 5.1, 5.2 and 5.3 represent their analytical solutions. Figure 5.1 defines the terms used in the following

equations:

$$H_x(x,y,z) = \frac{M_0}{4\pi}\sum_{k,l,m=1}^{2}(-1)^{k+l+m} \times \ln\left\{Z+\sqrt{X^2+Y^2+Z^2}\right\} \tag{5.1}$$

$$H_y(x,y,z) = \frac{M_0}{4\pi}\sum_{k,l,m=1}^{2}(-1)^{k+l+m}\frac{YX}{|Y||X|} \times \arctan\left\{\frac{|X|\cdot Z}{|Y|\cdot\sqrt{X^2+Y^2+Z^2}}\right\} \tag{5.2}$$

$$H_z(x,y,z) = \frac{M_0}{4\pi}\sum_{k,l,m=1}^{2}(-1)^{k+l+m} \times \ln\left\{X+\sqrt{X^2+Y^2+Z^2}\right\} \tag{5.3}$$

where,

$$\begin{aligned} X &= x+(-1)^k x_b \\ Y &= y+(-1)^l y_b \\ Z &= z+(-1)^m z_b \end{aligned}$$

5.1.5 μSR response

The muons used in the μSR technique relax in response to the magnetic field perpendicular to the direction of the applied muon polarization (which is parallel to the applied muon beam). In this geometry the muon beam is along the z direction. Hence the muon detects the magnetisation h in the xy direction given by:

$$h = \sqrt{H_x^2+H_y^2} \tag{5.4}$$

Equations 5.1, 5.2 and 5.3 were used to numerically evaluate the field distribution in the silver block. The simulation replicates the effect of the stray field from a magnetised

x	y	z	$B_x(mT)$	$B_y(mT)$	$B_z(mT)$	
$1.1x_b$	$1.1y_b$	$1.1z_b$	112.814	59.737	86.680	AS
			112.811	59.723	86.679	FEM
			112.814	59.737	86.680	IS
$2x_b$	$2y_b$	$2z_b$	7.268	8.330	3.892	AS
			7.268	8.330	3.892	FEM
			7.268	8.330	3.892	IS
$10x_b$	$10y_b$	$10z_b$	0.039413	0.058473	0.019740	AS
			0.039413	0.058473	0.019734	FEM
			0.039413	0.058473	0.019740	IS
$1.1x_b$	$1.1y_b$	0	180.916	114.796	0	AS
			180.916	114.765	0	FEM
			180.916	114.796	0	IS
$2x_b$	$2y_b$	0	8.400	9.935	0	AS
			8.400	9.935	0	FEM
			8.400	9.935	0	IS
$10x_b$	$10y_b$	0	0.042985	0.065197	0	AS
			0.042985	0.065197	0	FEM
			0.042985	0.065197	0	IS

Table 5.1: Comparison of results by Engel-Herbert in ref. [145] (AS and FEM) and the results obtained using the simulation produced here (IS) for the dipolar field at certain points given by (x, y, z). x_b, y_b and z_b are the dimensions of the sample under investigation defined in figure 5.1. Each seperate point is defined with respect to x_b, y_b and z_b. B_x (mT), B_y (mT) and B_z (mT) give the component of the dipolar field at the point (x, y, z).

volume, with dimensions $(2x_b, 2y_b, 2z_b)$, on another volume at a distance d away, with dimensions $(2a, 2b, 2c)$. The x and y dimensions were the same for both volumes, with the z dimension being retained as a variable. The exterior "implantation" (i.e. silver) volume was split up into a grid of 500,000 equal sized cubes. The perpendicular field h was found at the corners of each of these cubes. The cases for $x = \pm x_b$ and $y = \pm y_b$ are not defined by the analytical expressions and therefore had to be omitted. Using small enough grid spacings made this effect negligible. A circular beam cross section was used as the area in which muons would reside in the silver sample in the xy direction. Thus only the field within a cylindrical area inside the silver sample was considered, with the beam radius being extended from its approximate radius of 10 mm to 14 mm to account for beam drift and the fact that the muons would explore the silver sample whilst being implanted into the sample and diffusing to lose their energy.

The calculation also allowed the option of finding the field at a point a distance (x, y, z) from the centre of the magnetic sample i.e. from the origin. A selection of results are shown in table 5.1. These compare the calculation described here with the results printed in Engel-Herbert et al.'s paper [145]. The table shows the results for single points are correctly produced, giving confidence to the calculation of the field distribution produced here.

For each distance d of nickel to silver separation, the mean value of the magnetisation perpendicular to the beam direction was then evaluated, to be compared to the results of the μSR experiment, see Fig. 5.2.

The theoretical fit was obtained using a 53.5 mT saturation magnetised, which is within 10% of the expected saturation magnetisation of nickel [146], and a volume of $40 \times 40 \times 0.6$ mm^3. The beam radius of the muons in the calculation was 14 mm, expected to be a good approximation of the true beam radius within the silver sample.

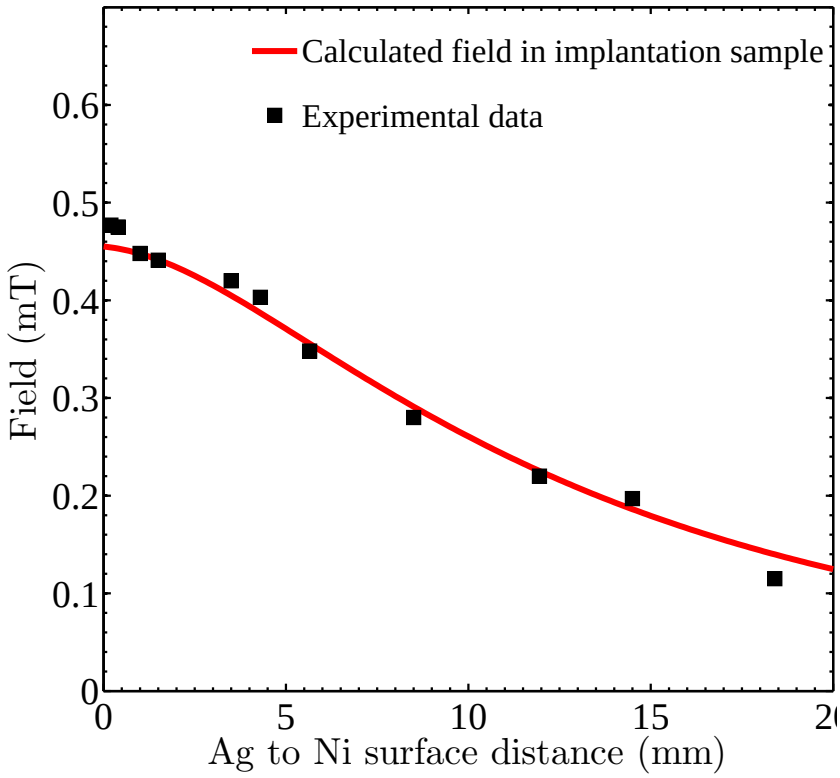

Figure 5.2: Experimental μSR and theoretical results obtained for the variation of the dipolar field felt by a silver volume when placed a known distance from a magnetised nickel volume. The parameters used for the calculation are a beam radius of 14 mm, saturation magnetisation of 53.5 mT in a $40 \times 40 \times 0.6$ mm magnetised sample.

(The MuSR information website lists the beam size at focus to be: Vertical: 8 mm fwhm, horizontal: adjustable, 7-15 mm fwhm [105]). The chosen parameters are believed to be well within reasonable experimental errors. For each distance, d, of the nickel to silver separation in the simulation the mean value of the magnetisation perpendicular to the beam direction was found. This represents what is measured in a μSR experiment. An excellent agreement is found between experiment and theory, which demonstrates that a small modification of the standard μSR technique may be used to derive an unbiased estimate of the sample magnetisation.

5.2 The study of $Tb_2Sn_2O_7$

As discussed in section 1.2.1 there has been much work on the pyrochlores, in particular the titanates and stannates. Only in the past couple of years, however, has $Tb_2Sn_2O_7$ received any significant attention [147–149]. Initial susceptibility measurements down to 1.8 K were reported [150]. The most in depth study before these three recent investigations was described in ref. [151] which investigated the magnetic properties of the rare earth pyrochlore stannates and included magnetic dc susceptibility measurements on $Tb_2Sn_2O_7$. The dc susceptibility measurements showed a divergence at 0.87 K which was attributed to ferromagnetic order. A recent review in ref. [12] on the frustrated rare earth titanate and stannate pyrochlores includes only one paragraph on $Tb_2Sn_2O_7$, pointing out that it has received scant attention and that much work is needed to prove the claim that it ferromagnetically orders at 0.87 K made previously in ref. [151]. Around the same time as the review in ref. [12], more detailed work on $Tb_2Sn_2O_7$ was reported [147]. $Tb_2Sn_2O_7$ was studied through neutron diffraction and specific heat measurements. It was reported that the antiferromagnetic liquid like behaviour changed to ferromagnetic behaviour in two magnetic steps. Firstly a smeared transition at 1.3 K, and then an abrupt transition at 0.87 K. The behaviour was explained as a new magnetic structure and given the name "ordered spin ice" due to its similarity to the spin ice behaviour found in related pyrochlores. This "ordered spin ice" was said to have both ferromagnetic and antiferromagnetic characteristics. Shortly after the findings of ref. [147] two further investigations of $Tb_2Sn_2O_7$, in an attempt to clarify the magnetic behaviour, were reported [148, 149]. Both involved μSR. The initial μSR experiment [148] found no signature of a static magnetically ordered state reported by ref. [147]. The neutron results did however agree with those previously carried out. The explanation arrived at

was that of a dynamical ground state in which the Tb^{3+} magnetic moment has a characteristic fluctuation time of $\simeq 10^{-10}$ s. This fluctuation time is much less than had been previously inferred, despite agreement on the neutron results. Further μSR results followed [149]. Results were obtained down to 35 mK and they showed that strong fluctuations persist down to well below 0.87 K where the ferromagnetic transition is said to occur. It was proposed that the dynamics observed in the μSR results were due to clusters of correlated spins with the ordered spin ice structure. Whole clusters of well ordered spins were proposed to fluctuate in between six degenerate configurations allowed in the "ordered spin ice" structure. These results would mean that $Tb_2Sn_2O_7$ would join $Gd_2Ti_2O_7$, $Gd_2Sn_2O_7$ and $Er_2Ti_2O_7$ in having simultaneously fluctuations and long ranged order [149].

5.2.1 The study of $Tb_2Sn_2O_7$ using "far field" μSR

The analysis of $Tb_2Sn_2O_7$ in the literature relied heavily on μSR and trying to fit the results with the observed neutron experiments. This has led to the consideration of what effect the implanted muons have on the local structure and what the muons are actually probing.

A "far field" μSR experiment using the method described in section 5.1.2 was carried out by STB and SRG. The results are reported in ref. [152].

Figure 5.3 is one result of the experiment (Fig. 4 in ref. [152]). The decay of muons implanted into the silver sample does not oscillate at 1.4 K (above the transition temperature) indicating that there is no static field in which the muons in the silver are precessing around. At 0.35 K (below the transition temperature) there are clear oscillations observed. This can be explained by the muons precessing around the static field produced in the $Tb_2Sn_2O_7$ supporting the static magnetisation hypothesis proposed as the

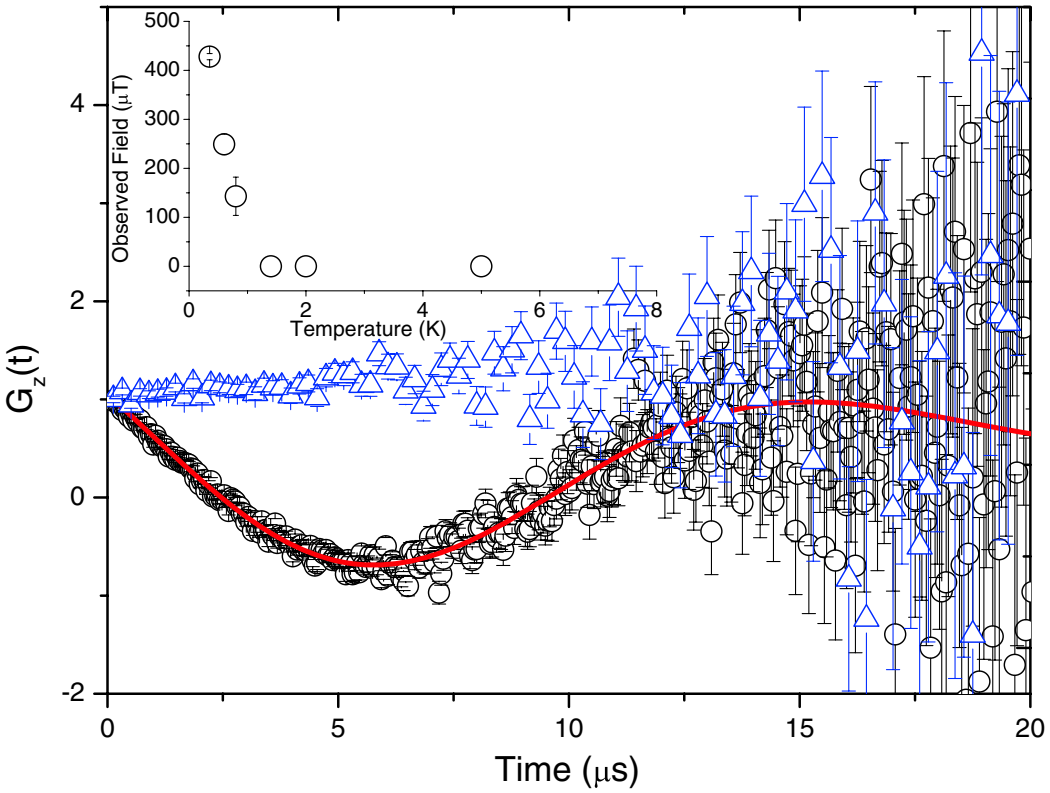

Figure 5.3: (Fig. 4 in ref. [152]): The muon signal of the observed field in the silver above (triangles) and below (circles) T_c in $Tb_2Sn_2O_7$. Oscillations are clearly observed below T_c. The red line is a fit to the relaxation. The inset shows the temperature dependence of the observed field.

ordering and ruling out dynamical correlations as proposed in refs. [148, 149]. The temperature dependence of the measured dipolar field correlates well with the expected ferromagnetic order parameter. This definitively rules out the "dynamical structure" hypothesis put forward in refs. [148, 149], and highlights the advantages of the use of a separate implantation sample.

5.3 Summary of "far field" μSR

In summary, the use of μSR as a magnetometer with complementary characteristics to the usual local probe experiment may be exploited in the study of magnetic samples using the "far field" technique outlined, thus allowing the extension from a purely local probe to both a local and bulk probe. The calibration experiment described here shows that it is possible to accurately measure the dipolar field from a sample in an exterior "implantation" sample. The experimental technique does not require any change in the standard μSR apparatus and, is easy to employ, and keeps the same time-scale and frequency response. In specific cases it may prove useful as a source of crucial experimental information that will facilitate the accurate interpretation of standard μSR results. An experimental investigation using this method with respect to the frustrated system $Tb_2Sn_2O_7$ has been shown to give a more complete and thorough understanding when compared to solely using muons as a local probe implanted in the sample.

The experimental work carried out by STB and SRG has been published [152] and the numerical work I carried out has been published in a separate article [153].

Chapter 6

Conclusions

This thesis has considered the magnetic properties of Ba_2HoSbO_6, Ba_2ErSbO_6 and $LuCuGaO_4$, motivated by their geometry which has been proposed to lead to frustrated behaviour. The main conclusions from the experimental investigations will now be considered and a strategy for future work outlined.

6.1 Conclusions for Ba_2HoSbO_6 and Ba_2ErSbO_6

Ba_2HoSbO_6 has been characterised in ref. [26] at room temperature as having the space group $Fm\overline{3}m$, with the rare earth ions on an fcc lattice of edge sharing tetrahedra: a geometry which can cause geometric frustration. Along with the lack of ordering in the susceptibility results reported down to 1.5 K, despite $\theta_W = -4.7(2)$, led to the conclusion that the rare earth double perovskites are an "excellent model system for the detailed study of geometric magnetic frustration" [26]. This thesis undertook the first detailed low temperature study of the rare earth double perovskites Ba_2HoSbO_6 and Ba_2ErSbO_6.

The neutron powder diffraction results in section 3.2 confirmed both compounds crystal structure to be unchanged down to 1.5 K, with no evidence of magnetic ordering or diffuse scattering. The magnetic component results from polarised neutron diffrac-

tion showed no change between 5 K and 0.06 K (figures 3.10 and 3.12). This was a surprising result. There was no evidence of magnetic correlations, diffuse scattering or liquid like behaviour associated with magnetic frustration. The only feature was a form factor dependence with scattering angle which matched the expected behaviour for each rare earth ion, indicating paramagnetic behaviour.

Inelastic neutron scattering was carried out on MARI at ISIS which solved the CEF level scheme for Ba_2HoSbO_6 and Ba_2ErSbO_6, the results are shown in figure 3.22.

The solved CEF level scheme for Ba_2ErSbO_6 was used to calculate susceptibility and compared to experimental susceptibility results, the close agreement is shown in figure 3.32. The lack of ordering, despite a magnetic CEF ground state, is predicted to be a consequence of the large nearest neighbour distance of $\sim$6 Å prohibiting exchange interactions and subsequent magnetic ordering.

For Ba_2HoSbO_6 results calculated using the CEF parameters matched closely to experimental results, see figures 3.30 and 3.31. The solved CEF level scheme has a non-magnetic doublet ground state for Ba_2HoSbO_6 and a closely spaced magnetic triplet first excited state, this explains all the experimental results. The susceptibility and magnetic results from polarised neutron analysis was consistent with Ba_2HoSbO_6 behaving as a paramagnet; a non-magnetic ground state does not preclude magnetic behaviour. No evidence for an induced moment or level crossing were found.

The results clearly refute the evidence in ref. [26] that the behaviour in the investigated rare earth double perovskites could be explained as highly frustrated. The experimental susceptibility and specific heat carried out by X. Ke shown in figures 3.30 and 3.31 were initially thought to represent conclusive proof of spin liquid behaviour due to frustration of the Ho^{3+} ions. Although no ordering in susceptibility at the Curie-Weiss temperature is a signature of frustration, and the lack of a Schottky anomaly in the

specific heat results match that hypothesis, the study carried out in this thesis explains those results quantitatively and importantly also explains the neutron experimental results. Bulk measurements and a high frustration f value are not sufficient to accurately characterise a material as frustrated. Instead a complete picture, built up from bulk measurements and a microscopic model, is necessary to understand the true magnetic behaviour. The results in this thesis therefore highlight the importance of a carefully and thorough study when investigating new magnetic materials and show the importance of the crystal electric field in rare earth magnetic studies.

6.1.1 Future work on Ba_2HoSbO_6 and Ba_2ErSbO_6

The investigation of Ba_2HoSbO_6 and Ba_2ErSbO_6 in this thesis has produced a model that explains their zero field behaviour down to 0.06 K. There are, however, still various avenues for future work.

- The close spacing of the non-magnetic GS and first excited magnetic state in Ba_2HoSbO_6 suggests interesting behaviour. Although it was predicted in this thesis that the application of a magnetic field would not lead to the crossing of levels and a magnetic ground state, it would be of interest to verify this experimentally.
- Results from an inelastic neutron scattering experiment in an applied magnetic field would give the CEF level scheme at certain applied fields.
- Applying pressure to a system can alter the CEF level scheme and this could be used to create a magnetic ground state. Being able to switch between a non-magnetic to magnetic GS at a temperature well below a transition temperature in a frustrated system would be a unique and interesting experimental exercise.
- Measurements on other members of the series could find further interesting results on the fcc lattice.
- A zero field magnetic phase transition could be found by decreasing the temperature of investigation.

- It would be of interest to have a single crystal of both Ba_2HoSbO_6 and Ba_2ErSbO_6. Fields applied along different axis have been calculated to cause differing responses within the system from the magnetic and specific heat CEF calculations that would of interest to study.

6.2 Conclusions for $LuCuGaO_4$

$LuCuGaO_4$ has equal numbers of magnetic Cu^{2+} and non-magnetic Ga^{3+} ions on triangular bilayers, resulting in frustration of both spin and charge. Ref. [72] reported $LuCuGaO_4$ to have $\theta_W \approx -69$ K, with increased correlations below 50 K, but no ordering down to 1.5 K, suggesting it to be highly frustrated. From ac-susceptibility and specific heat results $LuCuGaO_4$ was classified as having a spin glass transition at $\sim$0.4 K, a conclusion refuted in this thesis. The work carried out in this thesis represents the first low temperature microscopic investigation of $LuCuGaO_4$, with the results showing $LuCuGaO_4$ to be a spin liquid at low temperature.

Neutron powder diffraction measurements agreed with reported structural results in ref. [72] in which the Lu ion sits at a shifted but well defined position above and below the Cu/Ga bilayers. The model was therefore extended down to 1.5 K. A model of randomly disordered Cu/Ga ions is sufficient to explain the diffraction data, but this thesis concludes that this is a misleading consequence of the similar scattering lengths of copper and gallium. Instead what is proposed is a minimisation of near neighbour charges on the bilayers to minimise Coulombic interactions. This produces a cation topology of branched loops shown figure 4.11.

Polarised neutron analysis confirmed $LuCuGaO_4$ to be a paramagnet at 50 K. Results between 5 K and 0.08 K were identical, within experimental error, see figure 4.3, and showed a change from paramagnetic to antiferromagnetic near neighbour correla-

tions. Inelastic neutron scattering confirmed the same behaviour. μSR probed the local interactions from 50 K to below 0.4 K. The results were not compatible with a spin glass below 0.4 K. Instead they corresponded to spin liquid behaviour, see figure 4.10.

Combining all the experimental results leads to the conclusion that $LuCuGaO_4$ is in the paramagnetic regime above 50 K. Correlations between the spins slowly develop but the overall behaviour remains paramagnetic down to just above 5 K. At 5 K the Cu^{2+} spins become correlated at the nearest neighbour distance and this correlation increases until 0.4 K, at which point $LuCuGaO_4$ is well described as a spin liquid, despite the presence of cation disorder.

6.2.1 Future work on $LuCuGaO_4$

The result that $LuCuGaO_4$ behaves as a spin liquid at low temperature with the spin-$\frac{1}{2}$ Cu^{2+} as the magnetic ion makes this compound of great interest for future studies. These could take various forms:

- Further verifications of the spin liquid model would be advantageous, this would include carrying out dc-susceptibility below 0.4 K.
- Inelastic neutron scattering results between 5 and above 50 K would be able to follow the onset of correlations in energy and Q.
- From the inelastic neutron scattering there is no evidence of a "gap" in the energy for constant Q associated with dimers. The question of the singlet state and the resonating valence bond in spin-$\frac{1}{2}$ materials is of current interest. Investigating the scaling of $\chi(Q,T)$ in $LuCuGaO_4$ would be of interest, with the dilute nature of the Cu^{2+} cations allowing a contrast with undilute spin-$\frac{1}{2}$ systems.
- The inherent charge frustration and possible ordering of the triangular bilayers needs to be more carefully investigated. Unfortunately the scattering length of Cu and Ga are prohibitively close to distinguish their scattering using neutrons. As

such either Ga could be replaced or other dilute members of the series could be investigated.

- Similar behaviour has been reported for $LuFeMgO_4$, however no conclusions considering all the results have been obtained. A study in light of the results reported here would be advantages.

6.3 "Far field" μSR conclusions

The alternative technique of "far field" μSR implants muons outside of the sample under investigation. This allows a further handle on the experimental results which, when used alongside the standard technique, can provide important extra detail. It also removes any need to know where the muon is residing in the sample.

It is widely assumed that the muons cause no damage to the sample when implanted, despite the implantation process involving muons with energies of the order MeV. There does not, however, appear to be a thorough study in the literature supporting this claim. In geometric frustrated systems the interactions are often subtle and any changes, such as introducing defects caused by muon implantation, has the potential to alter the state of the system: defects allow the degeneracy of frustrated ground states to be broken.

The results from this thesis show that it is possible to successfully carry out a μSR experiment using a separate implantation sample to measure the "far field" of a magnetic sample. It is directly applicable to frustrated materials, demonstrated by the success of using the technique to measure the magnetic behaviour of $Tb_2Sn_2O_7$.

It would be of interest to carry out a study on the effect of muon implantation, particularly with respect to geometric frustrated materials. "Far field" μSR has many future uses and will positively add to the tools available to experimental investigations of materials, particularly frustrated magnetic oxides.

Bibliography

1. J. H. V. Vleck, *The Theory of Electric and Magnetic Susceptibilities*. Oxford University Press, 1932.
2. G. H. Wannier, *Phys. Rev.*, vol. 79, no. 2, pp. 357–364, 1950.
3. R. M. F. Houtappel, *Physica*, vol. 16, no. 5, pp. 425–455, 1950.
4. P. W. Anderson, *Phys. Rev.*, vol. 102, no. 4, pp. 1008–1013, 1956.
5. G. Toulouse, *Commun. Phys.*, vol. 2, no. 4, pp. 115–119, 1977.
6. J. Villain, *J. Phys. C: Solid State Phys.*, vol. 10, no. 10, pp. 1717–1734, 1977.
7. J. Villain, *Zeitschrift für Physik B*, vol. 33, pp. 31–42, 1979.
8. A. P. Ramirez, *Ann. Rev. Mat. Sci.*, vol. 24, no. 1, pp. 453–480, 1994.
9. R. Moessner, *Can. J. Phys.*, vol. 79, pp. 1283–1291, 2001.
10. R. Moessner and J. T. Chalker, *Phys. Rev. B*, vol. 58, no. 18, pp. 12 049–12 062, 1998.
11. J. E. Greedan, *J. Mater. Chem.*, vol. 11, pp. 37–53, 2001.
12. J. E. Greedan, *J. Alloys Compd.*, vol. 408, pp. 444–455, 2006.
13. A. Harrison, *J. Phys.: Cond. Matt.*, vol. 16, no. 11, pp. S553–S572, 2004.
14. C. Broholm, G. Aeppli, G. P. Espinosa, and A. S. Cooper, *Phys. Rev. Lett.*, vol. 65, no. 25, pp. 3173–3176, 1990.

15. A. S. Wills and A. Harrison, *J. Chem. Soc., Faraday Trans.*, vol. 92, pp. 2161–2166, 1996.

16. M. P. Shores, E. A. Nytko, B. M. Bartlett, and D. G. Nocera, *J. Am. Chem. Soc.*, vol. 127, pp. 13 462–13 463, 2005.

17. J. E. Greedan, J. N. Reimers, C. V. Stager, and S. L. Penny, *Phys. Rev. B*, vol. 43, no. 7, pp. 5682–5691, 1991.

18. J. N. Reimers, J. E. Greedan, R. K. Kremer, E. Gmelin, and M. A. Subramanian, *Phys. Rev. B*, vol. 43, no. 4, pp. 3387–3394, 1991.

19. B. D. Gaulin, J. N. Reimers, T. E. Mason, J. E. Greedan, and Z. Tun, *Phys. Rev. Lett.*, vol. 69, no. 22, pp. 3244–3247, 1992.

20. J. S. Gardner, S. R. Dunsiger, B. D. Gaulin, M. J. P. Gingras, J. E. Greedan, R. F. Kiefl, M. D. Lumsden, W. A. MacFarlane, N. P. Raju, J. E. Sonier, I. Swainson, and Z. Tun, *Phys. Rev. Lett.*, vol. 82, no. 5, pp. 1012–1015, 1999.

21. M. J. Harris, S. T. Bramwell, D. F. McMorrow, T. Zeiske, and K. W. Godfrey, *Phys. Rev. Lett.*, vol. 79, no. 13, pp. 2554–2557, 1997.

22. A. P. Ramirez, A. Hayashi, R. J. Cava, R. Siddharthan, and B. S. Shastry, *Nature*, vol. 399, pp. 333–335, 1999.

23. C. Castelnovo, R. Moessner, and S. L. Sondhi, *Nature*, vol. 451, pp. 42–45, 2008.

24. S. T. Bramwell, S. R. Giblin, S. Calder, R. Aldus, D. Prabhakaran, and T. Fennell, *Nature*, vol. 461, pp. 956–959, 2009.

25. S. Rosenkranz, A. P. Ramirez, A. Hayashi, R. J. Cava, R. Siddharthan, and B. S. Shastry, *J. Appl. Phys.*, vol. 87, no. 9, pp. 5914–5916, 2000.

26. H. Karunadasa, Q. Huang, B. G. Ueland, P. Schiffer, and R. J. Cava, *PNAS*, vol. 100, no. 14, pp. 8097–8102, 2003.

27. R. H. Mitchell, *Perovskites Modern and Ancient*. Almaz Press, 2002.

28. L. G. Tejuca and J. L. G. Fierro, Eds., *Properties and Applications of Perovskite-type Oxides*. Marcel Dekker Inc, New York, 1992.

29. Y. Doi, Y. Hinatsu, A. Nakamura, Y. Ishii, and Y. Morii, *J. Mater. Chem.*, vol. 13, no. 7, pp. 1758–1763, 2003.

30. Y. Izumiyama, Y. Doi, M. Wakeshima, Y. Hinatsu, Y. Shimojo, and Y. Morii, *J. Phys.: Cond. Matt.*, vol. 13, no. 6, pp. 1303–1313, 2001.

31. Y. Kanaiwa, M. Wakeshima, and Y. Hinatsu, *Mater. Res. Bull.*, vol. 37, no. 11, pp. 1825–1836, 2002.

32. B. D. Dunlap and G. K. Shenoy, *Phys. Rev. B*, vol. 12, no. 7, pp. 2716–2724, 1975.

33. W. R. Gemmill, M. D. Smith, and H. C. zur Loye, *J. Solid State Chem.*, vol. 177, no. 10, pp. 3560–3567, 2004.

34. D. Harada, M. Wakeshima, and Y. Hinatsu, *J. Solid State Chem.*, vol. 145, no. 1, pp. 356–360, 1999.

35. Y. Hinatsu and Y. Doi, *Bull. Chem. Soc. Jpn*, vol. 76, no. 6, pp. 1093–1113, 2003.

36. A. Danielian, *Phys. Rev. Lett.*, vol. 6, no. 12, pp. 670–671, 1961.

37. T. Oguchi, H. Nishimori, and Y. Taguchi, *J. Phys. Soc. Jpn.*, vol. 54, pp. 4494–4497, 1985.

38. H. T. Diep and H. Kawamura, *Phys. Rev. B*, vol. 40, no. 10, pp. 7019–7022, 1989.

39. J. L. Alonso, A. Tarancón, H. G. Ballesteros, L. A. Fernández, V. Martín-Mayor, and A. Muñoz Sudupe, *Phys. Rev. B*, vol. 53, no. 5, pp. 2537–2545, 1996.

40. C. L. Henley, *J. Appl. Phys.*, vol. 61, no. 8, pp. 3962–3964, 1987.

41. J. Villain, R. Bidaux, J.-P. Carton, and R. Conte, *J. Phys.*, vol. 41, no. 11, pp. 1263–1272, 1980.

42. J. D. M. Champion, M. J. Harris, P. C. W. Holdsworth, A. S. Wills, G. Balakrishnan, S. T. Bramwell, E. Čižmár, T. Fennell, J. S. Gardner, J. Lago, D. F. McMorrow, M. Orendáč, A. Orendáčová, D. M. Paul, R. I. Smith, M. T. F. Telling, and A. Wildes, *Phys. Rev. B*, vol. 68, no. 2, pp. 020 401–1 – 020 401–4, 2003.

43. P. G. Casado, A. Mendiola, and I. Rasines, *Zeitschrift Fur Anorganische Und Allgemeine Chemie*, vol. 510, no. 3, pp. 194–198, 1984.

44. P. J. Saines, B. J. Kennedy, and M. M. Elcombe, *J. Solid State Chem.*, vol. 180, no. 2, pp. 401–409, 2007.

45. J. A. Aguiar, C. C. D. Silva, Y. P. Yadava, D. A. L. Tellez, J. M. Ferreira, and E. Montarroyos, *J. Low Temp. Phys.*, vol. 117, no. 3/4, pp. 969–973, 1998.

46. J. A. Aguiar, C. C. D. Silva, Y. P. Yadava, D. A. L. Tellez, J. M. Ferreira, J. Guzman, and E. Chavira, *Physica C*, vol. 307, no. 3, pp. 189–196, 1998.

47. J. A. Alonso, C. Cascales, P. G. Casado, and I. Rasines, *J. Solid State Chem.*, vol. 128, no. 2, pp. 247–250, 1997.

48. G. Blasse, *J. Inorg. Nucl. Chem.*, vol. 27, no. 5, pp. 993–1003, 1965.

49. Y. Doi and Y. Hinatsu, *J. Phys.: Cond. Matt.*, vol. 13, pp. 14 191–4202, 2003.

50. B. J. Kennedy, P. J. Saines, Y. Kubota, C. Minakata, H. Hano, K. Kato, and M. Takata, *Mater. Res. Bull.*, vol. 42, no. 11, pp. 1875–1880, 2007.

51. E. J. Cussen, D. R. Lynham, and J. Rogers, *Chem. Mat*, vol. 18, no. 12, pp. 2855–2866, 2006.

52. M. Lufaso and P. Woodward, *Acta Cryst. B*, vol. 57, pp. 725–738, 2001.

53. A. Glazer, *Acta Cryst. B*, vol. 28, pp. 3384–3392, 2005.

54. W. T. Fu and D. J. W. Ijdo, *J. Solid State Chem.*, vol. 178, no. 7, pp. 2363–2367, 2005.

55. E. Bucher, H. J. Guggenheim, K. Andres, G. W. Hull, and A. S. Cooper, *Phys. Rev. B*, vol. 10, no. 7, pp. 2945–2951, 1974.

56. C. Cheng and P. Dorain, *J. Chem. Phys.*, vol. 65, no. 2, pp. 785–791, 1976.

57. G. E. Fish, M. H. North, and H. J. Stapleton, *J. Chem. Phys.*, vol. 73, no. 10, pp. 4807–4815, 1980.

58. J. P. Morley, T. R. Faulkner, F. S. Richardson, and R. W. Schwartz, *J. Chem. Phys.*, vol. 75, no. 2, pp. 539–560, 1981.

59. C. A. Morrison, R. P. Leavitt, and D. E. Wortman, *J. Chem. Phys.*, vol. 73, no. 6, pp. 2580–2598, 1980.

60. E. Veenendaal, H. Brom, and W. Huiskamp, *Physica B & C*, vol. 121, no. 1-2, pp. 1–29, 1983.

61. B. Bleaney, *Proc. R. Soc. Lond. A*, vol. 376, pp. 217–233, 1981.

62. R. Clad and J. M. Bouton, *J. Phys. F: Metal Phys.*, vol. 11, pp. 207–216, 1981.

63. R. Ballou, C. Lacroix, and M. D. Requerio, *Phys. Rev. Lett.*, vol. 66, pp. 1910–1913, 1991.

64. H. R. Molavian, M. J. P. Gingras, and B. Canals, *Phys. Rev. Lett.*, vol. 98, no. 15, pp. 157 204–1 – 157 204–4, 2007.

65. E. A. Goremychkin, R. Osborn, B. D. Rainford, R. T. Macaluso, D. T. Adroja, and M. Koza, *Nat. Phys.*, vol. 4, no. 10, pp. 766–770, 2008.

66. A. D. Christianson, J. M. Lawrence, J. L. Zarestky, H. S. Suzuki, J. D. Thompson, M. F. Hundley, J. L. Sarrao, C. H. Booth, D. Antonio, and A. L. Cornelius, *Phys. Rev. B*, vol. 72, pp. 024 402–1 – 024 402–6, 2005.

67. T. Kelley, W. Beyermann, R. Robinson, H. Nakotte, P. Canfield, and F. Trouw, *Physica B*, vol. 261, pp. 163–165, 1999.

68. D. E. MacLaughlin, R. H. Heffner, G. J. Nieuwenhuys, P. C. Canfield, A. Amato, C. Baines, A. Schenck, G. M. Luke, Y. Fudamoto, and Y. J. Uemura, *Phys. Rev. B*, vol. 61, no. 1, pp. 555–563, 2000.

69. Y. Yamada, K. Kitsuda, S. Nohdo, and N. Ikeda, *Phys. Rev. B*, vol. 62, no. 18, pp. 12 167–12 174, 2000.

70. T. E. Saunders and J. T. Chalker, *Phys. Rev. Lett.*, vol. 98, no. 15, p. 157201, Apr 2007.

71. L. Bellier-Castella, M. Gingras, P. Holdsworth, and R. Moessner, *Can. J. Phys.*, vol. 79, no. 11-12, pp. 1365–1371, 2001.

72. R. J. Cava, A. P. Ramirez, Q. Huang, and J. J. Krajewski, *J. Solid State Chem.*, vol. 140, no. 2, pp. 337–344, 1998.

73. N. Ikeda, H. Ohsumi, K. Ohwada, K. Ishii, T. Inami, K. Kakurai, Y. Murakami, K. Yoshii, S. Mori, Y. Horibe, and H. Kito, *Nature*, vol. 436, no. 7054, pp. 1136–1138, 2005.

74. J. Iida, M. Tanaka, Y. Nakagawa, S. Funahashi, N. Kimizuka, and S. Takehawa, *J. Phys. Soc. Jpn.*, vol. 62, no. 5, pp. 1723–1735, 1993.

75. K. Yoshii, N. Ikeda, Y. Matsuo, Y. Horibe, and S. Mori, *Phys. Rev. B*, vol. 76, no. 2, pp. 024 423–1 – 024 423–12, 2007.

76. K. Yoshii, N. Ikeda, Y. Okajima, Y. Yoneda, Y. Matsuo, Y. Horibe, and S. Mori, *Inorganic Chemistry*, vol. 47, no. 14, pp. 6493–6501, 2008.

77. A. Wiedenmann, W. Gunsser, J. Rossat-Mignod, and M. O. Evrard, *J. Magn. Magn. Mater.*, vol. 31, pp. 1442–1444, 1983.

78. N. Ikeda, K. Kohn, E. Himoto, and M. Tanaka, *J. Phys. Soc. Jpn.*, vol. 64, no. 11, pp. 4371–4377, 1995.

79. M. Tanaka, E. Himoto, and Y. Todate, *J. Phys. Soc. Jpn.*, vol. 64, pp. 2621–2627, 1995.

80. Y. Todate, N. Ohnishi, M. Tanaka, K. Nishiyama, and K. Nagamine, *Hyperfine Interact.*, vol. 104, no. 1–4, pp. 375–380, 1997.

81. Y. Todate, E. Himoto, C. Kikuta, M. Tanaka, and J. Suzuki, *Phys. Rev. B*, vol. 57, no. 1, pp. 485–491, 1998.

82. T. Sunaga, M. Tanaka, N. Sakai, and Y. Tsunoda, *J. Phys. Soc. Jpn.*, vol. 70, no. 12, pp. 3713–3718, 2001.

83. H. Dabkowska, A. Dabkowski, G. Luke, and B. Gaulin, *J. Phys. Soc. Jpn.*, vol. 234, pp. 411–414, 2002.

84. T. Matsumoto, N. Mri, J. Iida, M. Tanaka, K. Siratori, F. Izumi, and H. Asano, *Physica B*, vol. 180-181, no. Part 2, pp. 603 – 605, 1992.

85. Y. Todate, C. Kikuta, E. Himoto, M. Tanaka, and J. Suzuki, *J. Phys.: Cond. Matt.*, vol. 10, no. 18, pp. 4057–4070, 1998.

86. S. Katano, T. Matsumoto, S. Funahashi, J. Iida, M. Tanaka, and J. W. Cable, *Physica B*, vol. 213, pp. 218–220, 1995.

87. J. Iida, Y. Nakagawa, S. Funahashi, S. Takekawa, and N. Kimizuka, *J. Phys.*, vol. 49, no. C–8, pp. 1497–1498, 1988.

88. J. Chadwick, *Proc. R. Soc. Lond. A*, vol. A136, pp. 692–708, 1932.

89. G. L. Squires, *Introduction to the Theory of Thermal Neutron Scattering*. Dover Publications, Inc., 1996.

90. G. E. Bacon, *Neutron Diffraction, 3rd Edition*. Oxford: Clarendon Press, 1975.

91. J. Rossat-Mignod, *Methods in Experimental Physics*, K. Scold and D. Price, Eds. Academic Press, 1987.

92. G. T. Trammell, *Phys. Rev.*, vol. 92, no. 6, pp. 1387–1393, 1953.

93. www.isis.rl.ac.uk/excitations/mari.

94. www.isis.rl.ac.uk/disordered/GEM.

95. A. C. Hannon, *Nucl. Instrum. Methods Phys. Res., Sect. A*, vol. 551, no. 1, pp. 88–107, 2005.

96. www.ill.eu/IN4.

97. www.ill.eu/D1a.

98. www.ill.eu/D7.

99. J. R. Stewart, P. P. Deen, K. H. Andersen, H. Schober, J.-F. Barthélémy, J. M. Hillier, A. P. Murani, T. Hayes, and B. Lindenau, *J. Appl. Cryst.*, vol. 42, pp. 69–84, 2009.

100. S. L. Lee, S. H. Kilcoyne, and R. Cywinski, Eds., *Muon Science*. Institute of Physics, 1999.

101. K. Nagamine, *Introductory Muon Science*. Cambridge University Press, 2003.

102. S. J. Blundell, *Contemp. Phys*, vol. 40, pp. 175–192, 1999.

103. P. D. de Réotier and A. Yaouanc, *J. Phys.: Cond. Matt.*, vol. 9, no. 43, pp. 9113–9166, 1997.

104. S. F. J. Cox, *J. Phys. C: Solid State*, vol. 20, no. 22, pp. 3187–3319, 1987.

105. www.isis.rl.ac.uk/muons/musr.

106. A. Larson and R. V. Dreele, "General structure analysis system (GSAS)," *Los Alamos National Laboratory Report LAUR*, pp. 86–748, 2000.

107. B. H. Toby, *J. Appl. Cryst.*, vol. 34, no. 2, pp. 210–213, 2001.

108. A. Wills, *Physica B*, vol. 276, no. 2, pp. 680–681, 2000.

109. R. M. Moon, W. C. Koehler, H. R. Child, and L. J. Raubenheimer, *Phys. Rev.*, vol. 176, no. 2, pp. 722–731, 1968.

110. Y. J. Tang, X. W. Cao, J. C. Ho, and H. C. Ku, *Phys. Rev. B*, vol. 46, no. 2, pp. 1213–1215, 1992.

111. P. J. Brown, *Magnetic form factors*. International tables for crystallography, vol. C, ch. 4.4.5, International tables for crystallography vol. C (A. J. C. Wilson, ed.), pp. 391–399.

112. H. A. Bethe, *Splitting of terms in crystals*. Consultants Bureau, New York, Complete English translation from: *Annalen der Physik*, vol. 3, pp. 133-206, 1929.

113. M. T. Hutchings, *Solid State Phys.*, vol. 16, pp. 227–273, 1964.

114. K. W. H. Stevens, *Proc. Phys. Soc. London, Sect. A*, vol. 65, no. 3, pp. 209–215, 1952.

115. K. R. Lea, M. J. M. Leask, and W. P. Wolf, *J. Phys. Chem. Solids*, vol. 23, pp. 1381–1405, 1962.

116. D. Schmitt, P. Morin, and J. Pierre, *Phys. Rev. B*, vol. 15, no. 4, pp. 1698–1705, 1977.

117. W.-H. Li, J. W. Lynn, H. B. Stanley, T. J. Udovic, R. N. Shelton, and P. Klavins, *Phys. Rev. B*, vol. 39, no. 7, pp. 4119–4126, 1989.

118. A. Podlesnyak, A. Mirmelstein, N. Golosova, E. Mitberg, I. Leonidov, V. Kozhevnikov, I. Sashin, F. Altorfer, and A. Furrer, *Appl. Phys.*, vol. 74, pp. 1746–1748, 2002.

119. P. Fulde and M. Loewenhaupt, *Adv. Phys.*, vol. 34, no. 5, pp. 589–661, 1985.

120. U. Walter, *J. Phys. Chem. Solids*, vol. 45, no. 4, pp. 401–408, 1984.

121. R. J. Birgenea, *J. Phys. Chem. Solids*, vol. 33, no. 1, pp. 59–68, 1972.

122. J. R. Dean and D. Bloor, *J. Phys. C: Solid State*, vol. 5, no. 20, pp. 2921–2940, 1972.

123. J. B. Gruber, J. R. Henderson, M. Muramoto, K. Rajnak, and J. G. Conway, *J. Chem. Phys.*, vol. 45, no. 2, pp. 477–482, 1966.

124. N. Magnani, A. Baraldi, E. Buffagni, R. Capelletti, M. Mazzera, S. Brovelli, and A. Lauria, *Phys. Stat. Sol.*, vol. 4, pp. 1209–1212, 2007.

125. P. Fabi, "Focus manual," *ISIS Science Division, Rutherford Appleton Laboratory, ISSN 1358-6254*, 1995.

126. P. Morin, J. Rouchy, and Z. Kazei, *Phys. Rev. B*, vol. 51, no. 21, pp. 15 103–15 112, 1995.

127. J. T. Smit, H. J. Van Wijk, L. J. De Jongh, and R. L. Carlin, *Chem. Phys. Lett.*, vol. 62, no. 1, pp. 158 – 160, 1979.

128. J.-M. Broto, H. Rakoto, and Z. A. Kazei, *J. Phys.: Cond. Matt.*, vol. 15, no. 50, pp. 8767–8779, 2003.

129. Z. Kazei, V. Snegirev, A. Andreenko, and O. Kondratiev, *J. Magn. Magn. Mater.*, vol. 300, no. 1, pp. 430–432, 2006.

130. J. Jensen and A. R. Mackintosh, *Rare Earth Magnetism*. Clarendon Press, 1991.

131. Y. Tanaka, H. Tanaka, T. Ono, A. Osawa, K. Morishita, K. Iio, T. Kato, H. A. Katori, M. I. Bartashevich, and T. Goto, *J. Phys. Soc. Jpn.*, vol. 76, no. 10, pp. 3068–3075, 2001.

132. O. V. Lounasmaa, *Phys. Rev.*, vol. 128, no. 3, pp. 1136–1139, 1962.

133. A. J. Freeman and J. P. Desclaux, *J. Magn. Magn. Mater.*, vol. 12, pp. 11–21, 1979.

134. S. Calder, S. Giblin, D. R. Parker, P. P. Deen, C. Ritter, R. J. Stewart, and T. Fennel, *unpublished*, 2009.

135. S. Blundell, *Magnetism in Condensed Matter*. Oxford University Press, 2006.

136. M. A. de Vries, J. R. Stewart, P. P. Deen, J. O. Piatek, G. J. Nilsen, H. M. R. nnow, and A. Harrison, *Phys. Rev. Lett.*, vol. 103, no. 23, pp. 237 201–(1)–237 201–(4), 2009.

137. F. Pratt, *Physica B*, vol. 289-290, pp. 710–714, 2000.

138. A. Keren, P. Mendels, I. Campbell, and J. Lord, *Phys. Rev. Lett.*, vol. 77, pp. 1386 – 1389, 1996.

139. B. Fåk, F. C. Coomer, A. Harrison, D. Visser, , and M. E. Zhitomirsky, *EPL*, vol. 81, pp. 17 006–p1 – 17 006–p6, 1995.

140. P. Schiffer and I. Daruka, *Phys. Rev. B*, vol. 56, no. 21, pp. 13 712–13 715, 1997.

141. M. Isoda, *J. Phys.: Cond. Matt.*, vol. 20, no. 31, p. 315202 (8pp), 2008.

142. P. Mendels, F. Bert, M. A. de Vries, A. Olariu, A. Harrison, F. Duc, J. C. Trombe, J. S. Lord, A. Amato, and C. Baines, *Phys. Rev. Lett.*, vol. 98, pp. 077 204–1 – 077 204–4, 2007.

143. F. Pratt, I. Marshall, S. Blundell, A. Drew, S. Lee, F. Ogrin, N. Toyota, and I. Watanabe, *Physica B*, vol. 326, pp. 374–377, 2003.

144. S. F. J. Cox, *Solid State NMR*, vol. 11, pp. 103–121, 1998.

145. R. Engel-Herbert and T. Hesjedal, *J. Appl. Phys.*, vol. 97, no. 7, pp. 074 504–1 – 074 504–4, 2005.

146. C. Kittel, *Introduction to Solid State Physics (8th Edition)*. Wiley, 2005.

147. I. Mirebeau, A. Apetrei, J. Rodriguez-Carvajal, P. Bonville, A. Forget, D. Colson, V. Glazkov, J. P. Sanchez, O. Isnard, and E. Suard, *Phys. Rev. Lett.*, vol. 94, no. 24, pp. 246 402–1 – 246 402–4, 2005.

148. P. D. de Réotier, A. Yaouanc, L. Keller, A. Cervellino, B. Roessli, C. Baines, A. Forget, C. Vaju, P. C. M. Gubbens, A. Amato, and P. J. C. King, *Phys. Rev. Lett.*, vol. 96, no. 12, pp. 127 202–1 – 127 202–4, 2006.

149. F. Bert, P. Mendels, A. Olariu, N. Blanchard, G. Collin, A. Amato, C. Baines, and A. D. Hillier, *Phys. Rev. Lett.*, vol. 97, no. 11, pp. 117 203–1 –117 203–4, 2006.

150. V. Bondah-Jagalu and S. T. Bramwell, *Can. J. Phys.*, vol. 79, no. 11, pp. 1381–1385, 2001.

151. K. Matsuhira, Y. Hinatsu, K. Tenya, H. Amitsuka, and T. Sakakibara, *J. Phys. Soc. Jpn.*, vol. 71, no. 6, pp. 1576–1582, 2002.

152. S. R. Giblin, J. D. M. Champion, H. D. Zhou, C. R. Wiebe, J. S. Gardner, I. Terry, S. Calder, T. Fennell, and S. T. Bramwell, *Phys. Rev. Lett.*, vol. 101, no. 23, pp. 237 201–1 – 237 201–4, 2008.

153. S. Calder, S. R. Giblin, and S. T. Bramwell, *Physica B*, vol. 404, pp. 1017–1019, 2009.